

Spontaneous pattern formation as a route to droplet motion

Kevin Robert Langley, MSci

Thesis submitted to The University of Nottingham
for the degree of Doctor of Philosophy

June 2011

Abstract

Two important areas of physics are spontaneous pattern formation and droplet motion on surfaces. These two areas can be brought together since the texture of a surface can influence its wetting properties. Therefore by controlling the factors that determine the length scales of the patterns during spontaneous pattern formation, it is possible to design surfaces with very specific wetting properties. This was used to create surfaces that could direct the motion of sessile water droplets.

Patterned surfaces with micro-wrinkled surface structures were prepared by thermally evaporating thin Aluminium ($50 - 500nm$ thick) (Al) layers on to thick pre-strained layers of a silicone elastomer and subsequently releasing the strain. This resulted in the formation of sinusoidal periodic surface wrinkles with characteristic wavelengths in the $3 - 45\mu m$ range and amplitudes as large as $3.6\mu m$. The Al thickness dependence of the wrinkle wavelengths and amplitudes were determined for different values of the applied pre-strain and compared to a selection of wrinkle formation theories.

Samples with spatial gradients in wrinkle wavelength were also produced by applying mechanical strain gradients to the silicone elastomer layers prior to deposition of the Al capping layers. Sessile water droplets that were placed on these surfaces were found to have contact angles that were dependent upon their position. When vibrated close to their resonant frequency, these water droplets were observed to move from regions of short wrinkle wavelength to regions of large wrin-

kle wavelength. These samples are therefore viable candidates for the production of low cost gradient energy surfaces.

Acknowledgements

Now that my thesis is complete, I finally feel that I can now relax without the guilt that I could be 'writing another chapter'. And although I am relieved that it is finally over, I cannot take full responsibility for getting to this point. Firstly I would like to thank my supervisor, James Sharp, without whose guidance this thesis would not have been up to scratch. Also It must be said that without his continuous advice throughout my Ph.D. many of my experiments would not have worked.

The second person I feel I must thank for help with my thesis is Julian, he has suffered many questions on how to get L^AT_EX to do the things I wanted. I am sure he must now regret having let me know he was something of an expert with L^AT_EX. Next I would like to thank the people I have worked with in the labs, Magdalena, Zoe, James and Mike. In particular I would also like to thank Mike for allowing the use of his contact angle measurement software, without which I feel I would have spent many hours bashing my head against my keyboard trying to write something similar.

I also could not have finished this without the support of all the friends I have made in the Nanoscience group at Nottingham, it is that friendship that I am sure keeps all Ph.D. students sane. Last, but by no means least, I would like to thank my wife Laura, for her continuing support throughout and for proofreading much of my work despite finding it immensely uninteresting.

Publication List

K. R. Langley, and J. S. Sharp, “Microtextured Surfaces with Gradient Wetting Properties,” *Langmuir*, vol. 26, pp. 18349-18356

Contents

Abstract	i
Acknowledgments	iii
Publication List	iv
1 Motivation	1
References	4
2 Introduction	7
2.1 Spontaneous pattern formation	7
2.2 Gradient wetting properties	11
2.3 Theoretical model	14
2.3.1 Small deflection model	15
2.3.2 Large deflection model	20
2.4 Controlling the wetting properties	21
References	26
3 Experimental Techniques	31
3.1 Sample preparation	31

3.1.1	Elastomer curing	32
3.1.2	Evaporation	37
3.2	Optical microscopy and image analysis	39
3.2.1	Optical Microscope	39
3.2.2	Optical Microscopy	41
3.2.3	Image Analysis	43
3.2.4	Selection of a method to make gradient samples	46
3.3	Scanning force microscopy	47
3.3.1	Scanning force microscope	47
3.3.2	Scanning force microscopy	49
3.4	Measuring the wetting properties	50
3.5	Droplet motion	53
3.6	Measuring the amplitude of the speaker	55
3.7	JKR measurements	61
	References	64
4	Wrinkle Formation in Aluminium-Elastomer Bilayers	65
4.1	Thermally induced wrinkles	67
4.2	Dependence on the thickness of the aluminium capping layer	70
4.3	Dependence on the applied pre-strain	75
	References	79
5	Gradient Wrinkled Surfaces	80
5.1	Measuring the Gradient in Wavelength	81
5.2	Measuring the Amplitude of Wrinkles on the Gradient Samples	88

5.3 Area of the Wrinkled Structure	90
References	94
6 Wetting Properties of Wrinkled Surfaces	95
References	104
7 Droplet Motion	105
7.1 Moving a Droplet with White Noise	108
7.2 Driving the Motion with a Sinusoidal Signal	113
References	120
8 Conclusions	121
References	124
9 Future Work	125
References	127
List of Figures	128

CHAPTER 1

Motivation

The two interesting areas that are covered within this thesis are the physics of spontaneous pattern formation and the physics of driven/spontaneous droplet motion. Spontaneous pattern formation occurs when an external stimulus is applied to a multi-layer system, provided that the layers exhibit a different response to the stimulus. This process creates textured surfaces with very well defined length-scales. These surfaces have already found a range of uses. Examples of this include, stretchable electronics [1–3], micro-fluidic devices [4, 5], substrates for cell adhesion [6], surfaces for the separation of particles with different sizes [7] and to manufacture optical components such as diffraction gratings and optical diffusers [8, 9].

An interesting property of these surfaces that was shown by Chung *et al.* [5] is that sessile water droplets on these surfaces exhibit anisotropic wetting with contact angles that are dependent upon the length-scale of the surface texture (Shown in Figure 1.1). This indicated that it may be possible to create a textured sample on which a sessile water droplet will experience an energy gradient and consequently a force causing it to move on the surface. Depending on the strength of this force, the motion could either be spontaneous or the force could direct the motion once a stimulus is applied that causes the droplet to move.

This leads into the second area of physics covered in this thesis, droplet motion.

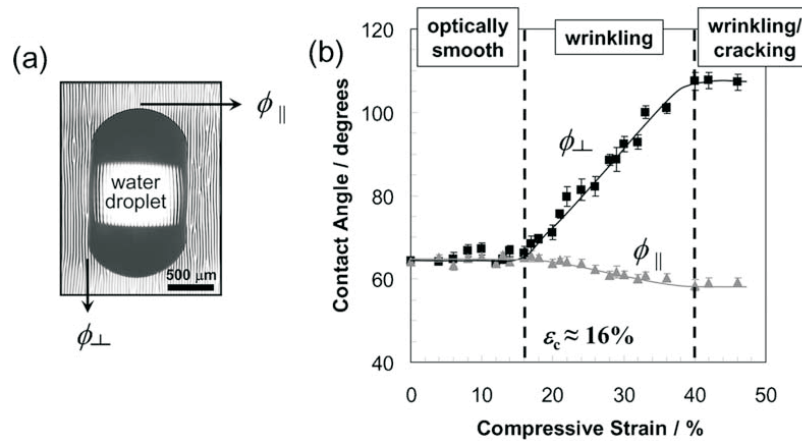


Figure 1.1: Figure from Chung *et al.* [5] (a) Optical micrograph of a $\approx 2\mu\text{l}$ water droplet on a patterned surface, revealing an elongated, parallel-sided shape; (b) Dependence of the water contact angles in two directions (ϕ_{\perp} and ϕ_{\parallel}) on sinusoidally patterned surfaces as a function of degree of compression. The lines are meant to guide the eye and the error bars represent one standard deviation of the data, which is taken as the experimental uncertainty of the measurement.

Surfaces with gradient wetting properties have received a great deal of recent attention because of their ability to direct the motion of small droplets. The control of the wetting properties on these surfaces is often achieved using gradients in chemical properties [10–14]. These chemically patterned gradient surfaces have been shown to exhibit both spontaneous droplet motion [10] and driven droplet motion [11–14]. Another approach that has been used to cause spontaneous droplet motion is the application of a temperature gradient [15, 16].

One additional method of controlling wetting properties is using a textured surface. The wetting properties are sensitive to the local topography, and this has led researchers to develop lithographically patterned surfaces with controlled wetting properties. Some studies have shown that is possible to get contact angles as large as 180° and produce superhydrophobic or “self-cleaning” surfaces [17].

Following on from this researchers have produced surfaces where the length-

scale of the surface structure varies with position. This was shown to result in gradients in the wetting properties of the substrates that assist in driving the motion of small droplets across the patterned surfaces [18–20].

The motivation behind this work was to determine whether these two areas could be brought together. The questions that this thesis will attempt to answer are:

1. Can spontaneous pattern formation be used to create highly ordered patterns with dimensions that can be accurately controlled by varying one or more of the parameters used during the manufacture of bilayers?
2. Do sessile water droplets on these samples exhibit contact angles that are dependent upon the amplitude and wavelength of the patterned surface?
3. Can samples be made that have a gradient in the amplitude and wavelength of the patterned surface, and does this lead to a gradient in the wettability of the surface?
4. Finally, do these gradient surfaces drive, or at least direct, the motion of sessile water droplets?

References

- [1] Y. Sun, V. Kumar, I. Adesida, and J. A. Rogers, “Buckled and wavy ribbons of GaAs for high-performance electronics on elastomeric substrate.,” *Advanced Materials*, vol. 18, pp. 2857–2862, 2006.
- [2] Y. Sun, W. M. Choi, H. Jiang, Y. Y. Huang, and J. A. Rogers, “Controlled buckling of semiconductor nanoribbons for stretchable electronics,” *Nat. Nanotechnol.*, vol. 1, pp. 201–207, 2006.
- [3] D. Y. Khang, H. Q. Jiang, Y. Huang, and J. A. Rogers, “A stretchable form of single-crystal silicon for high-performance electronics on rubber substrate.,” *Science*, vol. 311, pp. 208–212, 2006.
- [4] A. D. Stroock and G. M. Whitesides, “Controlling flows in microchannels with patterned surface charge and topography,” *Acc. Chem. Res.*, vol. 36, pp. 597–604, 2003.
- [5] J. Y. Chung, J. P. Youngblood, and C. M. Stafford, “Anisotropic wetting on tunable micro-wrinkled surfaces,” *Soft Matter*, vol. 3, pp. 1163–1169, 2007.
- [6] M. T. Lam, W. C. Clem, and S. Takayama, “Reversible on-demand cell alignment using reconfigurable microtopography,” *Biomaterials*, vol. 29, pp. 1705–1712, 2008.
- [7] K. Effimenko, M. Rackaitis, E. Manias, A. Vaziri, L. Mahadevan, and J. Genzer, “Nested self-similar wrinkling patterns in skins,” *Nat. Mater.*, vol. 4, pp. 293–297, 2005.
- [8] N. Bowden, W. T. S. Huck, K. E. Paul, and G. M. Whitesides, “The controlled formation of ordered, sinusoidal structures by plasma oxidation of an elastomeric polymer,” *Appl. Phys. Lett.*, vol. 75, pp. 2557–2559, 1999.

- [9] J.-H. Wang, C.-F. Chen, J.-R. Ho, T.-K. Shih, C.-C. Chen, W.-T. Whang, and J.-Y. Yang, “One-step fabrication of surface-relief diffusers by stress-induced undulations on elastomer,” *Opt. Laser Technol.*, vol. 41, pp. 804–808, 2009.
- [10] M. K. Chaudhury and G. M. Whitesides, “How to make water run uphill,” *Science*, vol. 256, pp. 1539–1541, 1992.
- [11] S. Daniel, S. Sircar, J. Gliem, and M. K. Chaudhury, “Ratcheting motion of liquid drops on gradient surfaces,” *Langmuir*, vol. 20, pp. 4085–4092, 2004.
- [12] S. Daniel, M. K. Chaudhury, and J. C. Chen, “Fast drop movements resulting from the phase change on a gradient surface,” *Science*, vol. 291, p. 633, 2001.
- [13] Y. Ito, M. Heydari, A. Hashimoto, T. Konno, A. Hirasawa, S. Hori, K. Kurita, and A. Nakajima, “The movement of a water droplet on a gradient surface prepared by photodegradation,” *Langmuir*, vol. 23, pp. 1845–1850, 2007.
- [14] L. Qiang, W. Hong, Z. Xun, and L. Mingwei, “Liquid droplet movement on horizontal surface with gradient surface energy,” *Science in China Series E: Technological Sciences*, vol. 49, pp. 733–741, 2006.
- [15] M. L. Ford and A. Nadim, “Thermocapillary migration of an attached drop on a solid surface,” *Phys. Fluids*, vol. 6, p. 3183, 1994.
- [16] Z. Jiao, X. Huang, N.-T. Nguyen, and P. Abrall, “Thermocapillary actuation of droplet in a planar microchannel,” *Microfluids and Nanofluids*, vol. 5, pp. 205–214, 2008.
- [17] Y. T. Cheng, D. E. Rodak, C. A. Wong, and C. A. Hayden, “Effects of micro- and nano-structures on the self-cleaning behaviour of lotus leaves,” *Nanotechnology*, vol. 17, pp. 1359–1362, 2006.
- [18] A. Shastry, M. J. Case, and K. F. Böhringer, “Directing droplets using microstructured surfaces,” *Langmuir*, vol. 22, pp. 6161–6167, 2006.

- [19] G. McHale, N. J. Shirtcliffe, S. Aqil, C. C. Perry, and M. I. Newton, “Topography driven spreading,” *Phys. Rev. Lett.*, vol. 93, no. 3, pp. 6102–6105, 2004.
- [20] J. Zhang and Y. Han, “A topography/chemical composition gradient polystyrene surface: Toward the investigation of the relationship between surface wettability and surface structure and chemical composition,” *Langmuir*, vol. 24, pp. 796–801, 2008.

Introduction

2.1 Spontaneous pattern formation

Spontaneous pattern formation processes in thin films provide a valuable method for the production of surfaces with well defined spatial variations in topography. The processes that underlie the formation of these spectacular patterns are usually governed by an underlying physical instability whose evolution results in the selection of a characteristic wrinkling length scale. This length scale is often determined as the result of a compromise between two or more competing physical processes that favour structure formation on different length scales. In each case the details of the pattern formation process vary, but the results are often very similar in terms of the morphology of the surface structures that are produced and the length scales that are associated with the characteristic wavelengths and amplitudes of the structures that form. The lateral sizes/wavelengths of the structures that form are typically in the sub micron to hundreds of microns range and the amplitudes vary from a few nanometres up to a few microns.

The production of structured surfaces with features on these technologically relevant length scales has resulted in them finding several applications:

- the manufacture of stretchable electronics [1–4]

- micro-fluidic devices [5, 6]
- substrates for cell adhesion [7]
- surfaces for the separation of particles with different sizes [8]
- measuring the mechanical properties of thin films of material [9]
- manufacture of optical components such as diffraction gratings and optical diffusers [10, 11]

Khang *et al.* [3] have demonstrated that it is possible to create circuits on these patterned surfaces using traditional materials such as silicon. However due to the wrinkled nature of the silicon within these structures, the ordinarily inflexible silicon can be bent and stretched to a much higher degree than is possible with conventional circuitry.

Stroock and Whitesides [5] have shown that for topographically patterned surfaces consisting of a series of grooves can be used as a series of channels through which fluids can be directed and used for applications such as the mixing of two micro-fluidic flows. Lam *et al.* [7] discussed how these wrinkled surfaces can be used as a reversible means to align cells on a surface. They showed that it is possible to align, unalign, and realign C2C12 myogenic cell line cells on these surfaces without inhibiting cell differentiation. This allows the study of cells that are not easily studied using traditional in vitro culture substrates.

Effimenko *et al.* [8] have shown that these surfaces can be used to separate particles of different sizes by allowing a fluid containing a mixture of the particles to flow over the wrinkles. Particles of different sizes then settle at different locations on the wrinkles.

Stafford *et al.* [9] have demonstrated that spontaneous pattern formation can be used to measure the elastic modulus of one of the two layers, provided the other is known. In particular this allows accurate measurements of the elastic modulus

of thin films of material by measuring the size of the wrinkles created. These measurements are needed as the properties of thin films can vary considerably from the bulk properties of the same materials, however traditional methods to acquire these properties would not easily be adapted to such thin films. This is done by measuring the wavelength and amplitudes of the patterns that form and relating these measurements to the mechanical properties of the two materials.

Wang *et al.* [11] have shown that silicon–elastomer bilayer systems can be used to create optical diffusers, and that by varying the parameters used in the manufacture of the samples, a range of optical patterns can be observed following illumination by a laser beam, due to the diffraction pattern resulting from the reflection of the laser light on the wrinkled surface.

Pattern formation processes that involve the bending of a rigid capping layer have been a key area of research because of the availability of a wide range of techniques (such as thermal evaporation, sputtering and spin coating) that enable researchers to deposit ultrathin films of material of well defined thickness and uniformity on to solid substrates. In these pattern formation processes, the mismatch in physical properties between the capping layer and an underlying layer or substrate is used to create a differential response of the layers in response to an applied stimulus.

In many ways, the physics which underlies these processes is very similar to that which describes the operation of a simple bimetallic strip. However, the confinement of the capping layer and underlying layers by a substrate often prevents the samples from bending macroscopically and the samples try to relieve the stresses that are exerted on them (as a result of the differential response of the layers) by wrinkling with a characteristic wavelength that typically lies in the microns to hundreds of microns range. This length scale is often significantly shorter than the lateral dimensions of the samples and is determined by a subtle balance of the in-plane stresses that are generated when an external stimulus is applied

and the bending stresses that arise in the rigid capping layers when they deform.

The in-plane stresses that develop in the samples can be generated by applying changes in temperature to samples with layers that have different thermal expansion coefficients [12] in the same way the bi-metallic strip works. They can also be driven by a differential response of the layers to a swelling solvent, such as that seen by Sharp and Jones [13], where an aliphatic polyester film on a silicon substrate was swelled in water. The silicon substrate was unaffected by the water while the polyester layer swelled, forming a series of blisters on the samples. When left to dry, these blisters collapsed leaving behind a surface patterned with a series of small wells. Thirdly, they can be driven by an applied mechanical stress [8, 14–16]. Ohzono and Shimomura [14] have shown that by applying a lateral compression to a polydimethylsiloxane-platinum bilayer, it is possible to create highly ordered wrinkles thanks to the platinum layer buckling to release the stress caused by the compression.

Other studies have used changes in the roughness of an interface between two materials to drive the instabilities that result in the formation of periodic surface patterns [17–19]. A significant amount of experimental work has also been focussed on the formation of surface structures on silicone elastomers that are coated with a rigid capping layer. The capping layers are usually deposited using thermal evaporation techniques [8, 12, 14–16, 20, 21] or by chemical modification of the surface of the elastomer [10, 11, 22, 23] and the patterns are formed by changes in the temperature of the samples or by the application of mechanical stress. In this case when the rigid capping layer is compressed, it wrinkles in order to relieve some of the stress that has been applied.

Numerous attempts have been made to derive theories which explain and predict the length scales that are associated with spontaneous pattern formation processes. A number of theories have been developed to describe pattern formation in systems where the length scales are formed by a mismatch in thermal expan-

sion coefficients [12, 24, 25], applied mechanical strains [26], roughness induced instabilities [17, 18] and as a result of dispersion forces [27].

Bowden *et al.* [12] considered the effects of the heating during evaporation on the sizes of the wrinkles that were created. In particular they developed a theory of the size of highly ordered wrinkles that occur adjacent to steps in the elastomeric layer.

Sridhar, Srolovitz, and Suo [26] calculated the size of wrinkles that would be created when an elastic film is compressed and attached to a viscous substrate. They also calculated the growth time for the wrinkles.

Sharp, Thomas, and Weir [18] devised a theory of wrinkling that arises from the instabilities created by the changes in roughness of the interface between two polymer layers. This instability can be exploited for wrinkle formation by melting the bottom layer and allowing the the top layer to freely move.

However, many of these theories only consider small amplitude deflections at the surfaces of the samples. This can result in errors when these theories are applied to situations where the amplitude of surface deflections is comparable to (or larger than) the thickness of one or more of the layers in the system. This has prompted the development of a number of more detailed theories of thin film wrinkling such as those developed by Huang, Suo and coworkers [28–31] and Song *et al.* [32, 33]. These models are obtained through a perturbation method, and they account for the two layers having different initial states, for example, the elastomer layer is initially under strain while the capping layer is unstrained.

2.2 Gradient wetting properties

Surfaces with gradient wetting properties have received a great deal of recent attention because of their ability to direct the motion of small liquid droplets. The control of the wetting properties on these surfaces is often achieved using

gradients in chemical properties [34–38]. Since the contact energy between the water droplet and the surface is dependent upon the chemistry of the surface, the addition of molecules with a different affinity to water will cause a change in the wetting properties that is dependent on the grafting density of these molecules. If a gradient in the density of these molecules is present, then there will also be a gradient in the wetting properties of the surface. These chemically patterned gradient surfaces have been shown to exhibit both spontaneous droplet motion [34] and driven droplet motion [35–38].

Chaudhury and Whitesides [34] prepared a silicon surface by allowing the vapour of decyltrichlorosilane [$\text{Cl}_3\text{Si}(\text{CH}_2)_9\text{CH}_3$] (a hydrophobic molecule) to diffuse over a silicon wafer. This created a higher packing of the molecule at one end of the silicon wafer and consequently a gradient in the wettability of the surface. The forces created by this gradient were enough to cause the droplet to spontaneously travel uphill.

Another approach that has been used to cause spontaneous droplet motion is the application of a temperature gradient [39, 40]. Ford and Nadim [39] present a model that demonstrates that it should be possible to create a force on a sessile water droplet by applying a gradient in the temperature of the substrate. Jiao *et al.* [40] then went on to show how this can be used to controllably move a water droplet in 2 dimensions with the use of two pairs of heaters positioned on the sides of a square substrate that could be used to set up 2 dimensional temperature profiles within the substrate.

An alternative approach to the production of gradient surfaces is to use topographically patterned substrates. In these experiments, chemically uniform surfaces were patterned with periodic surface structures on different length scales. This was shown to change the contact angles formed by sessile water droplets that were placed on the surface of these samples [6]. This works by increasing the contact area between the water and the substrate. The droplet then changes shape

to minimise the total energy. This involves reducing the size of the solid–liquid contact area while increasing the liquid–air contact area until the minimum energy is reached. By creating surfaces with a gradient in the lengthscales of the surface patterns, the total energy of the droplet will vary with position and it would be energetically favourable for the droplet to move to areas of the surface that allow a lower energy conformation/shape.

Recent studies have shown that the contact angles that are formed by water droplets on surface patterned elastomers are influenced by the amplitudes and wavelengths of one dimensional surface grooves [6]. Changes in the contact angle as large as 35° were seen over a range of pre-strain values. Moreover, these studies revealed that the contact angles that are observed on these surfaces differ depending on whether the droplets are viewed parallel or perpendicular to the groove axes. These interesting wetting phenomena occur due to the changes in the balance of interfacial energies that are experienced by a sessile droplet. For example, a droplet on a topographically patterned surface experiences a much larger contact area than a droplet with the same basal radius would on a flat surface. This means that the energy associated with the contact region between the drop and the surface is larger than it would be on a corresponding flat surface. This increase in the liquid–substrate interfacial energy component is unfavourable and the droplet can often reduce its total interfacial–surface energy by increasing the area of the liquid–air interface and thus altering its shape [6]. This can have a profound effect on the three phase contact angle at the liquid–air–substrate interface. Under extreme circumstances this can result in contact angles as large as 180° and the production of superhydrophobic or “self-cleaning” surfaces [41]. These are surfaces that have contact angles close to 180° , and as such water droplets will bead up and roll off. Surfaces of this kind occur naturally on the leaves of lotus plants, and the beading of the droplets acts to gather dirt from the leaf which is then washed away as the droplet rolls off of the leaf. This has been studied by Cheng *et al.* [41].

The sensitivity of surface wetting properties to local topography has also led researchers to develop lithographically patterned surfaces that have topography gradients where the characteristic length scale associated with the surface structures varies with position on the sample. This was shown to result in gradients in the wetting properties of the substrates that assist in driving the motion of small droplets across the patterned surfaces [42–44].

The purpose of this study was to bring together these two areas, spontaneous pattern formation and gradient wetting properties, and to determine the possibility of surfaces with a gradient in wetting properties produced using spontaneous pattern formation as it is a facile and inexpensive method for production.

A model system was selected for this study that consisted of a thick silicone elastomer layer with a thin aluminium(Al) layer deposited by thermal evaporation. The external stimulus used to cause the spontaneous pattern formation was a pre-strain, applied to the elastomer layer prior to the deposition of the Al layer, that could be released to cause a compressive stress within the Al layer.

An initial study of the pattern formation processes was carried out to determine the range of feature sizes that could be created on samples when the elastomer had undergone a uniform pre-strain. Measurements of the wavelength and amplitude of the wrinkles were taken for samples with an Al capping layer with a thickness in the range of $10 - 500nm$ and a pre-strain on the elastomer of $1 - 60\%$. This study showed that this facile method could produce textured samples with wrinkles that are approximately sinusoidal in shape, with wavelengths in the range $3 - 45\mu m$ and amplitudes of $0.5 - 4\mu m$.

2.3 Theoretical model

In order to assess the quality of the data collected, a model of the system studied had to be developed. Two models of this system will be discussed here. The first

assumes that the amplitudes were small compared to the thickness of the layer [45] (small deflection model), and a second that assumed the amplitudes were large compared to the Al thickness [32] (Song *et al.* model). The Song *et al.* model [32] was selected over the model produced by Huang and coworkers [28–31] due to the experimental confirmation of the model that had been discussed alongside the Song *et al.* model [32]. This showed that the model was relevant to the bilayer system used in this work.

The geometry for both of these models is an aluminium layer deposited on to a pre-strained elastomer substrate. The strain in the substrate is then released and the elastomer layer becomes unstrained while the aluminium layer undergoes a compressive strain and the aluminium wrinkles to reduce this strain.

2.3.1 Small deflection model

The small deflection model considers the stress applied from 3 separate sources, the predicted wavelength was found by balancing these stresses. The 3 sources of stress are:

1. Compressive stress in the Al capping layer caused by the release of the pre-strain applied to the elastomer
2. Stress from bending the Al capping layer
3. Stress in the elastomer layer caused by deformations close to the Al-elastomer interface

These stresses are shown in Figure 2.1.

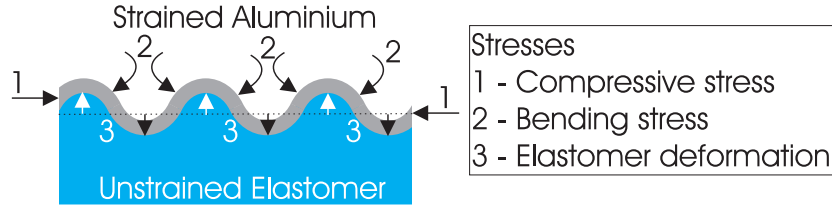


Figure 2.1: Schematic of the wrinkled surface showing the 3 stresses that are considered. These are: 1. Compressive stress acting on the aluminium; 2. Stress from bending the aluminium layer; and, 3. Stress in the elastomer due to deformation.

Compressive Stress in the Aluminium Layer

The local stress applied to the aluminium by the contraction of the PDMS will be equal to the curvature of the aluminium layer multiplied by the thickness and the compressive stress:

$$\sigma_z = \sigma_{cap} h_{cap} \frac{d^2 w}{dx^2} \quad (2.3.1)$$

where σ_{cap} is the compressive stress placed upon the Al capping layer by the release of the pre-strain in the elastomeric substrate.

Since the strain applied to the elastomer is known, we can calculate the strain applied to the aluminium when the pre-strain in the elastomer is released.

We know that the applied pre-strain can be written as, $\varepsilon_{pre} = \frac{\Delta L}{L}$ and that the initial length of the aluminium layer will be $L + \Delta L$. Since the aluminium layer will be compressed by an amount ΔL , then:

$$\varepsilon_{cap} = \frac{\Delta L}{(L + \Delta L)}$$

If the inverse of that is taken:

$$\frac{1}{\varepsilon_{cap}} = \frac{L + \Delta L}{\Delta L} = \frac{L}{\Delta L} + 1$$

Since $\varepsilon_{pre} = \frac{\Delta L}{L}$, then:

$$\frac{1}{\varepsilon_{cap}} = \frac{L}{\Delta L} + 1 = \frac{1}{\varepsilon_{pre}} + \frac{\varepsilon_{pre}}{\varepsilon_{pre}} = \frac{1 + \varepsilon_{pre}}{\varepsilon_{pre}}$$

It then follows that:

$$\varepsilon_{cap} = \frac{\varepsilon_{pre}}{1 + \varepsilon_{pre}}$$

It therefore follows that:

$$\sigma_{cap} = E_{cap}\varepsilon_{cap} = E_{cap}\frac{\varepsilon_{pre}}{1 + \varepsilon_{pre}} \quad (2.3.2)$$

Bending of the Aluminium Capping Layer

Bending of a solid layer, such as the Al capping layer, is generated from a transverse load according to the Euler–Bernoulli beam equation [46]:

$$\frac{F_{bending}}{h_{cap}} = E_{cap}I\frac{d^4w}{dx^4} \quad (2.3.3)$$

where h_{cap} is the thickness of the capping layer, E_{cap} is the Young's modulus of the Al capping layer, w is the out of plane displacement of the Al capping layer, x is a distance along the sample, as shown in Figure 2.2 and, I is the second moment of inertia, which for a beam is given by [45]:

$$I = \frac{bh_{cap}^3}{12} \quad (2.3.4)$$

where b is the width of the sample. Since the cross-sectional area of the aluminium layer is equal to $h_{cap}b$, this corresponds to a stress of:

$$\sigma_{bending} = \frac{F_{bending}}{h_{cap}b} = \frac{E_{cap}h_{cap}^3}{12} \frac{d^4w}{dx^4} \quad (2.3.5)$$

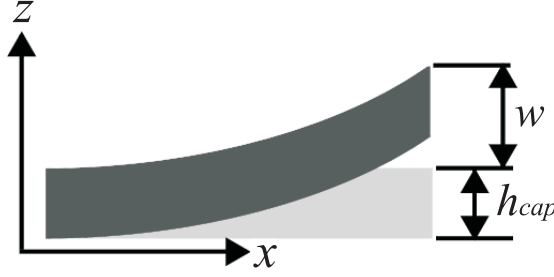


Figure 2.2: Schematic of a bending Al capping layer along with the definitions of the terms from equation 2.3.3. Shown in light grey is the flat unstrained position of the Al capping layer (this is the case before the release of the pre-strain). In dark grey is the position of the Al capping layer once wrinkled (after the release of the pre-strain).

The sum of these 2 stresses (compression of the aluminium layer and bending of the aluminium layer) must be equal to the stress required to deform the surface of the elastomeric substrate ($\sigma_{sub} = \sigma_{bending} + \sigma_{cap}$). This gives:

$$\frac{E_{cap}h_{cap}^3}{12} \frac{d^4w}{dx^4} + \sigma_{cap}h_{cap} \frac{d^2w}{dx^2} = \sigma_{sub} \quad (2.3.6)$$

One solution to this is sinusoidal buckling with a wavelength of λ such that:

$$w = w_m \sin \left(\frac{2\pi x}{\lambda} + \phi \right) \quad (2.3.7)$$

However since the phase of the wrinkles will not be considered, the position, $x = 0$, will be selected such that ϕ can be assumed to be equal to zero. From equations 2.3.3 and 2.3.7, the stress due to the bending of the aluminium can be written as:

$$\sigma_{bending} = \frac{E_{cap}h_{cap}^3}{12(1 + \nu_{cap}^2)} \left(\frac{2\pi}{\lambda} \right)^4 w_m \sin \left(\frac{2\pi x}{\lambda} \right) \quad (2.3.8)$$

Combining equations 2.3.1, 2.3.7 and 2.3.2 can also give the stress from the compression of the aluminium as:

$$\sigma_z = -E_{cap} \frac{\varepsilon_{pre}}{1 + \varepsilon_{pre}} h_{cap} w_m \left(\frac{2\pi}{\lambda} \right)^2 \sin \left(\frac{2\pi x}{\lambda} \right) \quad (2.3.9)$$

Deformation of the Elastomer

The surface of the elastomer must have the same shape as the aluminium layer since they are firmly attached. This means the deformation of the surface of the elastomer is known, and therefore the stress from this deformation can be written as [45, Ch.8]:

$$\sigma_{sub} = - \frac{2\pi E_{sub}}{(3 - \nu_{sub})(1 + \nu_{sub})} \frac{2\pi}{\lambda} w_m \sin \left(\frac{2\pi x}{\lambda} \right) \quad (2.3.10)$$

where E_{sub} and ν_{sub} are the Young's modulus and the Poisson's ratio, respectively, of the elastomeric substrate.

Balancing the Stresses

Considering all of these stresses together 2.3.8, (equations 2.3.9, and 2.3.10) gives:

$$\begin{aligned} E_{cap} \frac{\varepsilon_{pre}}{1 + \varepsilon_{pre}} h_{cap} w_m \left(\frac{2\pi}{\lambda} \right)^2 \sin \left(\frac{2\pi x}{\lambda} \right) = \\ \frac{E_{cap} h_{cap}^3}{12(1 + \nu_{cap}^2)} \left(\frac{2\pi}{\lambda} \right)^4 w_m \sin \left(\frac{2\pi x}{\lambda} \right) \\ + \frac{2\pi E_{sub}}{(3 - \nu_{sub})(1 + \nu_{sub})} \frac{2\pi}{\lambda} w_m \sin \left(\frac{2\pi x}{\lambda} \right) \end{aligned} \quad (2.3.11)$$

By rearranging, the equation becomes:

$$E_{cap} \frac{\varepsilon_{pre}}{1 + \varepsilon_{pre}} \left(\frac{2\pi h_{cap}}{\lambda} \right) = \frac{E_{cap}}{12(1 + \nu_{cap}^2)} \left(\frac{2\pi h_{cap}}{\lambda} \right)^3 + \frac{2\pi E_{sub}}{(3 - \nu_{sub})(1 + \nu_{sub})} \quad (2.3.12)$$

Equation 2.3.12 is a polynomial of order 3 for the variable $\frac{h_{cap}}{\lambda}$. This means that there is a solution for $\frac{h_{cap}}{\lambda}$. Given that the value $\frac{h_{cap}}{\lambda}$ is therefore constant, λ must be proportional to h_{cap} . The roots of this polynomial were found numerically for each strain used and these results were then compared to the data collected.

2.3.2 Large deflection model

A recent theory of wrinkle formation has been developed by Song *et al.* [32]. These authors used a perturbation method to determine that, in the limit of large deflections, the wavelength, λ , and amplitude, A , of the sinusoidal surface wrinkles that are produced when a pre-strain, ε_{pre} , is applied to an elastomer with a thin solid coating of thickness h_{cap} are given by:

$$\lambda = \frac{2\pi h_{cap} \left[\frac{E_{cap}(1-\nu_{sub}^2)}{3E_{sub}(1-\nu_{cap}^2)} \right]}{(1 + \varepsilon_{pre}) \left(1 + \frac{5\varepsilon_{pre}(1+\varepsilon_{pre})}{32} \right)^{\frac{1}{3}}} \quad (2.3.13)$$

$$A = h_{cap} \frac{\sqrt{4\varepsilon_{pre} \left(\frac{E_{cap}(1-\nu_{sub}^2)}{3E_{sub}(1-\nu_{cap}^2)} \right)^{\frac{2}{3}} - \frac{1 + \frac{5\varepsilon_{pre}(1+\varepsilon_{pre})}{96}}{\left(1 + \frac{5\varepsilon_{pre}(1+\varepsilon_{pre})}{32} \right)^{\frac{1}{3}}} (1 + \varepsilon_{pre})}}{\sqrt{1 + \varepsilon_{pre}} \left(1 + \frac{5\varepsilon_{pre}(1+\varepsilon_{pre})}{32} \right)^{\frac{1}{3}}} \quad (2.3.14)$$

where E_{cap} , E_{sub} , ν_{cap} and ν_{sub} are the Young's Moduli and Poisson ratio's of the solid capping layer and elastomeric substrate respectively. This assumes that the hard capping layer is initially in a strain free state while the elastomeric layer is initially under tensile strain. Crucially they allow the capping layer to experience large rotations during the buckling process, something that is not possible using the small deflection model. This model reduces to give the same results as the small deflection model when $\frac{5\varepsilon_{pre}(1+\varepsilon_{pre})}{32} \ll 1$, and there is less than a 1% difference between the two models when the pre-strain drops below 0.2%.

Song *et al.* [32] confirmed the validity of their model by considering the effects of pre-strain on poly(dimethylsiloxane)(PDMS)-silicon bilayer structures. There

are no further studies known, that explore the parameters that govern the sizes of the wrinkles produced by this method in other systems and with different capping layer materials.

This thesis shows that this theory is in good agreement with the experimental results of an aluminium–elastomer bilayer and that a large range of feature sizes were seen, which could cause a range of wettabilities for these surfaces. The range of wettability was confirmed through the use of contact angle measurements which showed that, depending on the feature sizes of the surface, contact angles for sessile water droplets of $90 - 125^\circ$ could be obtained.

2.4 Controlling the wetting properties

In order to drive or direct droplet motion, there must be a gradient in the wetting properties of the surface, with respect to the position. The simplest way to determine if there is a gradient in the wetting properties on any surface is to consider the contact angle as a function of position. The contact angle is determined by the balance of interfacial energies at the contact point. This is demonstrated in Figure 2.3, where the contact angle is defined by the balance of these energies in the plane of the surface of the solid:

$$\gamma_{13} = \gamma_{12} + \gamma_{23} \cos(\theta) \tag{2.4.1}$$

Small ($< 90^\circ$) contact angles indicate surfaces that are easy to wet with water, known as hydrophilic, while large ($> 90^\circ$) contact angles are indicative of surfaces that are not easy to wet, known as hydrophobic surfaces. If there is indeed a change in the contact angle then there may be a large enough force to drive or direct the motion of the droplet. However there may also be some contact angle hysteresis on the surface. This is caused by defects on the surface increasing the contact angle on the leading edge of the droplet while decreasing the contact

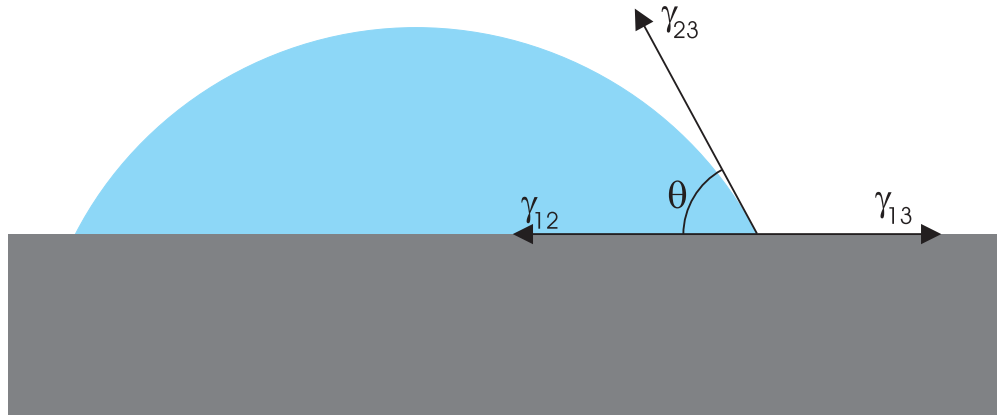


Figure 2.3: Interfacial energies acting on a droplet to determine the contact angle. The 3 interfacial energies are: γ_{12} , the liquid–solid interfacial energy, γ_{13} , the solid–air interfacial energy, and γ_{23} , the liquid–air interfacial energy (also known as the surface tension of the liquid).

angle at the trailing edge of the droplet. These two angles are the minimum and maximum angle that the droplet will exhibit while static, and are known as the advancing (the maximum angle, seen at the leading edge of the droplet) and receding (the minimum angle, seen at the trailing edge of the droplet) contact angles. In order for a droplet to move on the surface, the leading edge of the droplet must exhibit a contact angle equal to the advancing contact angle. If the contact angle is smaller than this, the contact point will pin and the droplet will deform until the contact angle has increased until it equals the advancing contact angle. Once at this angle, the contact point will unpin and the leading edge of the droplet will begin to move. The argument for the trailing edge of the droplet is the same, while the contact angle at this point is larger than the receding contact angle, the droplet will simply deform without the contact point moving until the contact angle is equal to the receding contact angle, at which time it can begin to move. The difference in these angles, known as contact angle hysteresis, means that a spherical droplet on a surface must be deformed before it is possible for it to move. The energy required to do this causes a energy barrier to the motion of droplets on surfaces, as discussed by Gao and McCarthy [47].

In the case of these wrinkled surfaces, there is a change in the contact area between droplets on surface with different lengthscales. This is illustrated in Figure 2.4. For this demonstration, the amplitude has been kept constant and the wavelength has been changed in order to adjust the contact area, however it would be equally as valid to vary the amplitude of the wrinkles, or to adjust both the amplitude and wavelength. The top left frame of Figure 2.4 shows a surface with a large wrinkle wavelength leading to a small contact area. Meanwhile the top right frame shows a surface with a smaller wavelength and consequently a larger contact area. This larger contact area is less energetically favourable than the smaller contact area of the first frame, therefore the droplet changes shape in order to minimise its total energy. This is done by increasing the size of the water–air interface. In order to remain spherical during this change, the solid–water contact area decreases. This consequently increases the contact angle of the droplet on this surface.

If it were possible to create a surface with a gradient in contact area of the droplet, the droplet would have a total energy that was dependent on its position on the surface. This would be visible as a position dependent contact angle and it would cause the droplet to have two different contact angles on either end as shown in the bottom frame of Figure 2.4.

To discover if this would occur, samples with a gradient in the wavelength and amplitude were manufactured. These were created by changing the geometry of the sample such that a gradient in the pre-strain was produced. This in turn created a gradient in the dimensions of the wrinkles that were created upon release of the pre-strain as shown in Chapter 5. Finally these samples were shown to direct the motion of sessile water droplets provided that the droplets were able to sample nearby locations on the surface. This sampling was achieved by vibrating the bi-layer sample close to the resonant frequency of the water droplet causing the contact area between the surface and droplet to change and allowing nearby

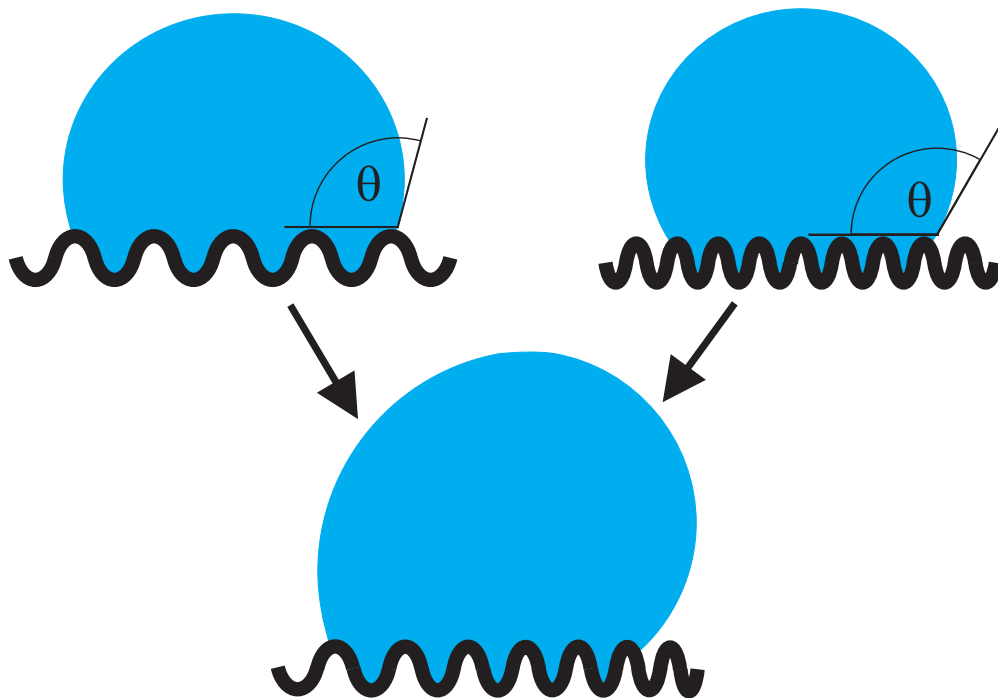


Figure 2.4: Diagrams of sessile water droplets on surfaces with different wavelengths. *Top Left:* an example of a droplet on a large wavelength sample - this droplet has a small contact angle and a small contact area. θ marks the macroscopic contact angle. *Top Right:* An example of a droplet on a small wavelength sample - this droplet has a large contact angle and a large contact area. θ marks the macroscopic contact angle. *Bottom:* An example of a droplet on a surface with a gradient in wavelength - the two visible contact angles are different and the contact area is now a function of the position.

locations to be sampled.

Droplets that were driven by these vibrations were seen to move at speeds in excess of $400\mu\text{ms}^{-1}$, indicating that these samples could be a possible candidate for low cost surfaces with a gradient in wettability.

The use of thin film instabilities to create surfaces with gradients in topography and wettability are also the first of their kind. While previous studies have considered pattern/wrinkle formation in similar systems, the patterns that form have a uniform length scale across the surface of the sample [8, 10, 12, 17, 21, 22]. This thesis describes a novel and facile method of producing samples with a gradient in wrinkle length scales that act as gradient energy surfaces for the biased transport of small liquid droplets.

References

- [1] Y. Sun, V. Kumar, I. Adesida, and J. A. Rogers, “Buckled and wavy ribbons of GaAs for high-performance electronics on elastomeric substrate.,” *Advanced Materials*, vol. 18, pp. 2857–2862, 2006.
- [2] Y. Sun, W. M. Choi, H. Jiang, Y. Y. Huang, and J. A. Rogers, “Controlled buckling of semiconductor nanoribbons for stretchable electronics,” *Nat. Nanotechnol.*, vol. 1, pp. 201–207, 2006.
- [3] D. Y. Khang, H. Q. Jiang, Y. Huang, and J. A. Rogers, “A stretchable form of single-crystal silicon for high-performance electronics on rubber substrate.,” *Science*, vol. 311, pp. 208–212, 2006.
- [4] S. Wang, J. Song, D.-H. Kim, Y. Huang, and J. A. Rogers, “Local versus global buckling of thin films on elastomeric substrates,” *Appl. Phys. Lett.*, vol. 93, p. 023126, 2008.
- [5] A. D. Stroock and G. M. Whitesides, “Controlling flows in microchannels with patterned surface charge and topography,” *Acc. Chem. Res.*, vol. 36, pp. 597–604, 2003.
- [6] J. Y. Chung, J. P. Youngblood, and C. M. Stafford, “Anisotropic wetting on tunable micro-wrinkled surfaces,” *Soft Matter*, vol. 3, pp. 1163–1169, 2007.
- [7] M. T. Lam, W. C. Clem, and S. Takayama, “Reversible on-demand cell alignment using reconfigurable microtopography,” *Biomaterials*, vol. 29, pp. 1705–1712, 2008.
- [8] K. Effimenko, M. Rackaitis, E. Manias, A. Vaziri, L. Mahadevan, and J. Genzer, “Nested self-similar wrinkling patterns in skins,” *Nat. Mater.*, vol. 4, pp. 293–297, 2005.
- [9] C. M. Stafford, C. Harrison, K. L. Beers, A. Karim, E. J. Amis, M. R. VanLandingham, H.-C. Kim, W. Volksen, R. D. Miller, and E. E. Simonyi, “A

- buckling-based metrology for measuring the elastic moduli of polymeric thin films,” *Nat. Mater.*, vol. 3, pp. 545–550, 2004.
- [10] N. Bowden, W. T. S. Huck, K. E. Paul, and G. M. Whitesides, “The controlled formation of ordered, sinusoidal structures by plasma oxidation of an elastomeric polymer,” *Appl. Phys. Lett.*, vol. 75, pp. 2557–2559, 1999.
- [11] J.-H. Wang, C.-F. Chen, J.-R. Ho, T.-K. Shih, C.-C. Chen, W.-T. Whang, and J.-Y. Yang, “One-step fabrication of surface-relief diffusers by stress-induced undulations on elastomer,” *Opt. Laser Technol.*, vol. 41, pp. 804–808, 2009.
- [12] N. Bowden, S. Brittain, A. G. Evans, J. W. Hutchinson, and G. M. Whitesides, “Spontaneous formation ordered structures in thin films of metals supported on an elastomeric polymer,” *Nature*, vol. 393, pp. 146–149, 1998.
- [13] J. S. Sharp and R. A. L. Jones, “Micro-buckling as a route towards surface patterning,” *Adv. Mater.*, vol. 14, pp. 799–802, 2002.
- [14] T. Ohzono and M. Shimomura, “Ordering of microwrinkle patterns by compressive strain,” *Phys. Rev. B*, vol. 69, p. 132202, 2004.
- [15] T. Ohzono and M. Shimomura, “Effect of thermal annealing and compression on the stability of microwrinkle patterns,” *Phys. Rev. E*, vol. 72, p. 025203, 2005.
- [16] T. Ohzono and M. Shimomura, “Geometry-dependent stripe rearrangement processes induced by strain on preordered microwrinkle patterns,” *Langmuir*, vol. 21, pp. 7230–7237, 2005.
- [17] J. S. Sharp, D. Vader, J. A. Forrest, M. I. Smith, M. Khomenko, and K. Dalnoki-Veress, “Spinodal wrinkling in thin-film poly(ethylene oxide)/polystyrene bilayers,” *Eur. Phys. J. E*, vol. 19, pp. 423–432, 2006.

- [18] J. S. Sharp, K. R. Thomas, and M. P. Weir, “Mechanically driven wrinkling instability in thin film polymer bilayers,” *Phys. Rev. E*, vol. 75, p. 011601, 2007.
- [19] A. M. Higgins and R. A. L. Jones, “Anisotropic spinodal dewetting as a route to self-assembly of patterned surfaces,” *Nature*, vol. 404, pp. 476–478, 2000.
- [20] X. Chen and J. W. Hutchinson, “Herringbone buckling patterns of compressed thin films on compliant substrates,” *J. Appl. Mech*, vol. 71, pp. 597–603, 2004.
- [21] J. Genzer and J. Groenewold, “Soft matter with hard skin: From skin wrinkles to templating and material characterization,” *Soft Matter*, vol. 2, pp. 310–323, 2006.
- [22] W. T. S. Huck, N. Bowden, P. Onck, T. Pardoën, J. W. Hutchinson, and G. M. Whitesides, “Ordering of spontaneously formed buckles on planar surfaces,” *Langmuir*, vol. 16, pp. 3497–3501, 2000.
- [23] T.-K. Shih, J.-R. Ho, C.-F. Chen, W.-T. Whang, and C.-C. Chen, “Topographic control on silicone surface using chemical oxidization method,” *Appl. Surf. Sci.*, vol. 253, pp. 9381–9386, 2007.
- [24] P. J. Yoo and H. H. Lee, “Evolution of a stress-driven pattern in thin bilayer films: Spinodal wrinkling,” *Phys. Rev. Lett.*, vol. 91, p. 154502, 2003.
- [25] P. J. Yoo, K. Y. Suh, H. Kang, and H. H. Lee, “Polymer elasticity-driven wrinkling and coarsening in high temperature buckling of metal-capped polymer thin films,” *Phys. Rev. Lett.*, vol. 93, p. 034301, 2004.
- [26] N. Sridhar, D. J. Srolovitz, and Z. Suo, “Kinetics of buckling of a compressed film on a viscous substrate,” *Appl. Phys. Lett.*, vol. 78, pp. 2482–2484, 2001.
- [27] K. Dalnoki-Veress, B. G. Nickel, and J. R. Dutcher, “Dispersion-driven morphology of mechanically confined polymer films,” *Phys. Rev. Lett.*, vol. 82, p. 1486, 1999.

- [28] R. Huang and Z. Suo, “Wrinkling of a compressed elastic film on a viscous layer,” *J. Appl. Phys.*, vol. 91, pp. 1135–1142, 2002.
- [29] R. Huang and Z. Suo, “Instability of a compressed elastic film on a viscous layer,” *International Journal of Solids and Structures*, vol. 39, pp. 1791–1802, 2002.
- [30] R. Huang, “Kinetic wrinkling of an elastic film on a viscoelastic substrate,” *J. Mech. Phys. Solids*, vol. 53, pp. 63–89, 2005.
- [31] S. H. Im and R. Huang, “Evolution of wrinkles in elastic-viscoelastic bilayer thin films,” *J. Appl. Mech.*, vol. 72, pp. 955–961, 2005.
- [32] J. Song, H. Jiang, Z. J. Liu, D. Khang, Y. Huang, J. A. Rogers, C. Lu, and C. G. Koh, “Buckling of a stiff thin film on a compliant substrate in large deformation,” *International Journal of Solids and Structures*, vol. 45, pp. 3107–3121, 2008.
- [33] J. Song, H. Jiang, W. M. Choi, D. Y. Khang, Y. Huang, and J. A. Rogers, “An analytical study of two-dimensional buckling of thin films on compliant substrates,” *J. Appl. Phys.*, vol. 103, p. 014303, 2008.
- [34] M. K. Chaudhury and G. M. Whitesides, “How to make water run uphill,” *Science*, vol. 256, pp. 1539–1541, 1992.
- [35] S. Daniel, S. Sircar, J. Gliem, and M. K. Chaudhury, “Ratcheting motion of liquid drops on gradient surfaces,” *Langmuir*, vol. 20, pp. 4085–4092, 2004.
- [36] S. Daniel, M. K. Chaudhury, and J. C. Chen, “Fast drop movements resulting from the phase change on a gradient surface,” *Science*, vol. 291, p. 633, 2001.
- [37] Y. Ito, M. Heydari, A. Hashimoto, T. Konno, A. Hirasawa, S. Hori, K. Kurita, and A. Nakajima, “The movement of a water droplet on a gradient surface prepared by photodegradation,” *Langmuir*, vol. 23, pp. 1845–1850, 2007.

- [38] L. Qiang, W. Hong, Z. Xun, and L. Mingwei, “Liquid droplet movement on horizontal surface with gradient surface energy,” *Science in China Series E: Technological Sciences*, vol. 49, pp. 733–741, 2006.
- [39] M. L. Ford and A. Nadim, “Thermocapillary migration of an attached drop on a solid surface,” *Phys. Fluids*, vol. 6, p. 3183, 1994.
- [40] Z. Jiao, X. Huang, N.-T. Nguyen, and P. Abrall, “Thermocapillary actuation of droplet in a planar microchannel,” *Microfluids and Nanofluids*, vol. 5, pp. 205–214, 2008.
- [41] Y. T. Cheng, D. E. Rodak, C. A. Wong, and C. A. Hayden, “Effects of micro- and nano-structures on the self-cleaning behaviour of lotus leaves,” *Nanotechnology*, vol. 17, pp. 1359–1362, 2006.
- [42] A. Shastry, M. J. Case, and K. F. Böhringer, “Directing droplets using microstructured surfaces,” *Langmuir*, vol. 22, pp. 6161–6167, 2006.
- [43] G. McHale, N. J. Shirtcliffe, S. Aqil, C. C. Perry, and M. I. Newton, “Topography driven spreading,” *Phys. Rev. Lett.*, vol. 93, no. 3, pp. 6102–6105, 2004.
- [44] J. Zhang and Y. Han, “A topography/chemical composition gradient polystyrene surface: Toward the investigation of the relationship between surface wettability and surface structure and chemical composition,” *Langmuir*, vol. 24, pp. 796–801, 2008.
- [45] H. G. Allen, *Analysis and design of structural sandwich panels*. Oxford : Pergamon, 1969.
- [46] A. P. Boresi, R. J. Schmidt, and O. M. Sidebottom, *Advanced mechanics of materials*. John Wiley and Sons, New York, 1993.
- [47] L. Gao and T. J. McCarthy, “Contact angle hysteresis explained,” *Langmuir*, vol. 22, pp. 6234–6237, 2006.

Experimental Techniques

A model system was chosen to study the wrinkling of the metallic-elastomeric bilayer system. It consisted of a thick film of a silicone elastomer (RS components Ltd, UK), with an aluminium (Al) capping layer. The wrinkling was achieved by the application of a pre-strain to the elastomeric substrate prior to evaporation of the Al capping layer. Due to the different responses of the aluminium and elastomer to the release of this pre-strain, the surface of the samples wrinkled and the properties of the wrinkles were then measured.

This chapter will discuss the methods used to produce these samples along with the experiments used to determine the length scales of the wrinkled bilayers (both wavelength and amplitude) and the wetting properties of these surfaces.

3.1 Sample preparation

These samples were made in four stages.

- Curing of the elastomeric substrate
- Stretching the cured elastomer in order to apply a pre-strain
- Thermal evaporation of a layer of aluminium onto the strained substrate

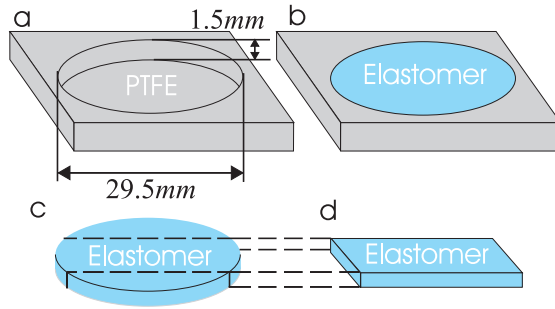


Figure 3.1: a) A schematic of the PTFE mold used to make the elastomer substrates. b) The uncured elastomer was poured into the PTFE mold until it was full. This was left to cure for ≈ 15 hours before being removed. c) The cured disc of elastomer after removal from the mold. d) A strip was then cut from the elastomer disc to be attached to the stretching rig.

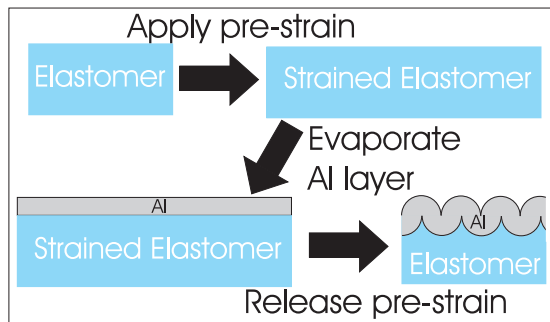


Figure 3.2: Schematic showing the production of wrinkled bilayer samples. A thick elastomer layer was stretched. A thin layer of Al was evaporated onto the strained elastomer layer. The pre-strain was released and the Al layer wrinkled.

- Release of the pre-strain to create the wrinkles

These stages can be seen in Figures 3.1 and 3.2.

3.1.1 Elastomer curing

Thick films of a flowable silicone elastomer (RS components Ltd, UK) were cast by curing the silicone fluid in 29.5mm diameter, 1.5mm deep cylindrical poly(tetrafluoroethylene) (PTFE) molds as shown in Figure 3.1a and 3.1b.

The samples were cured at room temperature for 15 hours. This resulted in the production of $\approx 1mm$ thick disc shaped elastomer samples that were smooth and uniform in thickness as shown in Figure 3.1c.

Finally this disc shaped elastomer sample was cut into a strip ready to be attached to the stretching rig (see Figure 3.1d). This strip was either $10mm$ wide (for the uniform pre-strain samples) or $16mm$ wide (for the gradient pre-strain samples). This difference in width of the strips arose from the differences between the stretching rigs used for making these two types of samples.

The aperture in the stretching rig used to make the uniform samples was a square with sides of $15mm$ in length. In order to ensure no interaction between the elastomer and the sides of the stretching rig, a small gap was left. $10mm$ wide strips of elastomer were therefore chosen as a sensible width to use for the uniform samples.

When making the samples with a gradient in pre-strain, wider strips were used as these allowed a larger range of pre-strains to be applied to the same sample. $16mm$ wide strips were chosen as they allowed a range in pre-strains from $\approx 10\%$ to $\approx 100\%$, whilst still being long enough at the 10% pre-strain end of the sample to allow attachment to the stretching rig.

Uniform Pre-strain Samples

When making uniform strain samples, the disc shaped elastomer samples were cut into $10mm$ wide strips. These samples were then mounted onto a custom built stretching rig by using some additional elastomer as a glue. This can be seen in Figure 3.3. Once this ‘glue’ was cured the pre-strain was applied to the elastomer using the stretching rig (see Figure 3.3).

As shown in Figure 3.3, a pre-strain can be applied by separating the two halves of the stretching rig by a known amount, ΔL . This was done using a micrometer

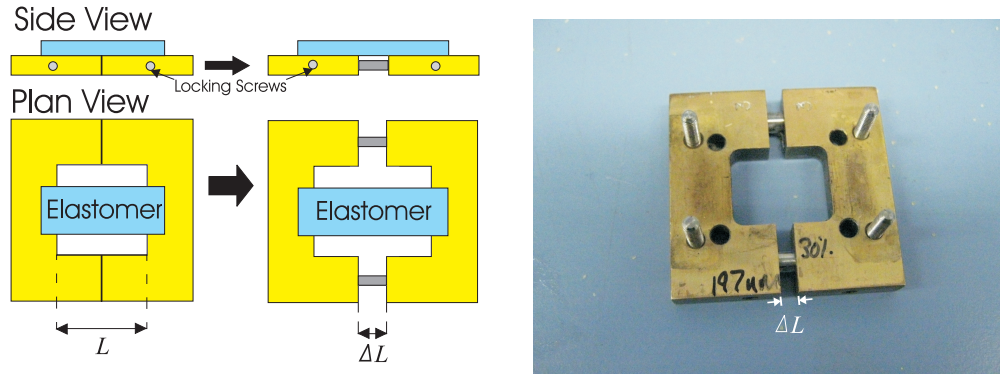


Figure 3.3: *Left and middle* Schematic of the stretching rig used to create samples with a uniform pre-strain. *Left* unstrained sample. *Middle* strained sample. *Right* Photograph of the stretching rig

to enable precision stretching to be carried out. This method gave a pre-strain of $\varepsilon_{pre} = \frac{\Delta L}{L}$, where L is the initial length of the sample. Once the pre-strain was applied, the stretching rig could be locked in place using set screws to ensure the dimensions of the sample could not change.

The stretching rig used was designed to be small enough to fit in a thermal evaporation unit while still allowing pre-strains of up to around 100% to be applied. This meant that the aperture size and therefore the initial length of the sample, L , was chosen to be 15mm . The thickness of the stretching rig was also chosen to allow it to fit beneath the objective of an optical microscope.

Pre-strain values in the range $1\% < \varepsilon_{pre} < 60\%$ were applied to the elastomer samples. The elastomer sample was then ready to be placed in the thermal evaporation unit to be coated with the Al capping layer.

Samples with a strain gradient

From a consideration of equations 2.3.12, 2.3.13 and 2.3.14 the variables upon which the wavelength and amplitude depend are the pre-strain of the elastomer and the thickness of the Al capping layer. In order to create samples with a

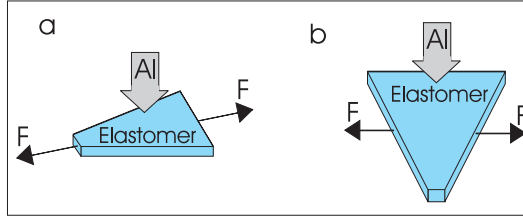


Figure 3.4: Schematic of two possible methods of applying a gradient in the pre-strain of the sample. In both cases the elastomer was of uniform thickness with the aluminium being evaporated onto the side shown. a) Applying a gradient in the cross-sectional area of the elastomer sample in the direction of applied pre-strain. b) applying a gradient in the initial length, L_0 , of the sample. In both images the direction of the force that was used to apply the pre-strain is shown.

gradient in the wavelength and/or amplitude of the wrinkles, samples needed to be made with a gradient in one of these two variables; the local pre-strain, or the local thickness of the Al capping layer. Due to the manual nature of controlling the capping layer thickness with the thermal evaporation unit used, it was decided that we would not get a reproducible thickness profile, and it would therefore be better to apply a strain gradient to the elastomeric substrate.

In order to apply a strain gradient, two methods were considered. Both required a geometric gradient in the sample to be stretched. The first involved creating a gradient in the cross-sectional area of the sample along the direction of the applied strain. This can be seen in Figure 3.4a.

If we consider the formula for strain;

$$\varepsilon = \frac{\sigma}{E} = \frac{F}{AE} \quad (3.1.1)$$

where E is the Young's modulus of the elastomer, σ is the local stress, A is the local cross-sectional area, and F is the applied force. Provided the local force is constant throughout the sample, which it should be in equilibrium, then the local pre-strain depends only on the local cross-sectional area and the force applied in stretching the elastomer. In fact it is inversely proportional to the local cross-

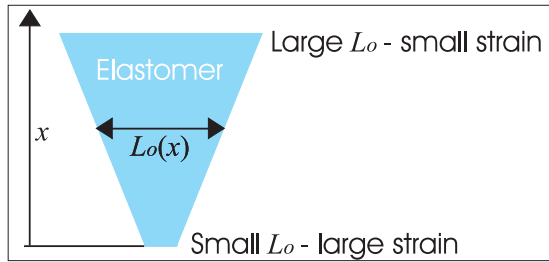


Figure 3.5: Schematic showing how the shape of the sample gives a gradient in L_0 which, in turn leads to a strain gradient when the sample is stretched by a fixed amount, ΔL since $\varepsilon_{pre} = \frac{\Delta L}{L_0(x)}$

sectional area at a given applied force. This gradient in pre-strain should then give rise to a gradient in wrinkle dimensions following the release of the strain.

The second method considered to apply a gradient in the pre-strain, was to apply the pre-strain in a different direction to a similar trapezoidal sample (see Figure 3.4b). In this case the initial length of the sample, L_0 , would vary with position, x , as can be seen in Figure 3.5. If the length is then increased by a fixed amount, ΔL , the pre-strain would be;

$$\varepsilon_{pre} = \frac{\Delta L}{L_0(x)} \quad (3.1.2)$$

where ΔL is the increase in length and $L_0(x)$ is the local initial length of the sample. Since ΔL is constant the pre-strain is only dependent upon the initial length of the sample and therefore a gradient can be produced in the pre-strain. This caused the short end of the sample to have a higher strain than the longer end of the sample, and caused a strain gradient across the sample (see Figure 3.5). In order to apply the pre-strain to samples of this shape, a redesign of the stretching rig was necessary since the two sides of the sample that were attached to the stretching rig were not parallel.

3.1.2 Evaporation

Following the application of the pre-strain, thin capping layers of high purity aluminium (Al, Advent Ltd, UK, 99.999%) with thickness values in the range 20 – 500nm were thermally evaporated on top of the elastomer films. Evaporation was performed under vacuum ($< 10^{-5}$ Torr) at a temperature of $\approx 50^{\circ}\text{C}$. The thickness of the Al capping layer was measured in situ by monitoring changes in the resonant frequency of a quartz crystal that was mounted close to the elastomer sample in the evaporation chamber. The thickness of the Al layers was also calibrated by evaporating films on to single crystal silicon wafers (Compart Technology, UK) and measuring the thickness of a masked region of the film using an Asylum Research MFP-3D scanning force microscope operating in intermittent contact mode.

When the Al capped elastomer samples were removed from the evaporator, the pre-strain in the silicone elastomer was released. Prior to release, the Al capping layer was in a state of zero stress. However, when the elastomer relaxed, the Al capping layer was left in a state of compressive stress. The compression of the thin Al capping layers by the relaxing elastomer layers resulted in the formation of sinusoidal surface wrinkles (see Figures 3.2 and 3.6).

The resultant wrinkles were perpendicular to the direction of the applied pre-strain and had wavelengths in the 3 – 42 micron range and amplitudes in the 0 – 3.6 micron range for pre-strains in the range of 0 – 100% and aluminium capping layers with a thickness in the range of 50 – 500nm.

Figure 3.6 gives examples of the appearance of the surface of Al-elastomer bilayer samples both before and after the release of the pre-strain. Figure 3.6a shows the bilayer sample before the release of the pre-strain, in this image there are small wrinkles apparent upon the surface. These wrinkles are formed during the thermal evaporation process. While evaporating the Al layer onto the elastomer, the temperature within the thermal evaporation unit increases. This has been measured in situ, by the use of a thermocouple embedded within the elastomer,

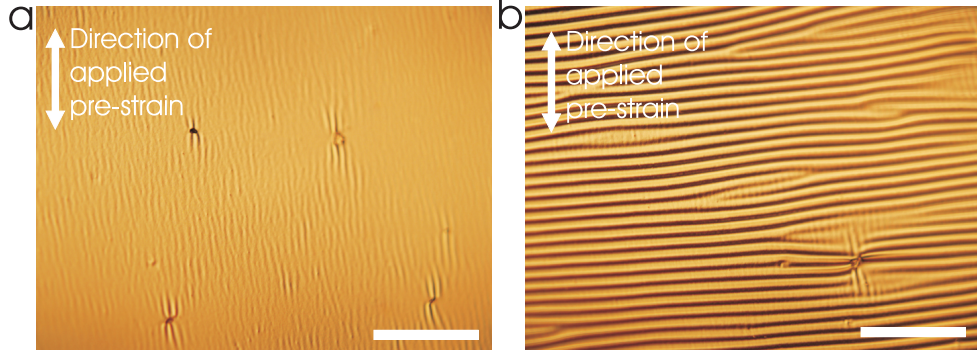


Figure 3.6: a) An example image of a bilayer sample with a pre-strain of 1% and an Al capping layer of 196nm thickness, before the strain was released. The scale bar is $200\mu\text{m}$ long, also shown is the direction of the applied strain. b) An example image of a bilayer sample with a pre-strain of 1% and an Al capping layer of 196nm thickness, after the strain was released. The scale bar is $200\mu\text{m}$ long, also shown is the direction of the applied strain.

to be approximately $25 - 30^\circ\text{C}$ (from room temperature to approximately 50°C). As the bilayer cools, the two layers exhibit a different response to the change in temperature due to their differing coefficients of thermal expansion (much like in a bimetallic strip) and this introduces a strain at the interface between the two layers. The values of the coefficients of thermal expansion, α , for aluminium and the elastomer were found to be $2.3 \times 10^{-5}\text{K}^{-1}$ and $3.1 \times 10^{-4}\text{K}^{-1}$ [1] respectively. This gives a thermally induced strain ($\Delta\alpha\Delta T$) of $\approx 0.7\%$ when $\Delta T = 25^\circ\text{C}$, which causes a small amount of wrinkling to occur.

Once the pre-strain has been released (such as in Figure 3.6b), this thermally induced wrinkling is replaced with wrinkles caused by the mechanical applied strain. This can be seen by a change in the direction of the wrinkles by approximately 90° . The result of this is an additional component to the pre-strain that is not explicitly covered by the models used for comparison with the data. Due to the small size of this additional component ($\approx 0.7\%$) there should be very little effect on samples with a large applied pre-strain. However at low strain (such as 1% as seen in Figure 3.6b) this will have a much larger effect. This can be seen in

Figure 3.6 where some of the thermally produced wrinkles can still be seen, particularly around defects within the Al layer. This is due to the thermally induced strain being comparable to the mechanically applied strain.

3.2 Optical microscopy and image analysis

3.2.1 Optical Microscope

The optical microscope has been around since the early 1600's, although its original inventor is no longer known. Although the design of the optical microscope has been improved over the past 400 years, the basic operation has remained the same. Light is either transmitted through the sample, or reflected from the samples surface. This light is then passed through a series of lenses to focus the light onto a detector; this can be the operator's eye; a photographic film; or, more recently, a digital camera. As well as focusing the light, the lenses are positioned to magnify the resultant image, allowing small details of the sample to be easily seen.

A schematic of the microscope used can be seen in Figure 3.7. The microscope was used in reflectance mode, meaning that the light from the lamp was reflected from the sample before being collected and focused on to the CCD of the digital camera. A ray diagram showing how this can magnify the image is shown in Figure 3.8. In this diagram, the arrow shown on the sample appears much larger in the image plane (the CCD of the digital camera in the case of the Olympus BX51) than its real size on the sample.

The objective lens in Figure 3.8 focuses the light from the sample onto the intermediate image plane. As shown in Figure 3.8, the image in this plane can have some magnification and is inverted with respect to the original sample. The eyepiece, or ocular lens, then focuses the light onto the image plane. It is at this point that the image is viewed, either with the observer's eye, or by placing the

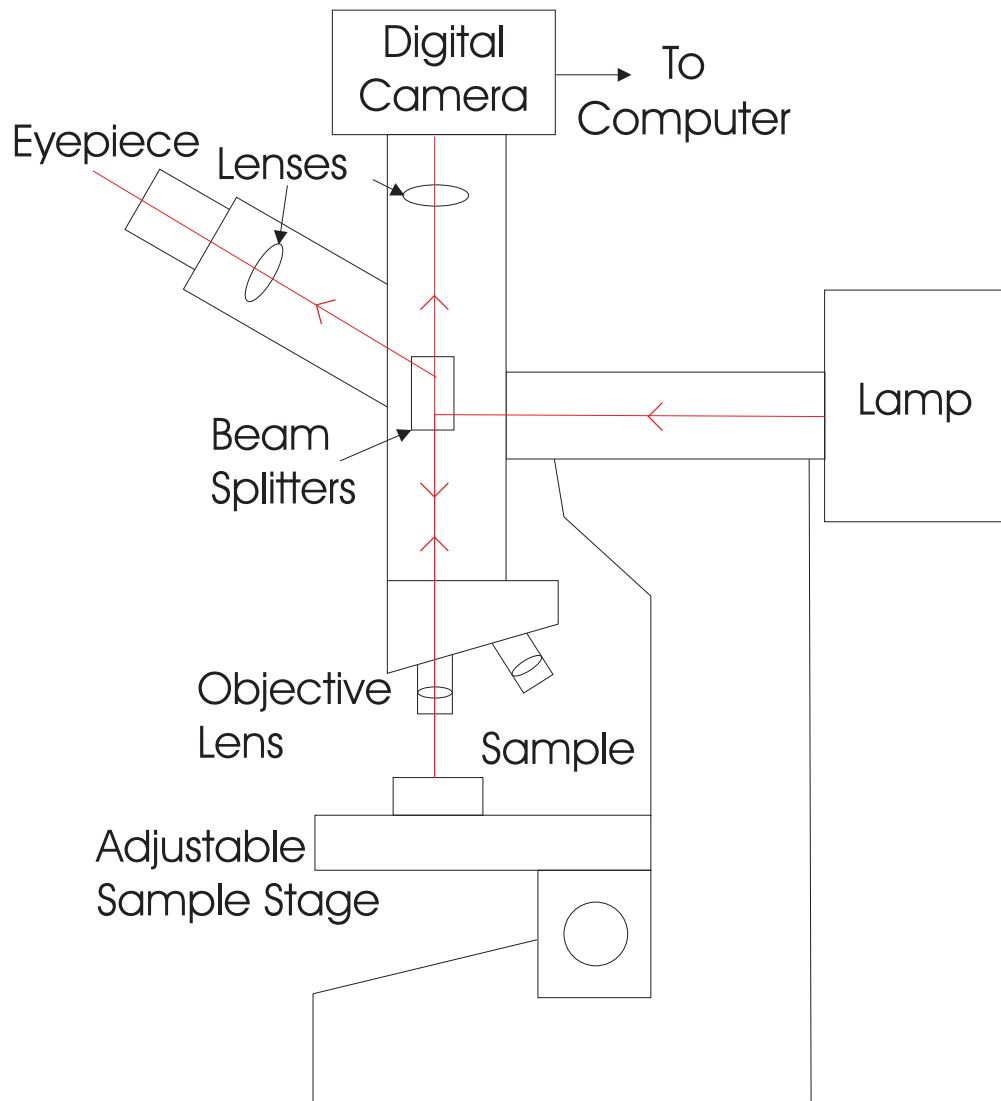


Figure 3.7: Diagram of the microscope used for these experiments. The Olympus BX51 was connected to a computer so that images taken by the digital camera could be saved for later analysis.

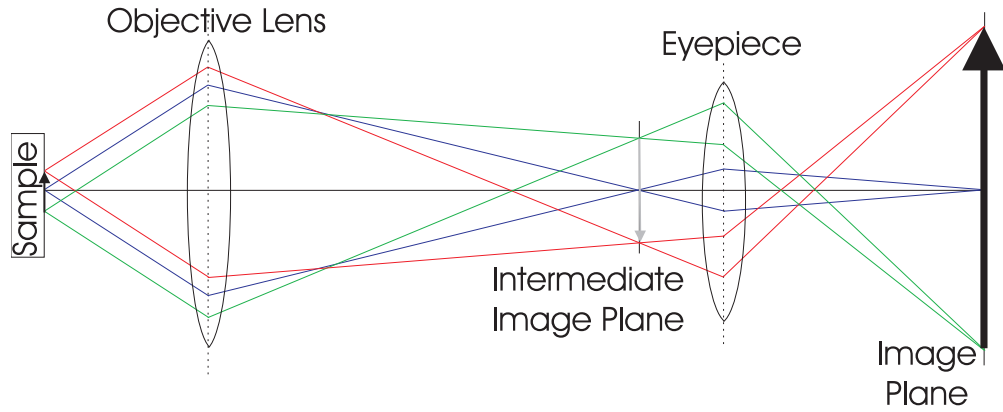


Figure 3.8: Ray diagram showing how 2 lenses can be used to make a simple microscope. The portion of the sample viewed can be seen to appear much larger in the image plane than its size at the sample. This is shown by the 2 arrows in these positions.

CCD of the digital camera in this position. As can be seen in Figure 3.8, a large magnification can be achieved between the sample and the image.

3.2.2 Optical Microscopy

All of the Al capped elastomer samples (both the uniform pre-strain samples and the gradient pre-strain samples) were imaged using an Olympus BX51 optical microscope in reflection using bright field illumination and differential interference contrast (DIC) (see Figure 3.9 for example images of both uniform pre-strain samples and gradient pre-strain samples).

In the images shown in Figure 3.9, two types of features can be seen. Running horizontally in the image are the wrinkles. The peaks and troughs of the wrinkles reflect the most light back through the optics of the microscope and consequently appear as bright lines within the image. In addition to the wrinkles, dark vertical lines can also be seen. These lines are cracks in the aluminium layer. When the strain was applied to the elastomer, due to the finite Poisson ratio, the elastomer contracted in the directions orthogonal to the applied strain. When the strain was

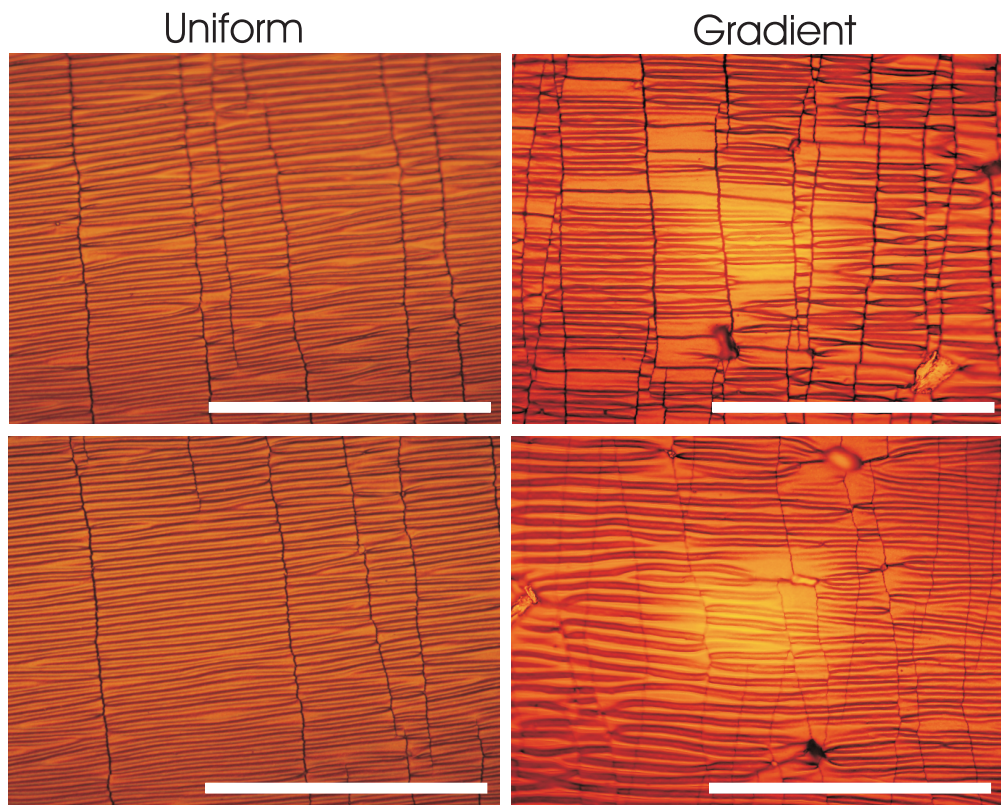


Figure 3.9: *Left* - Optical microscope images two different positions from opposite ends of a sample with a uniform pre-strain of 10% and an Al capping layer of thickness 73nm . *Right* - Optical microscope image of opposite ends of a gradient pre-strain sample with an Al capping layer of thickness 146nm , approximate pre-strain at image location is 30%. All scale bars are $200\mu\text{m}$ long

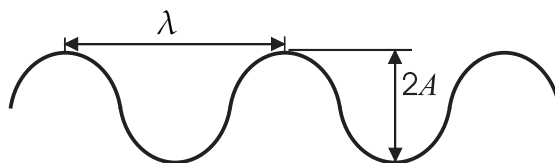


Figure 3.10: Schematic showing how the wavelength, λ , and amplitude, A , of the wrinkles are defined.

released following the application of the aluminium layer, the elastomer returned to its original size causing the aluminium to be stretched in a direction orthogonal to the applied strain. The force applied to the aluminium during the release of the pre-strain was calculated to be $3.165N$ with a pre-strain of 10%. With a capping layer of $100nm$, this caused an estimated stress on the aluminium of $1.5GPa$ which clearly exceeds the yield stress of the aluminium ($15 - 20MPa$ [2]) and therefore caused it to rupture, leaving behind these cracks.

3.2.3 Image Analysis

The wavelength, λ (see Figure 3.10), of the wrinkles on a given sample was obtained by Fourier transformation of the resulting micrographs. An example of this can be seen in Figure 3.11. The wavelength, λ , and its associated uncertainty, $\Delta\lambda$, were initially obtained from the position, k_{max} , and width, Δk , of the dominant peak in the radially averaged Fourier transform (see Figure 3.11c) using the expressions $\lambda = \frac{1}{k_{max}}$ and $\Delta\lambda = \frac{\Delta k}{k_{max}^2}$ respectively.

In order to obtain accurate measurements of the wavelength of different samples, the wave vector, k_{max} , was calibrated for each of the objectives available. This involved imaging a stage micrometer with each of the objectives and using the Fourier transform of the image to find the separation of the lines in pixels. As the separation of the lines on the stage micrometer was known, this provided a calibration between the size of features in the image and the size of the features on the sample.

The measurement of the wavelength was repeated at different locations on the surface of each sample to test the reproducibility of the measured length scales and for the samples with a uniform pre-strain, no difference was found in the wavelength at different locations of a single sample.

It was subsequently discovered that with some samples, particularly those with amplitudes of a similar order to the depth of field of the microscope that there was

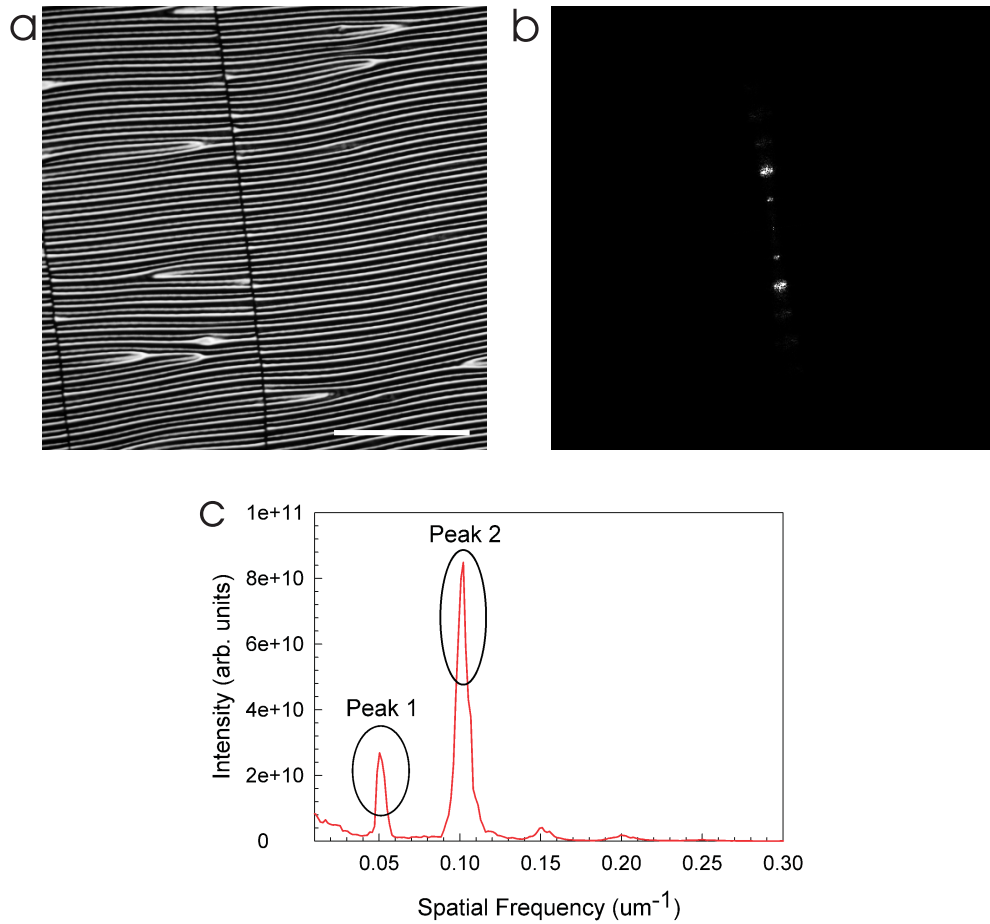


Figure 3.11: a) Optical microscope image of a sample with a uniform pre-strain of 10% and a Al capping layer of 219nm thickness with a $200\mu\text{m}$ scale bar. b) 2D fast Fourier transform of the microscope image, the peaks representing the wrinkled structure can be clearly seen. c) Radial average of the fast Fourier transform with the two important peaks labelled.

a factor of 2 difference between the wavelengths measured using this method and those measured from the scanning force microscopy results. It was also found with samples whose wrinkle amplitudes were slightly larger than the depth of field of the microscope, that it was possible to focus on every second bright line within the image, whilst the rest of the lines were slightly out of focus. There were two focal points at which a set of the bright lines were in focus. The lines that were in focus using the first focal point were found to go out of focus when moving to the second focal point. Meanwhile, the lines that began out of focus, came into focus during the transition between the two focal points. Due to this behaviour, it is believed that bright lines seen within the optical microscope images are both the peaks and the troughs of the wrinkles upon the surface and that the two focal positions are focusing on either the peaks or the troughs, however the depth of field is too small to allow both to be in focus together. This behaviour is shown in Figure 3.12 along with a schematic showing which regions of the surface are in focus in each image. This explains the appearance of the factor of 2 when comparing the optical microscope images to those from the scanning force microscope.

When the positions of peaks 1 and 2 in Figure 3.11c are considered, it turns out that peak 1 corresponds to the same wavelength as measured using scanning force microscopy and peak 2 is equal to half of this value. It is therefore believed that peak 2 gives the spatial frequency of the bright lines within the image while peak 1, gives the spatial frequency of the variation between the trough lines and the peak lines, and this therefore corresponds to the spatial frequency of the wrinkles upon the surface despite being shorter than peak 2. This shows that care must be taken when analysing the radial average of the fast Fourier transform of the optical microscope images.

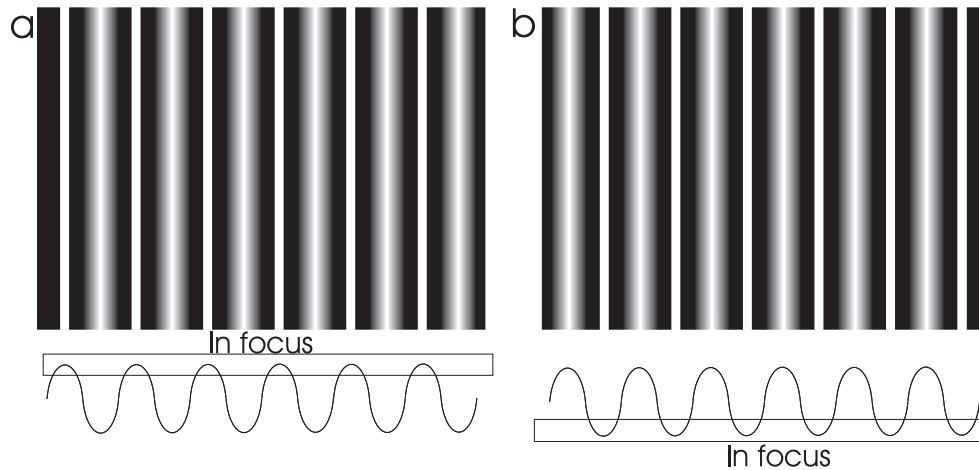


Figure 3.12: Schematic showing how the peaks or the troughs can be in focus. a) The peaks of the wrinkled surface are in focus, the troughs are slightly out of focus. b) When the sample is raised slightly the peaks of the wrinkled surface go out of focus and the troughs come into focus. Beneath each frame is a schematic showing the region of the sample that is in focus.

3.2.4 Selection of a method to make gradient samples

Out of the two methods to make gradient samples that were discussed in Section 3.1.1, the first was initially thought to be the most preferable since it could be done using the existing stretching rig and relied only on producing elastomer sheets with a different shape. However when this method was tested, it was found that there was no variation in the dimensions of the wrinkles upon the sample. In fact the wavelength and amplitude measured were the same everywhere on the samples and were consistent with results obtained from uniform pre-strain samples that had the same global pre-strain (i.e. the same initial length and the same extension). This led to the conclusion that only the global pre-strain is important for determining the wrinkle dimensions and not, as expected, the local pre-strain.

Since the first method did not create gradients in the wavelength and amplitude of the wrinkles, the second method of generating pre-strain gradients (figure 3.4b) was used despite this meaning that a redesign of the stretching rig was necessary.

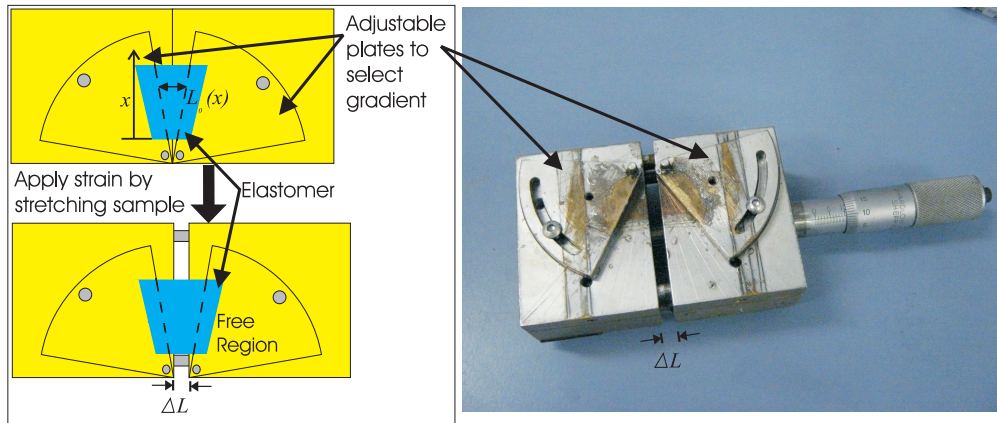


Figure 3.13: Schematic of the stretching rig used to create samples with a gradient in pre-strain. *Top left* The unstrained elastomer is attached to the adjustable plates. The free region of the elastomer has an initial length dependent upon its position within the sample, $L_0(x)$ *Bottom left* The pre-strain is applied by separating the two halves of the stretching rig by an amount, ΔL . The pre-strain applied is dependent upon the position, $\varepsilon_{pre} = \frac{\Delta L}{L_0(x)}$, and the sample therefore has a pre-strain gradient *Right* A photograph of the stretching rig used, the micrometer that was used to measure the strain can be seen to the right of the shot. The amount the sample has been stretched, ΔL , is shown

In order to make the samples with a strain gradient, a 16mm wide strip was cut from the elastomer discs. This was then attached to an adjustable stretching rig that was designed to allow a range of strain gradients to be applied to the sample. This can be seen in Figure 3.13.

3.3 Scanning force microscopy

3.3.1 Scanning force microscope

Binnig, Quate, and Gerber [3] developed the scanning force microscope (SFM) to image non-conducting surfaces at small scales. Since then, the basic principles behind the SFM have remained the same. A sharp tip is attached to the end of a

cantilever which is able to move in 3 dimensions. The deflection of this cantilever is measured to monitor the interaction of the tip with the surface.

In the Asylum Research MFP-3D scanning force microscope, which was used for this work, the deflection of the cantilever is measured using a laser that is reflected from the back of the cantilever onto a detector. The detector consists of two photo-detectors positioned with one above the other. The proportion of light falling on one compared to the other is measured to determine the position of the cantilever.

Contact Mode

The simplest mode in which an SFM can be used is known as contact mode. In this case the tip is brought into contact with the surface that is being scanned and is then dragged across the surface while the deflection of the cantilever is monitored. Throughout the scan, the height of the cantilever is adjusted in order to maintain a constant deflection of the cantilever. The disadvantage of this technique is that it is highly destructive to all but the hardest surfaces.

Intermittent Contact Mode

In order to avoid damage to the aluminium layer, intermittent contact mode SFM was used. In this mode the cantilever is continually oscillated during the scan. As the separation between the tip and the surface is reduced, the amplitude of the oscillation will decrease. By selecting an appropriate target amplitude, the interaction between the tip and surface can be controlled such that it is strong enough to image the surface and yet not so strong as to damage the surface. In this mode the height of the cantilever is adjusted in order to maintain a constant amplitude, and therefore a constant interaction with the surface. This gives an approximation to the height profile of the surface. A schematic of this is shown

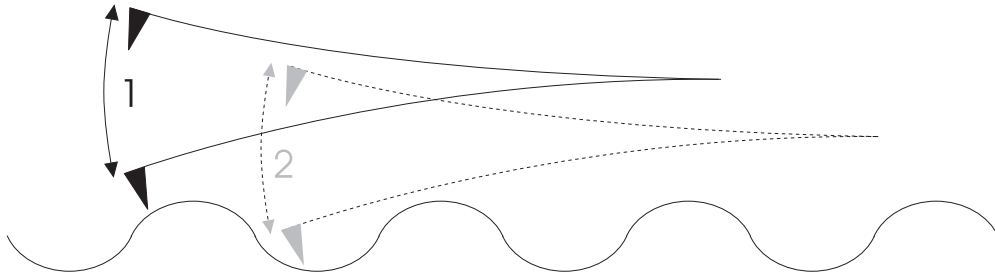


Figure 3.14: Schematic of SFM in intermittent contact mode. 1) The cantilever is oscillating and the feedback loop in the SFM software moves the cantilever until the amplitude of oscillation matches a target value. 2) As the surface is scanned, the cantilever will be moved up or down in order to maintain a constant amplitude.

in Figure 3.14.

3.3.2 Scanning force microscopy

Once the wavelengths of the wrinkles had been measured, the next step was to find their amplitude (A in Figure 3.10). However since the wrinkles are not perfectly sinusoidal, the peak-peak amplitude was measured and halved to obtain an estimate of A (see Figure 3.15).

In order to measure the amplitudes of the wrinkles, the samples were imaged using an Asylum Research MFP-3D scanning force microscope operating in intermittent contact mode. A line profile was taken from the resultant image and an measurements of the amplitude was taken. An example of this can be seen in Figure 3.15

The left hand panel in Figure 3.15 shows an example scanning force microscope image of a sample with a pre-strain of 10% and an Al capping layer of 219nm thickness. On this image is marked the location from which the line profile in the right hand panel of Figure 3.15 was taken. Also shown on the line profile is the peak-to-peak amplitude that was measured. This was done at several locations

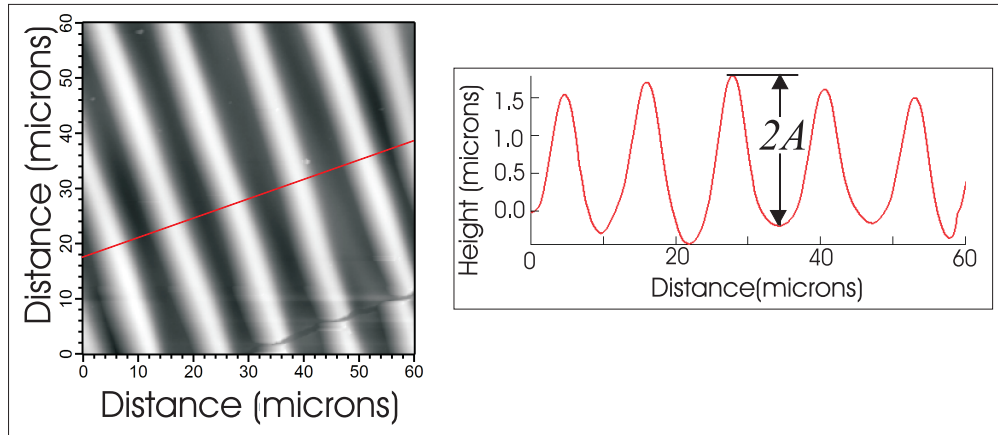


Figure 3.15: *Left* - Scanning force microscope scan of a portion of a wrinkled bilayer sample with a pre-strain of 10% and a 146nm Al capping layer. Shown on the image is the location of the line profile taken to determine the amplitude of the wrinkles. *Right* - Line profile taken from scanning force microscope image showing how the amplitude A is measured.

on each sample to ensure that the samples were uniform.

This process was repeated for both uniform samples and gradient samples. For the gradient samples both the wavelength and amplitude of the wrinkles were measured as a function of position.

3.4 Measuring the wetting properties

In order to find out how the wetting properties of these wrinkled surfaces depended upon the amplitude and wavelength of the wrinkles, the contact angles of sessile water droplets were measured on a range of the uniform pre-strain samples. In particular samples with an Al capping layer of 146nm thickness were considered since these directly corresponded to the gradient samples that were selected for examination.

The set-up used to capture images of the sessile water droplets upon the wrinkled sample was home built and can be seen in Figure 3.16. It consists of a Philips

SPC 1030NC webcam focused on the water droplet which is positioned in front of a white matt screen illuminated with white light. The light reflected from this screen caused a diffuse illumination of the droplet from behind which aided with the imaging of the droplet's profile. The droplet was placed upon the wrinkled sample which was mounted on a small speaker cone. This speaker cone was used to apply a short (approximately 1 second) vibration to the sample at the droplets resonant frequency. This ensured that the droplet was sat on the surface in its relaxed state and not in a metastable state, as the vibration would allow the droplet to experience nearby conformations and find the conformation that had the lowest total energy. Since it was found that a vibration was needed to de-pin the droplets when trying to get them to move (see section 3.5), this was the state that would be the same as the droplet would experience during the droplet motion experiments and therefore these measurements would better represent the wetting properties of the droplet during these experiments.

Once the images had been taken using this set-up, they were analysed using a program written using Matlab (MathWorks) [4]. This program isolated the droplet from the rest of the image and then estimated a fit to the edge of the droplet where it was in contact with the surface of the sample. This in turn gave the contact angle of the droplet on the surface. The uncertainties associated with the contact angles obtained using this method were found to be $\pm 1^\circ$.

Figure 3.17 shows the process used to measure the contact angle from an image taken using this experimental set-up. Firstly the image of the droplet is rotated to ensure that the surface is horizontal within the image. This has been done in Figure 3.17a. The equipment was set up such that the surface should be very close to horizontal in the image already, however this small rotation ensured that this was always the case. Following this the image was binarised. The threshold of the binarisation could be adjusted manually to ensure a good match to the droplet shape. The edges of the binary image were then selected as shown in Figure 3.17b.

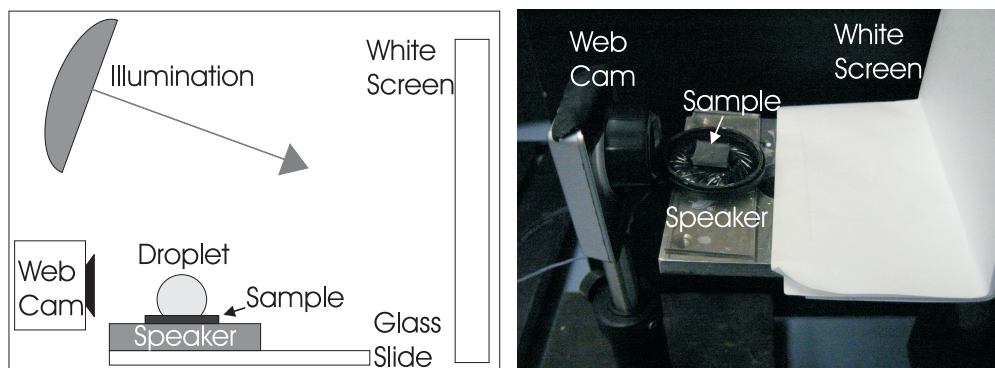


Figure 3.16: *Left* Schematic of the home built set-up used to capture images of sessile water droplets upon wrinkled surfaces. The white screen is illuminated with white light in order to create a disperse light source behind the droplet to aid with imaging the droplet. The sample upon which the droplet was placed was attached to a speaker cone such that a vibration could be applied at the droplets resonant frequency allowing it to fall into its relaxed state. The web-cam was focused upon the droplet and was used to image the droplets profile. *Right* Photograph of the set-up used to take the images for the contact angle measurements

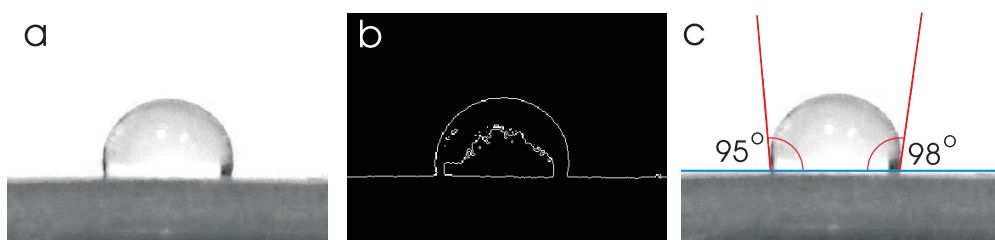


Figure 3.17: a) Example of a droplet upon a gradient surface. Image has been rotated to give a horizontal surface. b) Image has been binarised and the edges of the binary image have been highlighted. c) Lines fitted to contact points between droplet and surface. These are overlaid on the image along with the location of the surface. Also shown are the contact angles at each side of the droplet.

Next the height of the surface within the image was selected, this has been shown in Figure 3.17c. The points where the edges of the binary image intersected the defined surface were then found and assumed to be the contact points. A line was then fitted to the points on the edge of the droplet closest to the surface line. This line was then overlaid onto the original image to allow for a confirmation that it was in the correct place and the contact angle was then calculated as the angle between the fitted line and the horizontal surface line.

3.5 Droplet motion

Provided a change in the contact angle could be seen for different values of the wavelength and amplitude of the wrinkles on the surface, there must be either a different contact area present or a different chemical composition of the surface present. Since the surface should have the same chemical composition in all positions, it was assumed that any changes in contact angle were a result of a change in the contact area. A change in contact angle indicates that there is a change in the droplet's energy at different positions, and an energy gradient gave rise to a force that could be used to drive droplet motion.

The motion of water droplets on the gradient surfaces (along with uniform and flat surfaces for comparison) was studied by placing the speaker/sample set-up from the contact angle measurements under the objective of an Olympus BX51 optical microscope and the droplet on the surface was imaged using a low magnification objective ($\times 5$). The motion of the droplet could then be monitored using software written in Matlab (Mathworks). This software isolated the droplet from the wrinkled surface and calculated an estimate for the position of the centre of the droplet. The position of this point could then be tracked.

It was very quickly found that droplets placed upon the gradient surfaces would not spontaneously move. This means that any possible movement has an energy

barrier that is too high for the droplet to experience motion with only thermal energy. One possible cause of this was that the droplets were seen to pin very easily to defects within the wrinkled structure. These defects include the cracks within the Al capping layer which are present throughout all samples with a pre-strain higher than about 10%. Thermal energy at room temperature was not enough to overcome this pinning and was therefore unable to cause spontaneous movement of the sessile water droplets. In addition to this, contact angle hysteresis may have also been affecting the droplet. This occurs when the receding and advancing contact angles are different. In order for the droplet to move, the contact angle at the leading edge of the droplet must be equal to the advancing contact angle while the contact angle at the rear of the droplet must be equal to the receding contact angle. In order for the droplet to achieve these two different angles it is necessary for the droplet to be deformed prior to moving. The energy required for this process gives an activation energy for the motion of the droplet [5].

In order for any droplet motion to be seen, the droplet needs to experience nearby locations such that it would move to those with a lower total energy. Therefore in order that the droplet was able to sample nearby positions, a harmonic oscillation of the sample at a harmonic of the droplets resonant frequency was created using the speaker. The droplets would then hopefully move to areas with a lower surface energy and thus travel across the surface. In order to have precise control over the nature of the oscillation, software written in Matlab (Mathworks) was used to control the speaker. Once this control was possible, oscillations at a range of frequencies were applied to the sample and water droplet and the average velocity of the droplet as a function of the frequency of the applied oscillation was measured.

Figure 3.18 shows an example of a sessile water droplet on a vibrating surface with a gradient in the pre-strain. The images are in order from left to right with a 2 second interval between them. These images demonstrate that the droplets can

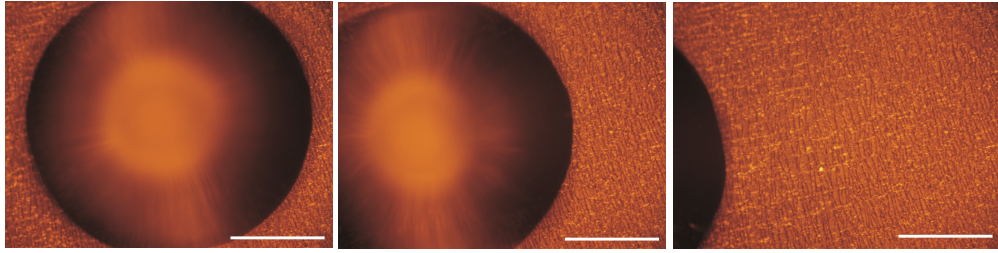


Figure 3.18: Images showing the movement of a $10\mu\text{l}$ sessile water droplet on a gradient surface where the droplet was vibrated close to a harmonic of its resonance frequency. In this case a vibration with a frequency of 210Hz was used. The images were taken in order from left to right with a 2s interval. The average speed of the droplet was over $200\mu\text{m}\text{s}^{-1}$. Scale bar $500\mu\text{m}$.

move on these surfaces. By tracking the position of the droplet it was possible to get a plot of position as a function of time for the droplet during the vibration (See Chapter 7).

The motion of sessile water droplets upon uniform pre-strain surfaces and flat surfaces of the materials in the bilayer (both the elastomer and aluminium) were studied under the same conditions as for the gradient surfaces. Upon these surfaces it was found that there was no preferred direction of motion, and there was often no motion at all. This confirmed that any motion seen that had a clear preferred direction would be due to the gradient in the dimensions of the wavelength and amplitude of the wrinkles and not due to any intrinsic properties of the materials used.

3.6 Measuring the amplitude of the speaker

The voltage signal that was applied to the speaker gave the frequency of oscillation of the speaker, but gave no information as to the amplitude of the oscillation. Without knowing the amplitude as a function of the frequency, it was impossible to distinguish between the resonant frequency of the water droplet and the frequency

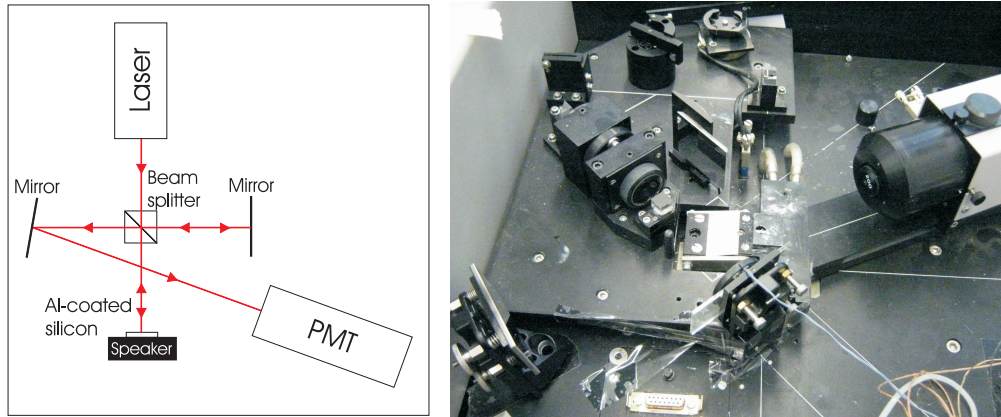


Figure 3.19: *Left* schematic of the interferometry used to measure the oscillation amplitude of the speaker. *Right* Photo of the same set-up.

response of the speaker. In order to determine the frequency response of the speaker, the amplitude of oscillation for voltage signals with a fixed amplitude and a range of frequencies was measured.

In order to measure the amplitude of the oscillation of the speaker, an interferometry set-up was used. This consisted of a laser, a beam splitter, a photomultiplier tube (PMT), and some mirrors to create a Michelson interferometer. An additional mirror was used to guide the laser beam to the PMT due to the limited movement of the detector within the apparatus. An aluminium coated silicon substrate was attached to the speaker to give a highly reflective surface in the position that the bilayer samples would be during the droplet vibration experiments. This set-up is shown in Figure 3.19

When the speaker is oscillating, the path difference between the two paths of the laser will change. Due to this changing path difference, the intensity of the laser spot incident on the PMT will increase and decrease as the path difference causes constructive and destructive interference respectively. Unfortunately the speaker was not moving with a constant speed (due to the sinusoidal vibration) which means that the frequency of the oscillation in the intensity will be not be constant. Instead, the speakers position and therefore the path difference is

changing sinusoidally. This means that a simple analysis of the Fourier transform was not possible. Instead, a model of the oscillation was created that assumed the intensity of the light at the PMT would vary sinusoidally with path difference. The model used for the intensity of the light was;

$$Intensity \propto \cos^2 \left(\frac{\pi PD}{\lambda} \right) \quad (3.6.1)$$

where PD is the path difference and λ is the wavelength of the laser, $633nm$. This model ensured that constructive interference fringes occurred at intervals equal to the wavelength of the laser. The path difference used for this model was the motion of the speaker with an unknown offset, however for the purposes of this model the offset was assumed to be zero as the numbers of fringes passed in one cycle of the speakers oscillation was more important than where in the speakers oscillation the constructive interference occurred. For these reasons the path difference was assumed to be;

$$PD = 2A \sin(2\pi ft) \quad (3.6.2)$$

where A is the amplitude of the speakers oscillation, f is the frequency of the oscillation and t is time. The power spectrum of the intensity profile was then taken, and was found to have the same shape regardless of the frequency and amplitude used. When this was compared to the power spectrum of the intensity seen by the PMT, a similar shape was seen that also exhibited additional harmonics. This comparison can be seen in Figure 3.20

This similarity between the model power spectrum and the measured power spectrum indicated that the simple model used was a good approximation of the speakers motion. The main peak visible within the power spectrum (circled in Figure 3.20) was then used as a reference peak to determine the amplitude of the speakers oscillation. The model power spectrum was calculated for a range

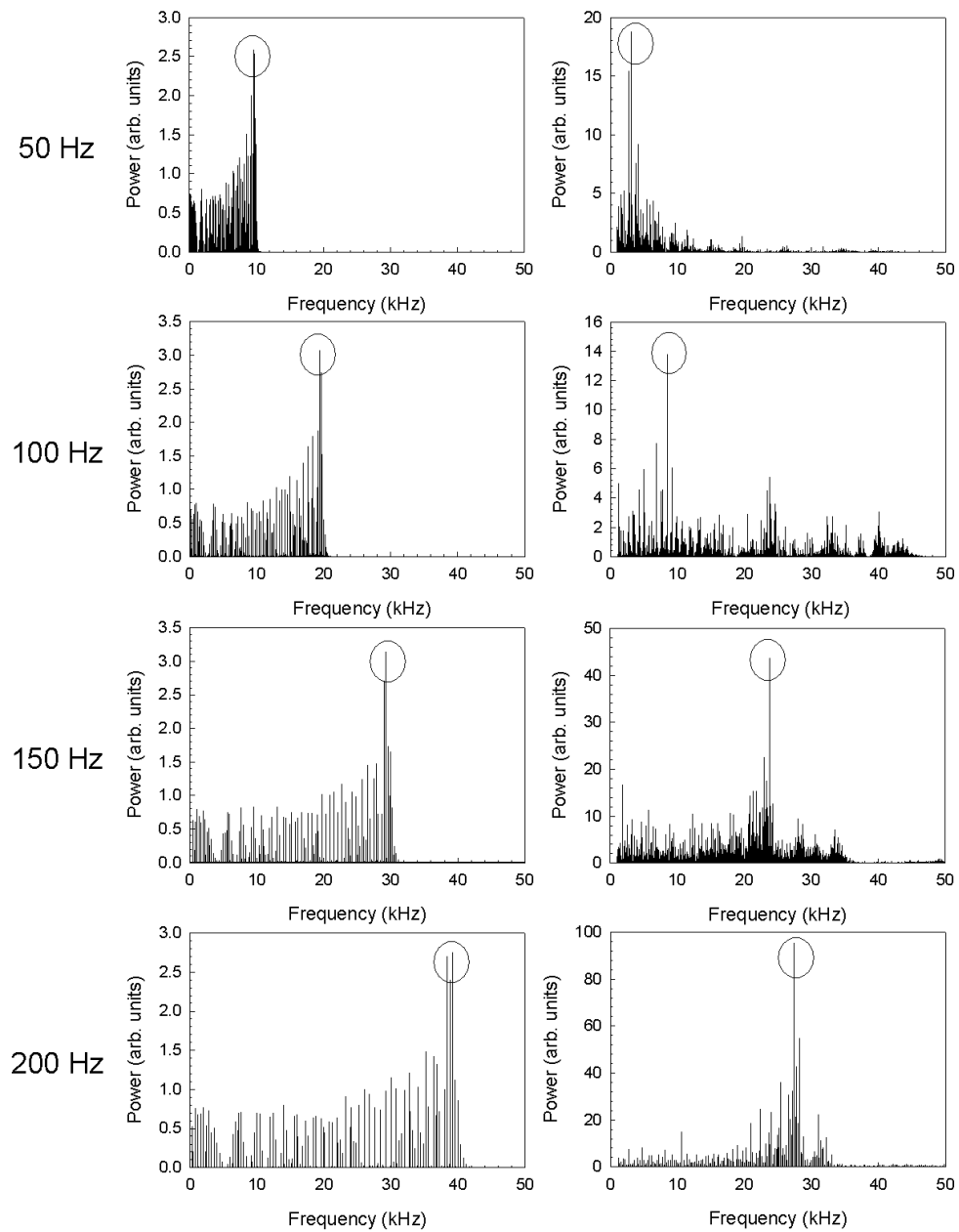


Figure 3.20: *Left:* Power spectrum of the intensity of the light for the simulated oscillation with a peak-peak amplitude of $20\mu\text{m}$ and a range of frequencies from 50Hz to 200Hz *Right:* Power spectrum of the intensity of the light collected at the PMT for a sinusoidal signal with the same frequencies and an amplitude of 1V

of amplitudes and frequencies of the speakers oscillation and a simple analysis was done on the reference peak. This simple analysis used the reference peak to determine the total distance moved during one period of the speakers oscillation if the speaker was moving with a constant speed throughout and this gave the distance, D to be:

$$D = \frac{f_{ref}\lambda}{f}$$

where f_{ref} is the frequency of the reference peak and f is the oscillation frequency of the speaker. Since the speaker moves a total distance of $4A$ during one oscillation (from $+A$ to $-A$ and back again), this gave a first approximation of the amplitude as:

$$A_{approx} = \frac{f_{ref}\lambda}{4f}$$

However due to the more complex behaviour of the speaker, this was found to disagree with the amplitude of oscillation within the model by a factor of $\approx \pi$ for all values of amplitude and frequency. Therefore the amplitude of oscillation, A , was related to the frequency of the reference peak (with a relative error of less than 1%) by;

$$A = \frac{f_{ref}\lambda}{4\pi f} \tag{3.6.3}$$

This equation could then be used to calculate the amplitude of the oscillation of the speaker from the position of the reference peak within the first harmonic of the power spectrum of the intensity of light reaching the PMT. The amplitude of oscillation was then calculated for a range of frequencies up to $300Hz$ and was found to remain approximately constant at a value of $28 \pm 8\mu m$, as can be seen in Figure 3.21 for a selection of frequencies at an input amplitude of $1V$.

Since the oscillation amplitude of the speaker remained approximately con-

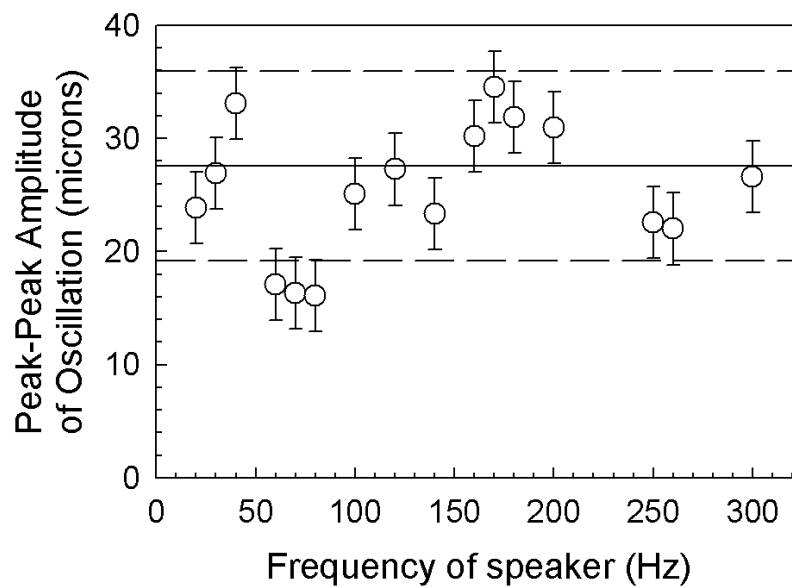


Figure 3.21: The calculated peak-peak amplitude of the speakers oscillation as a function of the frequency of oscillation for a sinusoidal input signal with an amplitude of $1V$. Also shown is the mean (solid line) and 95% confidence limits for the mean (dashed lines).

stant, the peak that was seen in the droplets speed as a function of speaker oscillation frequency could not be due to a peak in the energy input from the speaker and was therefore a result of finding the resonant frequency of the water droplet.

3.7 JKR measurements

From a consideration of equations 2.3.12, 2.3.13 and 2.3.14 it is clear that an important parameter in determining the wrinkle dimensions is the Young's modulus of the elastomer. However the Young's modulus is dependent upon the temperature at which the elastomer is cured and it was therefore necessary to measure the Young's modulus for elastomer that had been cured at the same temperature used to cure the bilayer samples rather than to use a standard value from the literature.

In order to calculate the Young's modulus of the elastomer an axi-symmetric deformation test based upon the method developed by Johnson, Kendall and Roberts [6–8] was used. The samples for these experiments were prepared by curing the silicone elastomer in 11.2mm diameter hemispherical PTFE molds at room temperature for 48 hours. These samples needed a longer curing time than the cylindrical samples used to make the bilayer samples due to an increased thickness. Bilayer samples were made using elastomer substrates that had also been cured for 48 hours and these were found to have the same wrinkle dimensions as those that had been cured for just 15 hours. It was therefore concluded that the total time of the curing had no effect upon the properties of the cured elastomer, provided that sufficient time was allowed for the entire sample to cure. As such it was assumed that although these hemispherical samples had undergone a longer period of curing than the disc shaped samples, they would still have the same value of Young's modulus and indeed no difference was seen in the Young's modulus of hemisphere's that were measured after 48 hours from the start of the curing

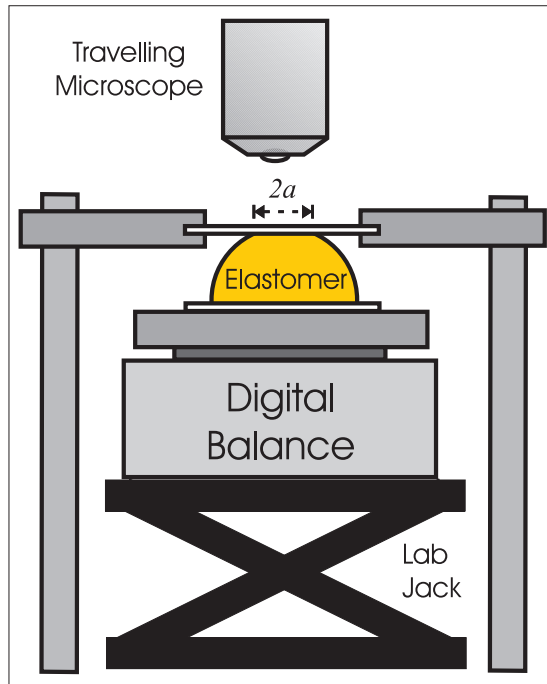


Figure 3.22: Schematic showing the set-up used for the axis-symmetric deformation test. The Lab jack is used to push the elastomer dome into the glass slide. Meanwhile the digital balance measures the force applied to the elastomer dome and the travelling microscope can be used to measure the diameter of the contact patch.

process and others that were measured 2 weeks later.

The samples were then released from the molds and placed on top of a digital balance that was in turn placed on top of laboratory jack (see Figure 3.22). The sample was then raised until it made contact with the bottom surface of a clean glass microscope slide that was coated with a thin uniform layer of the silicone elastomer (prepared by spin coating). At this point a circular contact patch developed between the hemispherical elastomer sample and the silicone coated glass slide and a force was measured by the digital balance. The radius of the contact patch, a , was varied by adjusting the height of the laboratory jack and measured using a travelling microscope. For each value of a , a measurement of the applied load, F , was obtained using the digital balance.

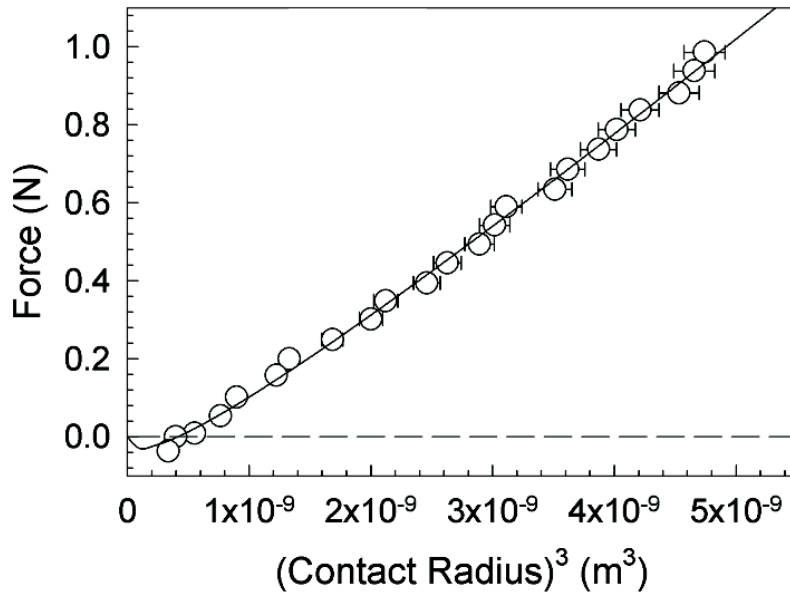


Figure 3.23: An example of data generated from the axi-symmetric deformation test used to determine the Young's modulus of the elastomer. A fit of these data to equation 3.7.1 gives $E = 2.11 \pm 0.08 \text{ MPa}$ and $G = 1.1 \pm 0.8 \text{ Jm}^{-2}$. The fit is shown on the graph as a solid line.

Using this technique the applied load is related to the contact radius by the equation [8]

$$F = \frac{16Ea^3}{9R} - \left(\frac{32\pi EGa^3}{3} \right)^{\frac{1}{2}} \quad (3.7.1)$$

where R is the radius of the hemisphere and G is the work of adhesion (Jm^{-2}) between the hemisphere and silicone coated glass surfaces.

The force can then be plotted as a function of the contact patch radius cubed, a^3 , and this can be fitted to equation 3.7.1 to obtain values for both the Young's modulus, E , and the work of adhesion, G . An example of this is shown in Figure 3.23.

References

- [1] A. Govindaraju, A. Chakraborty, and C. Luo, “Reinforcement of PDMS masters using SU-8 truss structures,” *Journal of Micromechanics and Microengineering*, vol. 15, pp. 1303–1309, 2005.
- [2] A. M. Howatson, P. G. Lund, and J. D. Todd, *Engineering Tables and Data*. Kluwer Academic Publishers, 1991.
- [3] G. Binnig, C. F. Quate, and C. Gerber, “Atomic force microscope,” *Phys. Rev. Lett.*, vol. 56, pp. 930–933, 1986.
- [4] “Automated contact angle measurement programme.” provided by Michael Smith, University of Edinburgh 2009.
- [5] L. Gao and T. J. McCarthy, “Contact angle hysteresis explained,” *Langmuir*, vol. 22, pp. 6234–6237, 2006.
- [6] K. L. Johnson, *Contact Mechanics*. Cambridge University Press, 1985.
- [7] D. Maugis, *Contact Adhesion and Rupture of Elastic Solids*. Springer, Berlin, 1934.
- [8] K. R. Shull and W. Chen, “Fracture mechanics studies of adhesion in biological systems,” *Interface Science*, vol. 8, pp. 95–100, 2000.

Wrinkle Formation in Aluminium-Elastomer Bilayers

The first samples that were considered were the uniform pre-strain samples. These were created with no gradient in pre-strain and with a uniform Al capping layer thickness. These were the simplest samples to study as the properties of the wrinkles (wavelength and amplitude) were constant across the entire sample. As such every study done was at a precisely defined pre-strain with a precisely defined Al thickness.

In order to calculate the predicted values for the wavelength and amplitude from these two models, the Young's Modulus and Poisson ratio of the elastomer layer and aluminium layer needed to be found. The Poisson ratio of the elastomer was assumed to be close to 0.5 [1], while the Poisson ratio for aluminium is widely reported to be 0.334 [2]. The value of E_{sub} of the silicone elastomer was measured using the axi-symmetric deformation tests that were based upon the method developed by Johnson, Kendall and Roberts [3–5], as discussed in Chapter 3. Figure 3.23 shows the data collected and the fit that was used to calculate both the Young's modulus of the elastomer and its surface energy.

The data shown in Figure 3.23 were fit to equation 3.7.1 to find the Young's modulus and the surface energy. The Young's modulus of the elastomer obtained

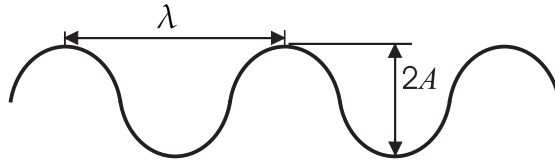


Figure 4.1: Schematic showing how the wavelength, λ , and amplitude, A , of the wrinkles are defined.

from these measurements was $E = E_{sub} = 2.11 \pm 0.08 MPa$. This was found to be in agreement with the range of values quoted for silicone elastomers [1]. A value for the work of adhesion between the silicone hemisphere and the silicone coated glass surface was also obtained and was found to be $G = 1.1 \pm 0.8 Jm^{-2}$. When this is compared to the value found by Silberzan, Perutz, and Kramer [6] of $328 \pm 3mJm^{-2}$, it is found that the value measured is the same within error, however, it has a large associated error due to a low number of data points taken at low loads. Although this leads to an inaccurate measurement of G , the decision not to repeat these measurements was taken since the aim was to acquire the Young's modulus and not the adhesion energy.

The value that was used for the Young's Modulus of the evaporated Al capping layers, E_{cap} , was 30 GPa and not the bulk value for aluminium (70 GPa). This was done because Read *et. al* [7] have shown that in evaporated thin films the Young's modulus of Al is reduced due to the presence of small Al grain sizes within thin aluminium films. These smaller grains can move and align much more easily than larger grains. The effect of this means that for a comparable strain, the stress is much lower than for bulk aluminium, which in turn causes a decrease in the Young's modulus.

Throughout this chapter and future chapters, the wavelength, λ , and the amplitude, A , of the wrinkles will be defined as shown in Figure 4.1

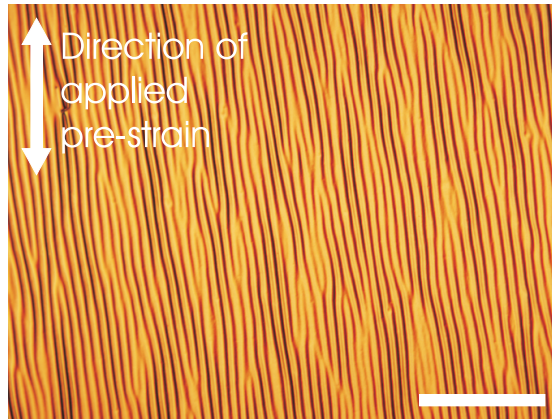


Figure 4.2: An example of the wrinkles that can be seen following removal of the bilayer sample from the thermal evaporation unit, but prior to release of the pre-strain. The scale bar is $200\mu m$ long. Also shown is the direction of the applied pre-strain.

4.1 Thermally induced wrinkles

Once the bilayer samples were removed from the thermal evaporation unit, some wrinkling was observed prior to the release of the pre-strain. An example of this can be seen in Figure 4.2.

During the evaporation process, the bilayer sample is heated. During the subsequent cooling of the bilayer substrate, the mismatch in thermal expansion coefficient between the elastomer and the Al cause a strain to occur at the interface between the two layers, much like the mechanically applied strain discussed previously. In order to release this strain the Al layer wrinkles in a sinusoidal pattern.

Under zero strain conditions, these thermally induced wrinkles would have no preferred direction. However the introduction of the pre-strain causes the wrinkles to align close to the direction of the applied pre-strain.

This occurs because when the elastomer is heated, it would usually expand in all directions. However if it is strained in one direction, this increases the Young's Modulus of the elastomer [8]. Meanwhile in all other directions the expansion

will be seen as normal. When the elastomer-Al bilayer then cools, there is no movement of the elastomer in the direction of the strain, only a decrease of the Young's modulus back to its original value [8].

Since the coefficient of thermal expansion of aluminium is low relative to that of the elastomer, the aluminium's length remains approximately constant during the cooling. Since almost no change in length has occurred for the aluminium or the elastomer, very little stress has been created along the interface and consequently no wrinkles occur along that axis. For all orthogonal directions however, there has been an increase in the length of the sample, when the sample cools this causes a subsequent decrease in the length of the elastomer which causes a compressive stress to be applied to the aluminium layer. This causes highly aligned wrinkles whenever there is a strain on the underlying elastomer, due to the highly directional stress applied to the aluminium during the cooling of the pre-strained sample.

Since the thermal strain induced during the cooling of the sample was $\varepsilon_T = \Delta\alpha\Delta T$ the model proposed by Song *et al.* [9] gives the thermally induced wrinkle wavelength and amplitude as:

$$\lambda = \frac{2\pi h_{cap} \left[\frac{E_{cap}(1-\nu_{sub}^2)}{3E_{sub}(1-\nu_{cap}^2)} \right]}{(1 + \Delta\alpha\Delta T) \left(1 + \frac{5\Delta\alpha\Delta T(1+\Delta\alpha\Delta T)}{32} \right)^{\frac{1}{3}}} \quad (4.1.1)$$

$$A = h_{cap} \frac{\sqrt{4\Delta\alpha\Delta T \left(\frac{E_{cap}(1-\nu_{sub}^2)}{3E_{sub}(1-\nu_{cap}^2)} \right)^{\frac{2}{3}} - \frac{1 + \frac{5\Delta\alpha\Delta T(1+\Delta\alpha\Delta T)}{96}}{\left(1 + \frac{5\Delta\alpha\Delta T(1+\Delta\alpha\Delta T)}{32} \right)^{\frac{1}{3}}} (1 + \Delta\alpha\Delta T)}}{\sqrt{1 + \Delta\alpha\Delta T} \left(1 + \frac{5\Delta\alpha\Delta T(1+\Delta\alpha\Delta T)}{32} \right)^{\frac{1}{3}}} \quad (4.1.2)$$

In order to compare the results from this against equations 4.1.1 and 4.1.2, the values of $\Delta\alpha$ and ΔT needed to be found. ΔT was found by embedding a thermocouple within an elastomer strip. The temperature was then monitored throughout the evaporation and it was discovered that the highest temperature achieved was approximately 25K above room temperature. Therefore $\Delta T \approx 25K$.

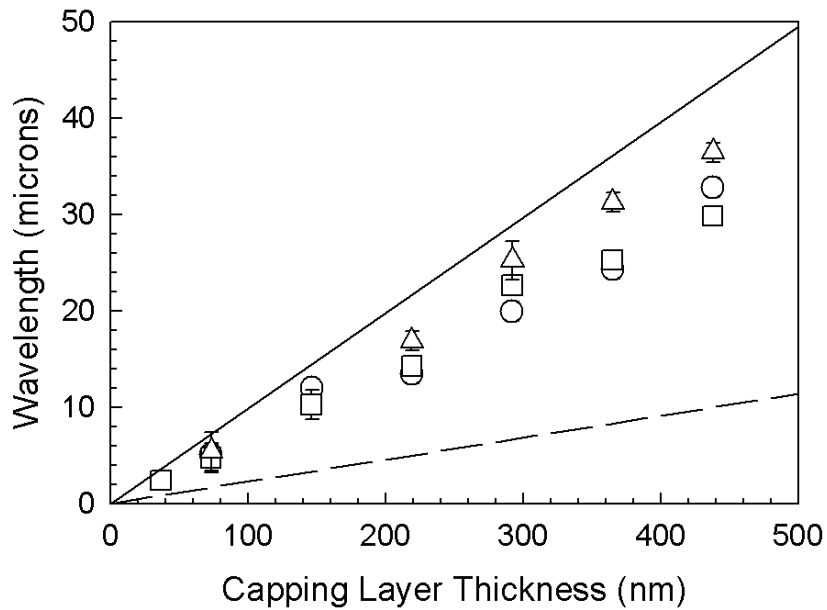


Figure 4.3: The wavelength of thermally produced wrinkles as a function of Al capping layer thickness for three values of the pre-strain, 1%(○), 10%(□) and 50%(△). Also shown are the predictions for the wavelength using the Song *et al.* model [9] (solid line) and the small deflection model (dashed line).

The values of α for aluminium and the elastomer were found to be $2.3 \times 10^{-5} K^{-1}$ and $3.1 \times 10^{-4} K^{-1}$ [10] respectively. The wavelengths of these thermally produced wrinkles were measured as a function of both pre-strain and Al capping layer thickness. The results of these measurements and the model predictions using the Figures discussed above, can be seen in Figure 4.3.

Figure 4.3 shows little dependence on the pre-strain of the elastomer. This was expected since the relative thermal expansion of the Al capping layer and the elastomer layer should be the same regardless of the applied pre-strain. There is however some discrepancy between the wavelengths predicted by the Song *et al.* model [9] and the measured wavelengths. This could be due to a large temperature gradient within the elastomer. Since the temperature was measured with a thermocouple embedded within the elastomer rather than at the interface between the elastomer and the aluminium, it is not currently known what temperature gradi-

ent was present during the evaporation process, and as such a higher temperature may have been reached at the interface between the two layers than was measured. This higher temperature would cause a higher strain within the elastomer which would in turn cause a reduction in the wavelength, which was not accounted for in the model.

4.2 Dependence on the thickness of the aluminium capping layer

Figure 4.4 shows the measured values of the wavelength of wrinkles on samples with uniform strain at a range of pre-strain values as a function of the Al capping layer thickness along with the predicted wavelengths given by the small deflection model (equation 2.3.12). As is expected, the wavelength increases with increasing thickness of the aluminium capping layer. Thicker layers need more energy to bend and they therefore have a larger radius of curvature with the same applied pre-strain. This increase in radius of curvature gives a larger wavelength.

It can be seen in Figure 4.4 that the small deflection model is not in good agreement with the wavelengths that were measured. The main assumption with that model was that the amplitude of the wrinkles was small with respect to all other lengthscales within the system, in particular the amplitude would need to be small compared to the thickness of the Al capping layer since this is the smallest dimension of the sample. In order to discover if this was the case the amplitude of the wrinkles (as measured by scanning force microscopy) was compared to the Al capping layer thickness. This can be seen in Figure 4.5.

Figure 4.5 clearly shows that the amplitude of the wrinkles is around 5-10 times larger (depending on the pre-strain) than the thickness of the Al capping layer. As such it cannot be assumed that there are only small deflections within the wrinkled structure, and as such this model was not considered further as its

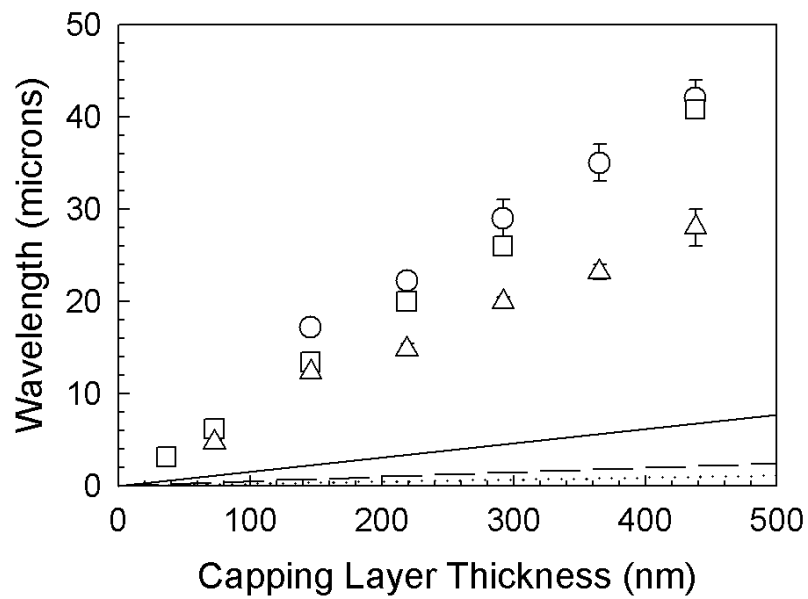


Figure 4.4: Al capping layer thickness dependence of the wrinkle wavelength measured for pre-strains of 1%(○), 10%(□), and 50%(△) respectively. Also shown are the predictions of the Small deflection model for pre-strains of 1%(—), 10%(- -), and 50%(···).

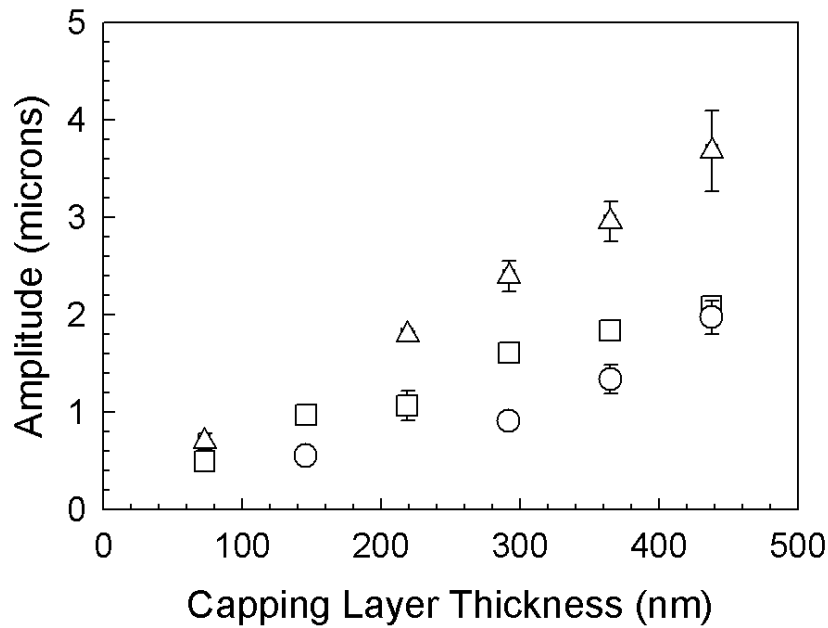


Figure 4.5: Al capping layer thickness dependence of the wrinkle amplitude, as measured using scanning force microscopy, for pre-strains of 1%(○), 10%(□) and 50%(△) respectively.

assumptions could not be applied to the system used.

The model proposed by Song *et al.* [9] was compared to the experimental results to find whether it performed better than the small deflection model or not.

Shown in Figure 4.6 are the predicted values as given by the Song *et al.* model [9] compared against the measured wavelengths (top frame) and amplitudes (bottom frame) for a range of uniform pre-strain samples.

Good quantitative agreement between experiment and calculations of the wrinkle wavelengths and amplitudes can be seen in most cases. The only exception to this is the difference between the amplitude data for samples with 1% pre-strain and the predictions of the model by Song *et al.* [9] that are shown in Figure 4.6. The differences that are observed at this low pre-strain are likely to be due to uncertainties in the strain that arise due to thermal expansion of the elastomeric substrate during the evaporation of the Al. However, small varia-

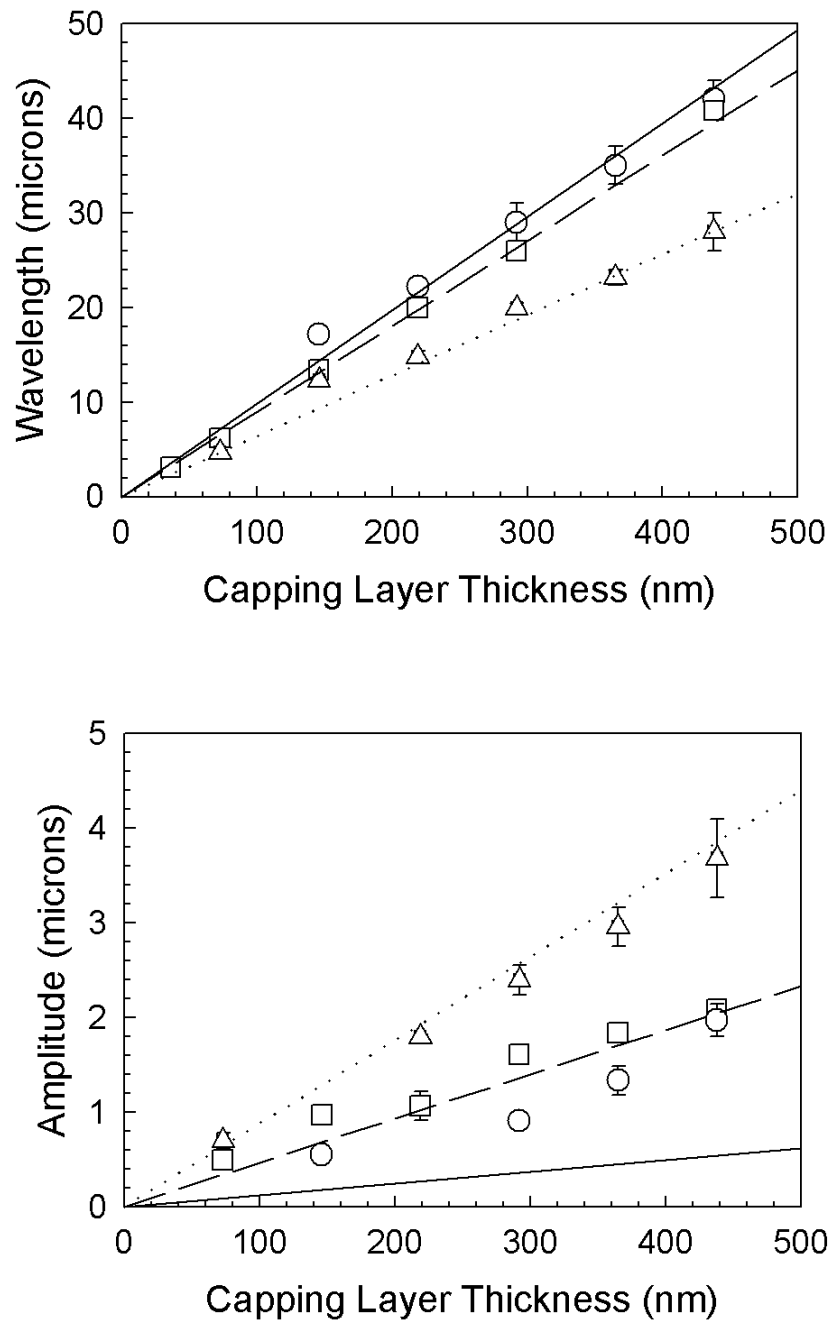


Figure 4.6: Al capping layer thickness dependence of the wrinkle wavelength (*Top*) and amplitude (*Bottom*) measured for pre-strains of 1%(○), 10%(□) and 50%(△) respectively. Also shown are the predictions of the Song *et al.* model [9] for the same pre-strains; 1%(—), 10%(- -), and 50%(⋯).

tions/uncertainties in the applied pre-strain may also have a measurable effect in this regime. Thermal expansion is expected to change the effective pre-strain in the elastomer. After the Al capping layer was deposited, the samples cooled and the strain was released, there was an additional component of the applied strain which occurs due to the mismatch in thermal expansion coefficients of the Al and the elastomer. This difference in thermal expansion coefficients $\Delta\alpha$ is expected to introduce an additional thermal strain within the Al of order $\varepsilon_T = \Delta\alpha\Delta T$, where ΔT is the change in temperature of the elastomer and Al capping layer during thermal evaporation of the Al layers.

Typical values for the expansion coefficients of Al and silicone elastomers were found to be $2.3 \times 10^{-5} K^{-1}$ and $3.1 \times 10^{-4} K^{-1}$ [10] respectively and the rise in temperature in the sample was measured, in situ, to be $\approx 25K$. This gives a value for the thermal strain of 0.7%. This is comparable to the 1% pre-strain that was applied to the samples. Calculations based upon equations 2.3.13 and 2.3.14 show that the change in strain caused by the temperature difference is expected to increase the amplitude of the surface corrugations/wrinkles on the samples with a 1% pre-strain by a factor of ≈ 1.3 and to decrease the wavelengths by a factor of 0.99. These Figures were calculated using the Song *et al.* model [9] with a thermal strain of $\varepsilon_T = \Delta\alpha\Delta T$ in addition to the applied pre-strain. The values of wavelength and amplitude were then compared to calculations that did not include the additional thermal strain terms.

At pre-strains of 10% and higher, similar calculations show that the effects of thermally induced strains on both the measured amplitudes and wavelengths are expected to be negligible. The observed differences between the 1% pre-strain amplitude data and the Song *et al.* model [9] are clearly larger than these predictions by a factor of $\approx 2 - 3$. Calculations based upon the results obtained for the amplitudes of the samples with 1% pre-strain shown in Figure 4.6 suggest that the uncertainty in the effective applied strain due to changes in temperature as

well as the uncertainty in the applied pre-strain are as high as $\pm 3\%$.

4.3 Dependence on the applied pre-strain

At pre-strain values of around 10% and above some cracking of the Al layer occurs. Above a pre-strain of around 40%, this cracking becomes even more pronounced. This can be seen in Figure 4.7 in optical micrographs taken with an Olympus BX51 optical microscope using bright field illumination and differential interference contrast (DIC) using a $\times 20$ objective. All of this cracking occurs parallel to the direction of the applied pre-strain and was attributed to yield processes in the Al capping layers. The crack density was observed to increase with the magnitude of the applied pre-strain.

As can be seen in Figure 4.7, cracking of the Al layer begins at a pre-strain of around 10% and the density of the cracks increases with increasing pre-strain up to around 40% pre-strain. Up until this point the major contribution to surface texture is the wrinkling pattern of the bilayer structure. However at a pre-strain of around 40%, the dominant pattern starts to come from the cracking of the aluminium layer rather than the wrinkles from the bilayer structure.

This increase in the wrinkle density is plotted as a function of the pre-strain in Figure 4.8. This Figure shows that as the pre-strain increases, the additional force applied to the aluminium during the release of the pre-strain causes additional cracking to occur.

As well as controlling the number of cracks, the pre-strain also affects the amplitude and wavelength of the wrinkles. Figure 4.9 shows the dependence of both the amplitude and wavelength of the wrinkles as a function of the applied pre-strain for samples of uniform strain with an Al capping layer of thickness 219nm . Again the predictions from the Song *et al.* model [9] are shown, wavelength with a solid line and amplitude with a dashed line.

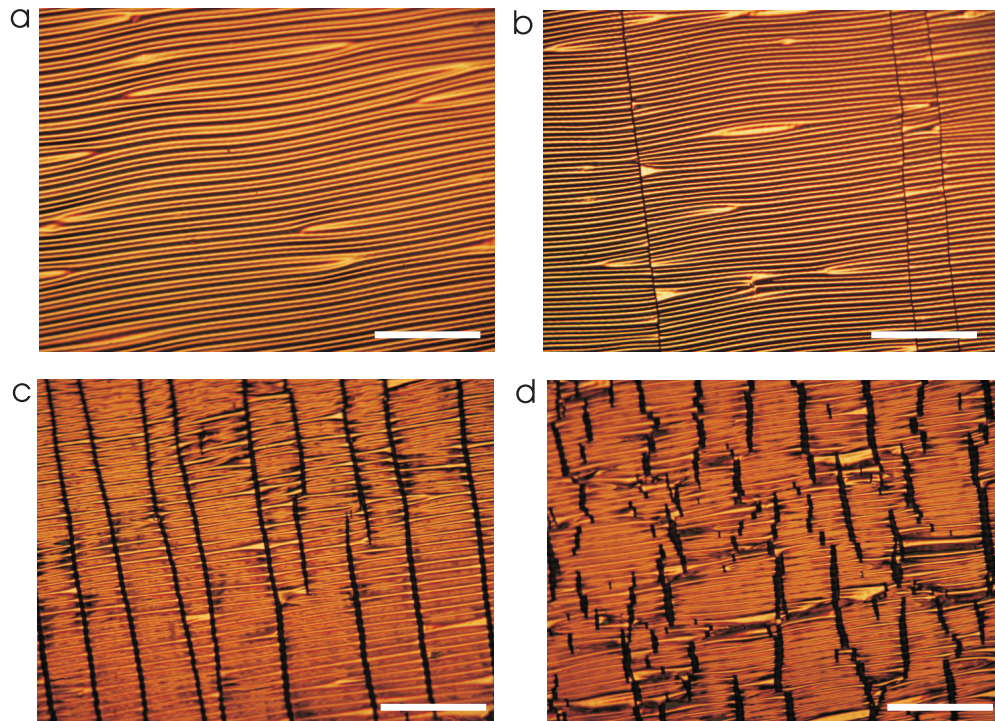


Figure 4.7: A range of images showing how the cracks in the Al layer evolve with increasing pre-strain. All of these samples have had the pre-strain applied in the vertical direction with respect to these images and have had a 219nm Al layer evaporated onto them. A $200\mu\text{m}$ scale bar is present in all images. a)5% pre-strain, no cracks are observed at this pre-strain. b)10% pre-strain, some cracking is observed although the major contribution to surface patterning comes from the wrinkling of the bilayer structure. c)30% pre-strain, the density of cracking has increased, however the major contribution to surface texture still comes from the wrinkling. d)40% pre-strain,wrinkling is still observed however the major contribution to surface texture comes from cracking of the aluminium layer.

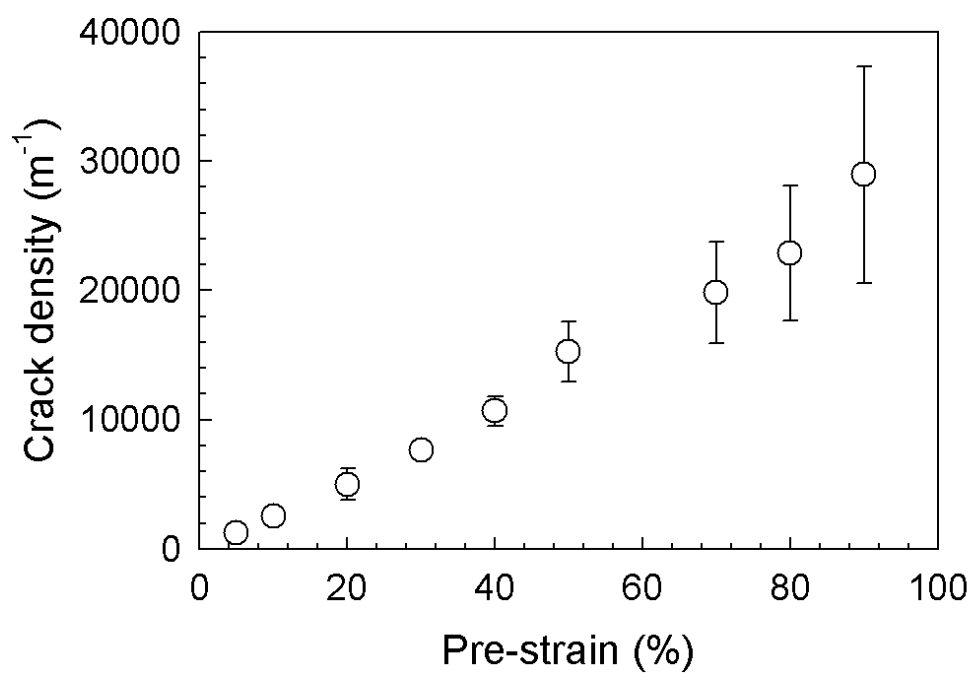


Figure 4.8: Plot showing how the density of the cracks varies with increasing pre-strain. The crack density is seen to increase linearly with increasing pre-strain.

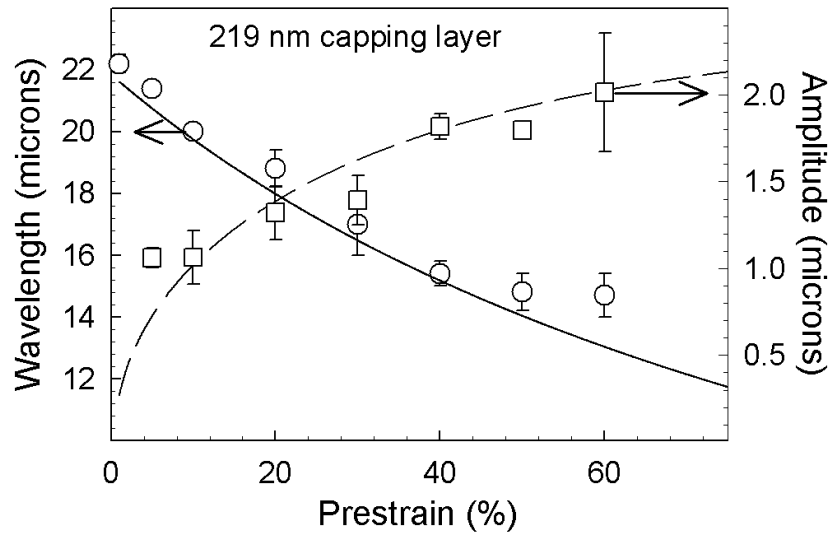


Figure 4.9: Pre-strain dependence of the wavelengths (○) and amplitudes (□) of wrinkles on elastomer samples that were capped with a 219nm thick layer of Al. Also shown are the predictions of the Song *et al.* model [9] for wavelength (solid line) and amplitude (dashed line).

As with the dependance on capping layer thickness, an excellent agreement can be seen for most of the pre-strain range shown. However there is the same discrepancy between the predicted and measured value of the wrinkle amplitude at low (< 10%) pre-strains.

References

- [1] E. Brandrup, J. and Immergut and E. Grulke, eds., *Polymer Handbook*. Wiley: New Jersey, 1999.
- [2] A. M. Howatson, P. G. Lund, and J. D. Todd, *Engineering Tables and Data*. Kluwer Academic Publishers, 1991.
- [3] K. L. Johnson, *Contact Mechanics*. Cambridge University Press, 1985.
- [4] D. Maugis, *Contact Adhesion and Rupture of Elastic Solids*. Springer, Berlin, 1934.
- [5] K. R. Shull and W. Chen, “Fracture mechanics studies of adhesion in biological systems,” *Interface Science*, vol. 8, pp. 95–100, 2000.
- [6] P. Silberzan, S. Perutz, and E. J. Kramer, “Study of the self-adhesion hysteresis of a siloxane elastomer using the jkr method,” *Langmuir*, vol. 10, pp. 2466–2470, 1994.
- [7] D. T. Read, Y. W. Cheng, R. R. Keller, and J. D. McColskey, “Tensile properties of free-standing aluminium thin films,” *Scripta Materialia*, vol. 45, pp. 583–589, 2001.
- [8] L. R. G. Treloar, *The Physics of Rubber Elasticity*. Oxford University Press, 1975.
- [9] J. Song, H. Jiang, Z. J. Liu, D. Khang, Y. Huang, J. A. Rogers, C. Lu, and C. G. Koh, “Buckling of a stiff thin film on a compliant substrate in large deformation,” *International Journal of Solids and Structures*, vol. 45, pp. 3107–3121, 2008.
- [10] A. Govindaraju, A. Chakraborty, and C. Luo, “Reinforcement of PDMS masters using SU-8 truss structures,” *Journal of Micromechanics and Microengineering*, vol. 15, pp. 1303–1309, 2005.

Gradient Wrinkled Surfaces

For the purposes of causing spontaneous droplet motion or for directing droplet motion on wrinkled surfaces, it was proposed that a gradient in the surface properties, particularly the wavelength and amplitude of the wrinkles may cause a gradient in wetting properties similar to those produced by Shastry *et al.* [1], McHale *et al.* [2], and Zhang and Han [3]. In order for there to be a gradient in wetting properties, a spatial gradient needed to exist in the total energy of the droplet. Since the surface energy per unit energy of the aluminium–water and aluminium–air interfaces would remain constant, this required a gradient in the contact area between the water and the aluminium.

This gradient in contact area required there to be a gradient in one or both of the lengthscales on the surface (wavelength and amplitude). In order to determine if this was the case, samples with a gradient in pre-strain were created, as detailed in Section 3.1.

For the purposes of understanding these gradient surfaces, one particular gradient in pre-strain was chosen. The free region of the chosen trapezoidal elastomer sample measured 2mm at its short end and 20mm at its long end. This was over approximately 16mm length. The increase in length, ΔL , was a constant 2mm over the whole sample and gave values of the pre-strain between 10% and 100%. This can be seen in Figure 5.1.

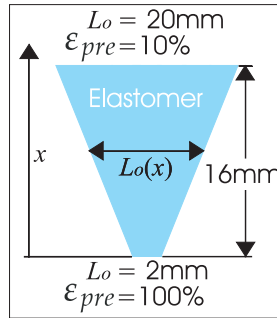


Figure 5.1: Dimensions of the trapezoidal free region of the elastomeric substrate used to create the gradient samples. All positions, x , on the sample are measured from the 100% pre-strain position. The given pre-strain values assume $\Delta L = 2mm$

It is these dimensions that were used for all of the samples discussed within this chapter. Throughout the discussion of the samples with a gradient in pre-strain, the position on the sample, x , was measured from the end of the sample with a pre-strain of 100% (see Figure 5.1).

As discussed in section 3.1.1, the local pre-strain at any given position, x , on the sample was given by $\varepsilon_{pre} = \frac{\Delta L}{L_0(x)}$. This assumes that the local pre-strain is dependent only on the local initial length and the increase in length, and has no additional components due to the non-uniformity of the sample. The predicted pre-strain profile using these assumptions can be seen in Figure 5.2.

This pre-strain profile was used to calculate all of the predicted models for comparison with the measurements for the gradient pre-strain samples.

5.1 Measuring the Gradient in Wavelength

The first property of the gradient pre-strain samples that was measured was the wavelength of the wrinkles as a function of position. In order to do this a range of locations on the sample were chosen and the positions were marked at the edge of the sample. This was to ensure that the marking process would not interfere

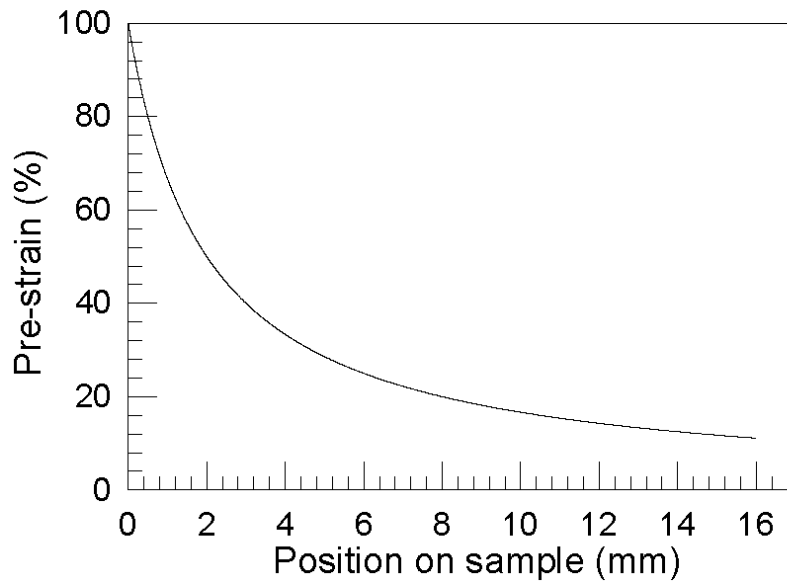


Figure 5.2: Profile of predicted the pre-strain for the chosen gradient sample.

This assumes no effects due to the non-uniformity of the sample. $\varepsilon_{pre} = \frac{\Delta L}{L_0(x)}$

with the shape of the wrinkles.

The wavelengths of the wrinkles were measured using an Olympus BX51 optical microscope. The sample was positioned under the objective such that the direction of the applied pre-strain was vertical within the image.

The Olympus BX51 optical microscope has an adjustable sample stage. This stage was able to move in two directions. The two directions are vertically, and horizontally in the images that have been taken using the microscope. This meant that when moving the sample using the adjustable stage, the direction of the applied pre-strain was aligned with one of the axes of motion of the stage. This allowed the sample to be moved along this axis without changing the position, x , that was being observed.

The microscope was then focused on the mark signifying the position to be studied. It was ensured that the mark was as close to the centre of the image as possible. The sample was then moved to a location away from the mark, but crucially a location that had the same pre-strain. An image of this location was

then taken and this image was analysed to find the wavelength of the wrinkles at this position.

Since there was a gradient across the image, the peaks within the radial average of the fast Fourier transform corresponded to the range of wavelengths within the image. However the area of the sample that was visible under the microscope was small and as such there was little difference between the width of the peak in the radial average of the fast Fourier transform of a uniform pre-strain sample and that of a gradient pre-strain sample. This can be seen in Figure 5.3.

The two radial averages shown in Figure 5.3 were chosen to have similar pre-strains such that any difference between the two would be due to the differences between the uniform and gradient samples. A fairly large value of the pre-strain (50%) was chosen for this test as the largest gradient is present at the end of the sample with the highest strain (see Figure 5.2).

The top frame of Figure 5.3 shows a sample with a uniform pre-strain of 50% with a $146nm$ thick Al capping layer. This is for comparison with the gradient sample that is shown in the bottom frame of Figure 5.3. This sample had a gradient in pre-strain and a $146nm$ thick Al capping layer. The location on the sample that was imaged was selected to have a similar local pre-strain to the uniform sample ($\approx 50\%$).

However in order to avoid any damage to the wrinkled structure prior to taking the images, the position was not measured accurately until after the measurements had been taken. Due to the large gradient in pre-strain at this position and this uncertainty in the position, the location had a higher pre-strain ($\approx 55\%$). This was found by measuring the distance from the high strain end of the gradient sample after all the measurements had been taken. This difference in pre-strain can be seen by the shift in the maximum of the radial average due to the production of wrinkles with different wavelengths.

Within the radial averages of the power spectra for the wrinkle surfaces, the

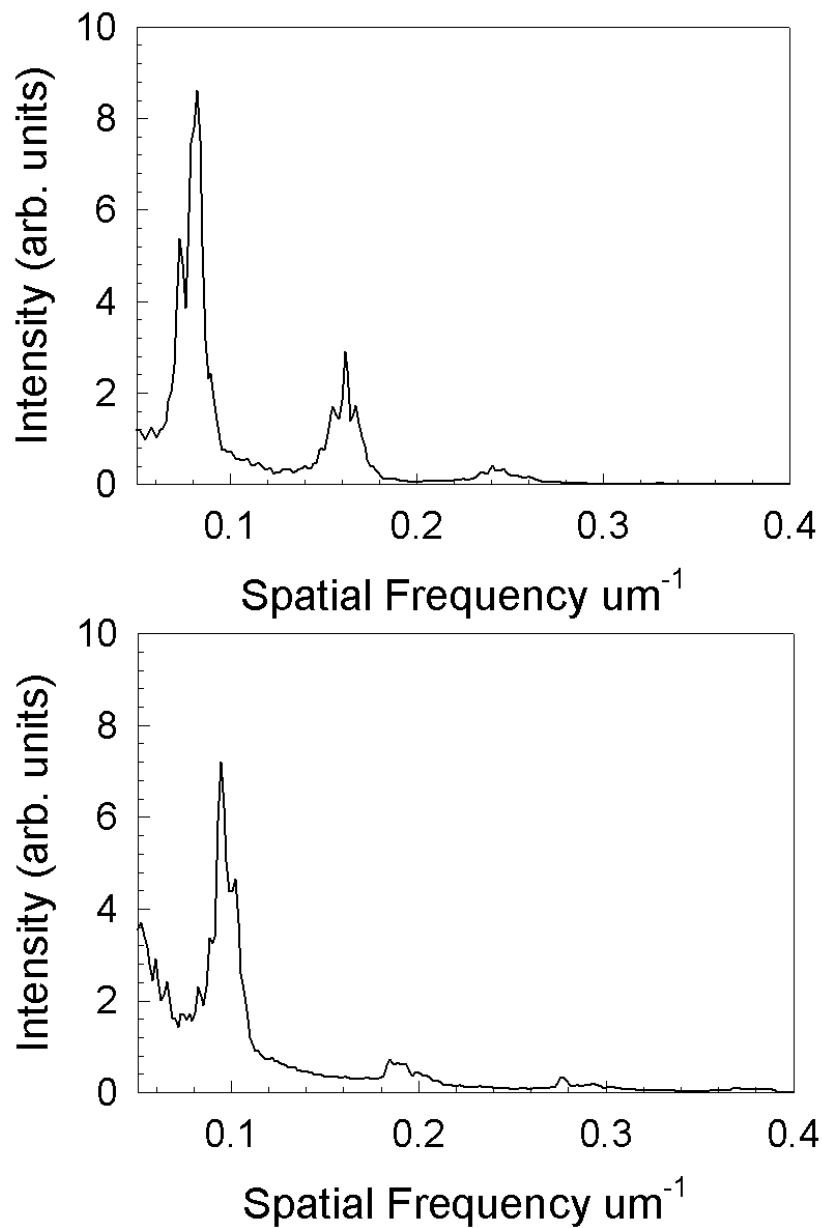


Figure 5.3: A comparison of the radial average of the fast Fourier transform of uniform and gradient samples. *Top* - Sample with a uniform pre-strain of 50% with a 146nm thick Al capping layer. *Bottom* - Sample with a gradient in pre-strain and a 146nm thick Al capping layer, the location on the sample was chosen to have a pre-strain close to 50%. When the position was accurately measured, the local pre-strain was found to be $\approx 55\%$.

width of the peak gives a measurement of the range of wavelengths that are visible within the frame of the image. A comparison of the radial averages shown in Figure 5.3 shows that there is little difference in the width of the peaks within the radial average between the gradient pre-strain sample and the uniform pre-strain sample. As such it was assumed that the gradient in wavelength was small enough that it would not need to be considered when measuring the wavelength as a function of position, and that the average wavelength within an image gave a good approximation of the wavelength of the wrinkles at the centre of the image.

This technique was used at various positions on the sample to measure how the wavelength changed with position. An example of this can be seen in Figure 5.4. Figure 5.5 shows the measured wavelengths as a function of position along with the prediction given by the model proposed by Song *et al.* [4].

Figure 5.5 shows that there is good agreement at all but the highest values of pre-strain (low value for position). There are two possible explanations for this; firstly this is the region of the sample under the highest strain, and therefore also the region under the highest stress. If the elastomeric substrate were to detach from the stretching rig, either before or after the elastomer ‘glue’ had fully cured, this would be the region most likely to have undergone detachment. This is not believed to be the case as any detachment following the curing of the elastomer ‘glue’ would have been apparent after removal from the thermal evaporation unit since the shape of the strained elastomer would have changed. Any detachment prior to the curing of elastomer (due to the pre-strain being applied before the ‘glue’ was fully cured) would become apparent following the release of the pre-strain since the ‘glue’ would continue to cure following the application of the pre-strain causing slipping between the holder and the sample. This would create excess elastomer between the two sides of the holder, and this would buckle upon the release of the pre-strain. Neither of these two effects were apparent on any of the samples; as such this is not believed to be the reason for the discrepancy.

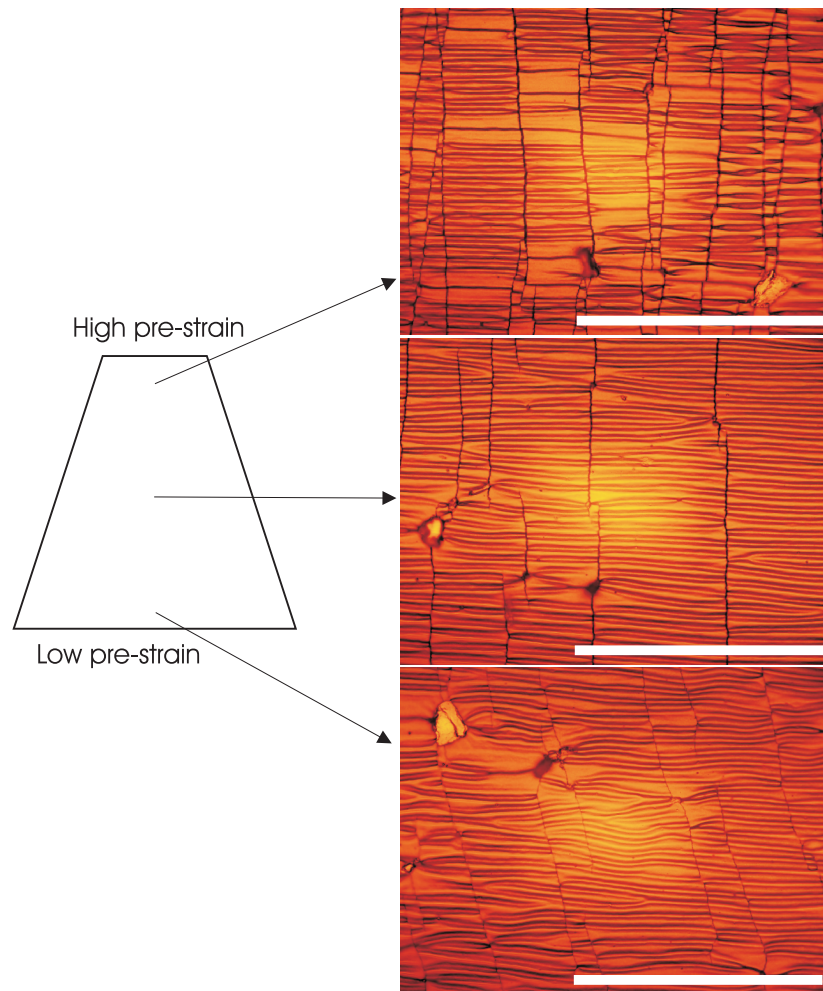


Figure 5.4: Example images of a gradient sample taken from a range of positions. The scale bar on each image is $200\mu m$ long. The diagram on the left shows the approximate location from which each image was taken. The wavelength of the wrinkles can clearly be seen to increase with decreasing pre-strain,

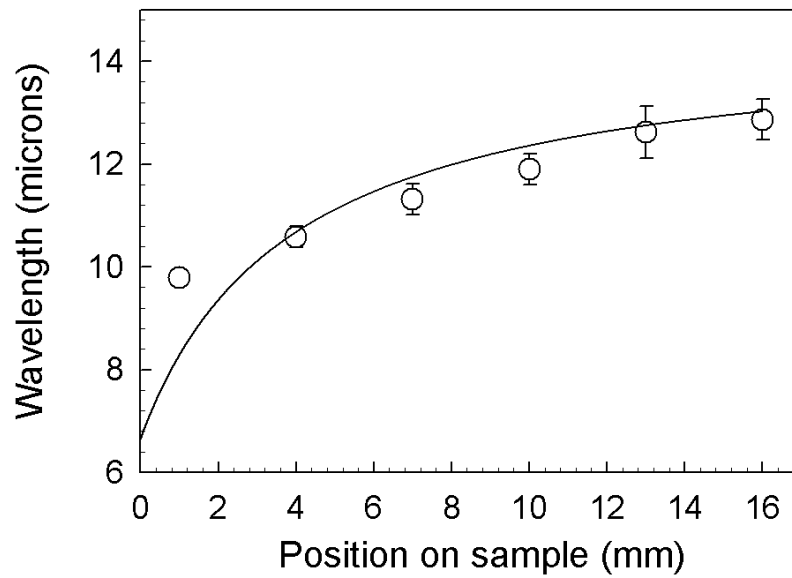


Figure 5.5: A plot showing the wavelength of the wrinkles as a function of the position on a sample with a gradient in pre-strain and a 146nm thick Al capping layer. Also shown as a solid line is the prediction from the model by Song *et al.* [4]. The pre-strain value for each position was taken from Figure 5.2 to calculate the the predicted wavelength.

The second possibility for this difference is that the model proposed by Song *et al.* [4] only accounts for samples with a uniform pre-strain. In order to generate the predictions shown in Figure 5.5 it was assumed that the sample would act as a series of unconnected uniformly strained samples with different values of pre-strain. This does not take into account any additional components of strain within the elastomer as a result of the gradient in pre-strain. The discrepancy between the results and the model only occurs at high values of pre-strain. This was also the region of the sample with the highest gradient in pre-strain. As such, any effects due to the gradient in pre-strain would be most apparent within this region. This may explain the observed discrepancy between the results and the model.

5.2 Measuring the Amplitude of Wrinkles on the Gradient Samples

Once the wavelength was known as a function of the position, the next property to consider was the amplitude of the wrinkles as a function of position. The wrinkles were imaged using an Asylum Research MFP-3D scanning force microscope operating in intermittent contact mode. The peak-to-peak amplitude was measured from these images and halved to find the amplitude of the wrinkles (see section 3.3 for more details).

The amplitude of the wrinkles was measured at the same location as the wrinkle wavelength was measured. In order to do this, the sample was mounted on the translation stage of the scanning force microscope such that the direction of the applied pre-strain was aligned with one of the axes of motion of the translation stage. The optical system built into the scanning force microscope was then focused on the same marks at the edge of the sample that had been used when measuring the wavelengths. Once the centre of this mark was below the end of the

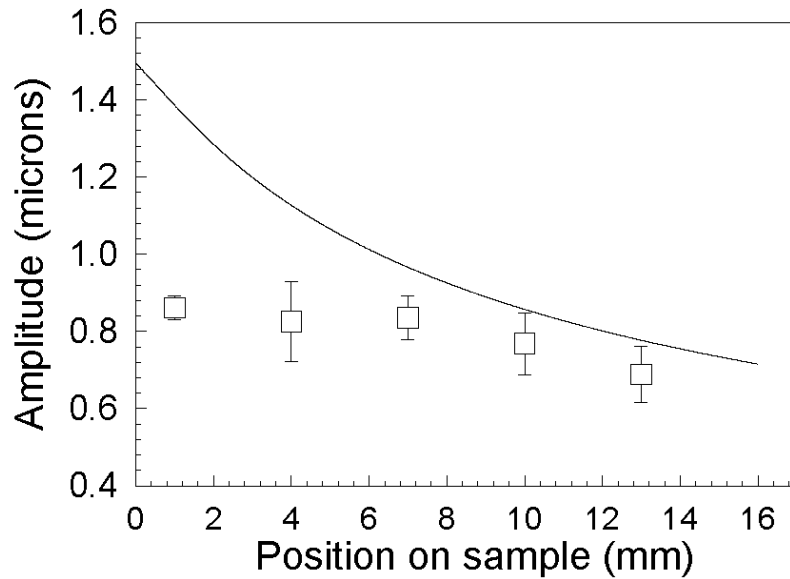


Figure 5.6: A plot showing the amplitude of the wrinkles as a function of the position on a sample with a gradient in pre-strain and a 146nm thick Al capping layer. Also shown as a solid line is the prediction from the Song *et al.* model [4]. The pre-strain value for each position was taken from Figure 5.2 to calculate the the predicted wavelength.

cantilever in the scanning force microscope, the sample was moved in a direction parallel to the direction of the applied pre-strain, such that the pre-strain beneath the end of the cantilever remained constant.

Once a suitable location to image the surface had been chosen, a region of the surface of size $60\mu\text{m}$ by $60\mu\text{m}$ was imaged. This corresponds to an area close to the centre of the optical microscope images used to measure the wavelengths. The amplitude of the wrinkles was then measured at several locations within the scanning force microscope image. This process was repeated at several locations along the line of constant pre-strain.

The measured amplitude of the wrinkles as a function of position is shown in Figure 5.6. Also shown are the values predicted using the Song *et al.* model [4].

Figure 5.6 clearly shows that there was only a small change in the amplitude

of the wrinkles across the sample, and that this change is much smaller than that predicted by the Song *et al.* model [4]. This discrepancy is the most prominent at the end of the sample with a high pre-strain and a high gradient in pre-strain. This area of the sample was therefore the most likely to experience any effects due to the strain gradient, for example the introduction of shear forces within the elastomer, that alter the wavelength and amplitude of the resultant bilayer.

5.3 Area of the Wrinkled Structure

In order for the samples to have a gradient in wetting properties, they needed to have a gradient in the contact area between the aluminium surface and the water droplet on the surface, as discussed in Section 2.4. The contact area will be dependent on both the amplitude and the wavelength of the wrinkles. A measurement of how the contact area varied per unit area of the sample, the area ratio, was defined to determine how the contact area varied with position. The area ratio was defined as the ratio of the surface area of the wrinkled surface to the projected area:

$$AreaRatio = \frac{L_{surface}W}{L_0W} = \frac{L_{surface}}{L_0} \quad (5.3.1)$$

where W is the width of the sample at this position, $L_{surface}$ and L_0 are defined to be the length of the unwrinkled surface, and the length of the wrinkled surface respectively. $L_{surface}$ and L_0 are shown in Figure 5.7.

In order to determine how the area ratio changes as a function of position, $L_{surface}$ needed to be calculated. This was done by assuming the wrinkles had a sinusoidal profile with the measured wavelength and amplitude, $z = A \sin\left(\frac{2\pi x}{\lambda}\right)$.

The length of a curve is defined as:

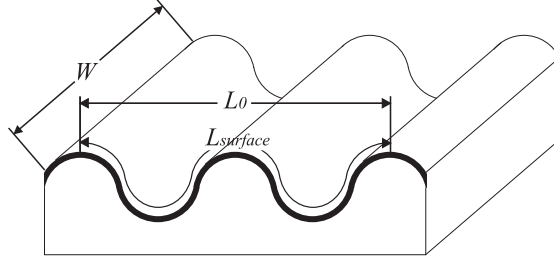


Figure 5.7: Definition of the terms used in equation 5.3.1. $L_{surface}W$ is the surface area of the wrinkled surfaces. L_0W is the projected area of the surface. In both cases W is the width of the sample.

$$r = \int_0^L \left(1 + \left(\frac{dz}{dx} \right)^2 \right)^{\frac{1}{2}} dx$$

Since, in the case of these wrinkles, $z = A \sin \left(\frac{2\pi x}{\lambda} \right)$, $L_{surface}$ can be defined as

$$L_{surface} = \int_{x=0}^{x=L_0} \left(1 + \left(\frac{2\pi A}{\lambda} \right)^2 \cos^2 \left(\frac{2\pi x}{\lambda} \right) \right)^{\frac{1}{2}} dx$$

which gives the area ratio (using equation 5.3.1) to be

$$AreaRatio = \frac{\int_{x=0}^{x=L_0} \left(1 + \left(\frac{2\pi A}{\lambda} \right)^2 \cos^2 \left(\frac{2\pi x}{\lambda} \right) \right)^{\frac{1}{2}} dx}{L_0} \quad (5.3.2)$$

Using equation 5.3.2 the area ratio was numerically calculated for each of the positions on the gradient sample. The numerically calculated values of the area ratio can be seen in Figure 5.8.

Figure 5.8 shows a very clear gradient in area ratio with respect to position on the gradient sample. Although the measured results for the gradient samples are not in excellent agreement with the Song *et al.* model [4], a gradient in the area ratio was still present when using this method to create a gradient in the wavelength and amplitude of the wrinkles present on the surface of the bilayer structure.

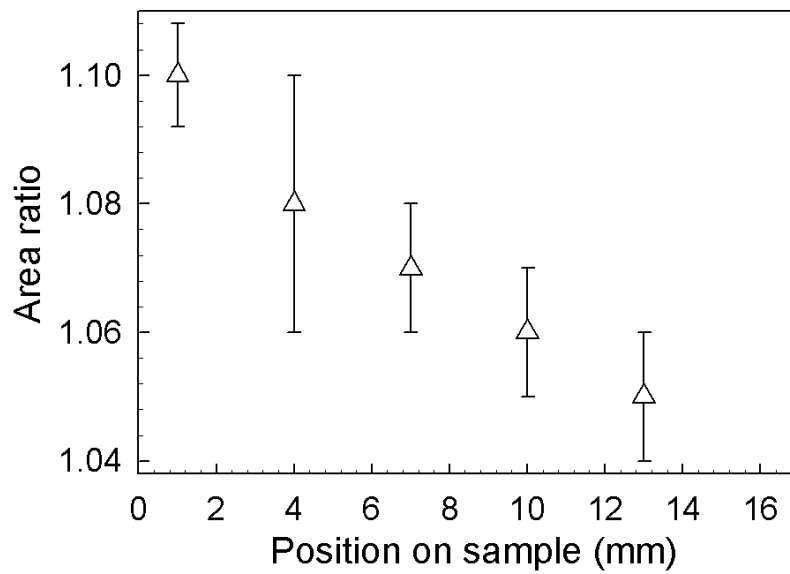


Figure 5.8: The area ratio, as calculated numerically using equation 5.3.2 along with the measured values for wavelength and amplitude as shown in Figures 5.5 and 5.6 respectively, as a function of the position on the sample. A gradient in the area ratio can be clearly seen across the sample.

It was this gradient in area ratio that was proposed to be a possible source for a gradient in contact area between the aluminium and the water droplet. Assuming this was the case there would be a gradient in the wetting properties of these wrinkled surfaces. It was this gradient that was proposed as a possible source for directed or spontaneous droplet motion on these surfaces.

References

- [1] A. Shastry, M. J. Case, and K. F. Böhringer, “Directing droplets using microstructured surfaces,” *Langmuir*, vol. 22, pp. 6161–6167, 2006.
- [2] G. McHale, N. J. Shirtcliffe, S. Aqil, C. C. Perry, and M. I. Newton, “Topography driven spreading,” *Phys. Rev. Lett.*, vol. 93, no. 3, pp. 6102–6105, 2004.
- [3] J. Zhang and Y. Han, “A topography/chemical composition gradient polystyrene surface: Toward the investigation of the relationship between surface wettability and surface structure and chemical composition,” *Langmuir*, vol. 24, pp. 796–801, 2008.
- [4] J. Song, H. Jiang, Z. J. Liu, D. Khang, Y. Huang, J. A. Rogers, C. Lu, and C. G. Koh, “Buckling of a stiff thin film on a compliant substrate in large deformation,” *International Journal of Solids and Structures*, vol. 45, pp. 3107–3121, 2008.

Wetting Properties of Wrinkled Surfaces

A variety of authors have looked at methods of creating surfaces with controllable wetting properties [1–6]. Yu *et al.* [5] in particular have shown that from a single surface it can be possible to get a very large range of wetting properties. After adsorption of $\text{HS}(\text{CH}_2)_{10}\text{CH}_2\text{OH}$ on a gold surface they were able to achieve contact angles ranging from less than 10° up to over 150° by simply changing the amount of time that the gold was submerged in a dilute solution of $\text{HS}(\text{CH}_2)_{10}\text{CH}_2\text{OH}$. Instead of looking at changing the chemical composition of the surface, this chapter will instead consider the range of contact angles that can be produced by changing the wavelength and amplitude of the wrinkles on aluminium–elastomer bilayer surfaces.

In order to determine the wettability gradient on the gradient pre-strain samples, the contact angle of a sessile water droplet was measured. This was initially done on the samples with a uniform pre-strain that corresponded to a range of positions on the gradient sample.

This was done so that the equivalent position on the gradient sample (the position with the same pre-strain as the uniform sample) was well known and so that the contact angles on opposite sides of the droplet were the same.

The important contact angles in this case are those seen when the droplet is viewed with the direction of the applied strain perpendicular to the plane of the image. When viewed from this position, any movement caused or directed by the gradient would be in the plane of the image and this would mean that the advancing and receding contact angles would be visible in this direction. Since it is possible for the droplet to have different contact angles when viewed from different angle due to the alignment of the wrinkles on the surface, this is also the direction from which the uniform samples were viewed.

Once images of the sessile water droplets had been taken, the contact angle between the liquid-solid interface and the liquid-air interface could be measured. These contact angles are shown in Figure 6.1.

The results shown in Figure 6.1 are from a single run of experiments. One of the droplets (circled) exhibits a contact angle that is much larger than the rest of the data suggests that it should. This was seen in repeats of the experiment, however it was seen to happen at all pre-strains and so was not believed to be a feature of the surface for any particular pre-strain. For this reason it was proposed that the sessile water droplet may have landed on the surface and found a metastable position to occupy. Since this position would be dependent upon how and where the droplet landed on the surface, it would be very difficult to control and as such very difficult to get any consistent measurements.

In order to solve the problem of the droplets being in a metastable position, the Al capped elastomer being used as the substrate, was oscillated close to a harmonic of the resonant frequency of the sessile water droplet. The resonant frequency was estimated by stepping through a range of frequencies, first crudely, and then more finely, watching the droplet on the microscope to estimate the frequency at which it exhibited the largest vibration. This oscillation was applied normal to the surface of the bi-layer, and would cause the contact area of the droplet to expand and contract, allowing the droplet to sample nearby conformations. This caused the

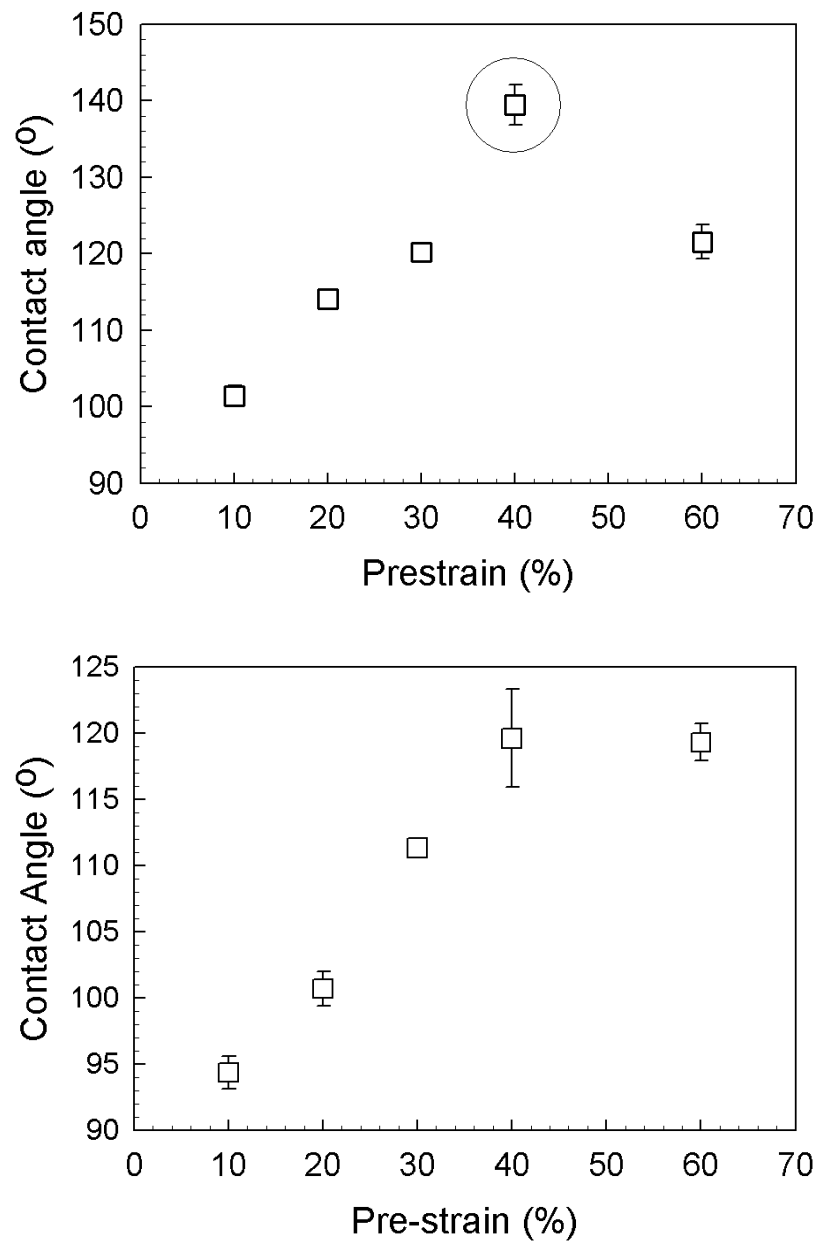


Figure 6.1: The measured contact angle of sessile water droplets on wrinkled elastomer-Al bilayers with a range of pre-strains. *Top* The measurements were taken immediately after the water droplet had landed on the surface. *Bottom* These results followed a 1 second oscillation of the bilayer, at a harmonic of the resonant frequency of the sessile water droplet. The capping layer thickness used for these experiments was 146nm

droplet to find positions with a lower total energy than the position in which it initially landed and hopefully it would find the lowest energy configuration on the surface and hence the equilibrium contact angle. With all of the measurements done with sessile water droplets in the ground state, the measurements were much more consistent. The results of this can be seen in Figure 6.1. The contact angle of the droplet on these surfaces displays a similar pattern to that discovered by Chung *et al.* [7].

Figure 6.1 shows that the contact angle increases monotonically with increasing strain (within error) for sessile water droplets that have been oscillated at their resonant frequency. When the equivalent positions on the gradient sample (those positions that have the same pre-strain) are considered (see Figure 6.2), a gradient in the contact angle can be clearly seen. Since the contact angle of a droplet on the surface is related to the wettability of that surface, these measurements suggested that a wetting gradient may be present on gradient surfaces.

Since the measurements done on uniform samples suggested that a wetting gradient should be present on the gradient pre-strain samples, there was a spatial gradient in the total energy of the droplet. This means that there is a force present that may be able to direct the motion of sessile water droplets on these surfaces. Before this was tested, it was necessary to check what wetting gradient (if any) was present on the gradient surfaces themselves.

In order to measure the contact angle as a function of position on the gradient samples, the position of the droplet on the sample needed to be accurately known. However it was difficult to control the location that the water droplet landed on the surface. As such it was necessary to measure the position of the droplet after it had been deposited on the surface.

In the images that were taken to measure the contact angle, the entire bilayer sample could be seen. since the bilayer was known to be the same distance from the camera as the droplet, it was used as a reference for the position of the droplet.

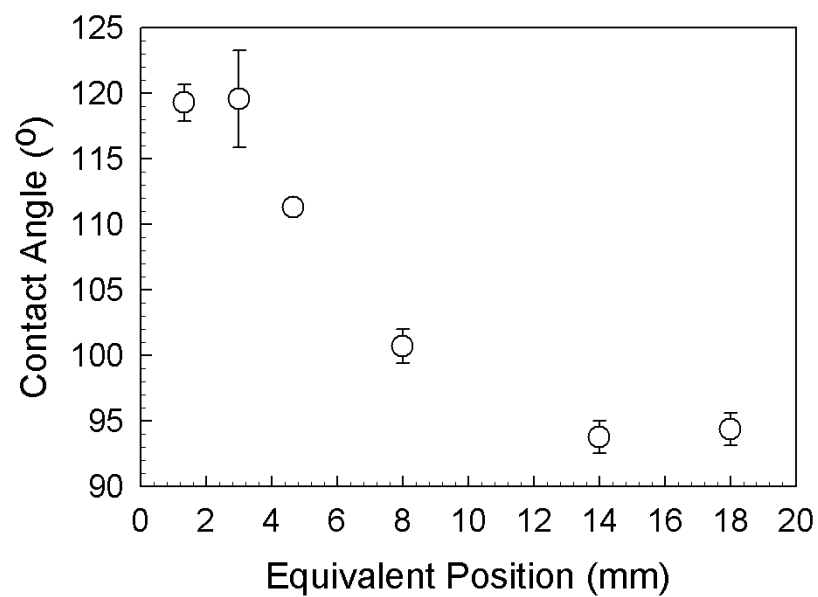


Figure 6.2: The estimated wetting profile of sessile water droplets on the gradient pre-strain samples. The contact angles are measured on uniform pre-strain samples with the same pre-strain as the equivalent position on the gradient sample.

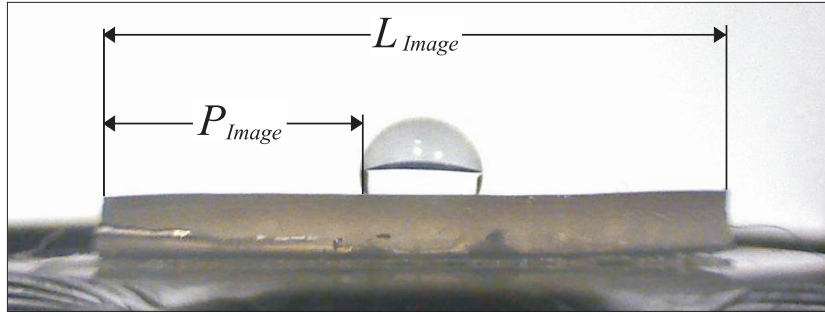


Figure 6.3: Definition of the values P_{Image} and L_{Image} used to measure the position of the droplet on the surface. These are both measured in pixels, however the length of the bilayer is also separately measured in mm to provide an accurate measurement for the position of the droplet on the surface using equation 6.0.1.

The position was calculated by taking the ratio of the distance from the end of the sample to the sessile water droplet, and the length of the bilayer sample (in the image), and multiplying this by the size of the bilayer sample the position of the droplet on the sample could be accurately calculated as

$$Position = \frac{P_{Image}}{L_{Image}} \times Length \quad (6.0.1)$$

where the lengths P_{Image} and L_{Image} are the distance between the droplet and the end of the bilayer, and the length of the bilayer respectively, as measured in the image and $Length$ is the measured length of the bilayer sample. Both P_{Image} and L_{Image} were measured in pixels and are shown in Figure 6.3.

This method was used to find the position of both the left and right contact angles. These were measured separately (unlike with the uniform pre-strain samples) since there was a difference in contact angle due to the gradient in the contact area of the droplet. This difference in contact angle can be seen in Figure 6.4 which shows an $8\mu l$ sessile water droplet on a gradient pre-strain sample. The droplet is close to the high pre-strain end of the sample and has a local pre-strain of $\approx 90\%$. The contact angle on either side of the droplet is displayed on the

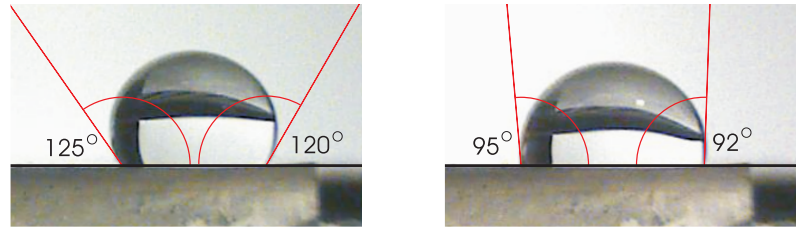


Figure 6.4: An $8\mu\text{l}$ sessile water droplet on a gradient pre-strain sample with a 146nm capping layer with pre-strain going from 10% at the low strain end to 100% at the high strain end ($\approx 90\%$ pre-strain at the displayed position). Images from before (*left*) and after (*right*) the oscillation of the bilayer are shown. The contact angle on each side of the droplet is shown in both cases with an error of $\pm 1^\circ$. A change in contact angle can be seen in both cases, with a change of $\approx 3^\circ$ for the post vibration droplet.

image and a change in contact angle of $\approx 3^\circ$ can be seen. The position of the contact angle for each side of the droplet was measured separately for the images from before and after the vibration of the bilayer.

This was done for a variety of positions on the gradient surfaces and a map of the contact angle with position was created. This can be seen in Figure 6.5.

The data taken from the gradient sample has much more variation than the data from the uniform samples. This is to be expected. When measuring the contact angles on the uniform pre-strain samples, multiple experiments were carried out and the mean was taken. However for the gradient samples it was not possible to repeat experiments at the same position as it was extremely difficult to control the position of the drop on the surface with the level of accuracy that would be required for that. As such each data point corresponds to a single experiment rather than a group of experiments. This means that there was more variation between nearby measurements than for the uniform pre-strain samples as any non-systematic errors were not eliminated by repeating the experiments.

Although not as clear as for the uniform pre-strain samples, a change in the

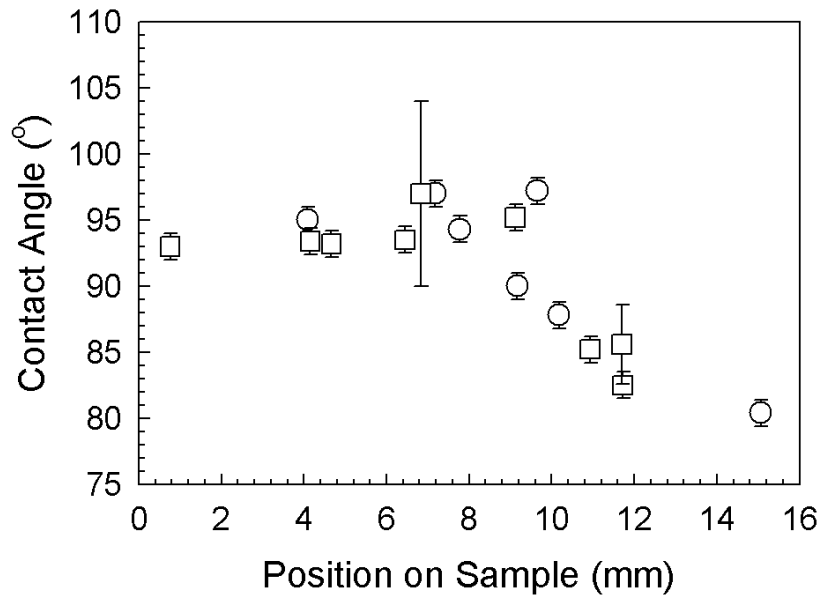


Figure 6.5: Graph showing individual measurements of the contact angle seen as a function of the droplets position on the gradient sample. Both sides of the droplet were measured individually. The contact angle closest to the low pre-strain end of the sample (○) and the contact angle closest to the high pre-strain end of the sample (□) are both shown. Although at large pre-strains (small position) the contact angle does not change much, a change in the contact angle can be clearly seen for low pre-strain.

contact angle with respect to position can still be seen in Figure 6.5 for the droplets on the gradient pre-strain samples.

References

- [1] S. Daniel, S. Sircar, J. Gliem, and M. K. Chaudhury, “Ratcheting motion of liquid drops on gradient surfaces,” *Langmuir*, vol. 20, pp. 4085–4092, 2004.
- [2] S. Daniel, M. K. Chaudhury, and J. C. Chen, “Fast drop movements resulting from the phase change on a gradient surface,” *Science*, vol. 291, p. 633, 2001.
- [3] Y. Ito, M. Heydari, A. Hashimoto, T. Konno, A. Hirasawa, S. Hori, K. Kurita, and A. Nakajima, “The movement of a water droplet on a gradient surface prepared by photodegradation,” *Langmuir*, vol. 23, pp. 1845–1850, 2007.
- [4] L. Qiang, W. Hong, Z. Xun, and L. Mingwei, “Liquid droplet movement on horizontal surface with gradient surface energy,” *Science in China Series E: Technological Sciences*, vol. 49, pp. 733–741, 2006.
- [5] X. Yu, Z. Wang, Y. Jiang, and X. Zhang, “Surface gradient material: From superhydrophobicity to superhydrophilicity,” *Langmuir*, vol. 22, pp. 4483–4486, 2006.
- [6] C. G. Gölander, K. Caldwell, and Y. S. Lina, “A new technique to prepare gradient surfaces using density gradient solutions,” *Colloids and Surfaces*, vol. 42, pp. 165–172, 1989.
- [7] J. Y. Chung, J. P. Youngblood, and C. M. Stafford, “Anisotropic wetting on tunable micro-wrinkled surfaces,” *Soft Matter*, vol. 3, pp. 1163–1169, 2007.

Droplet Motion

Once it was known that there was a gradient in the wetting properties, it was proposed that this could be used to direct or possibly drive droplet motion. During the measurements of the droplet contact angle on the gradient surfaces, no motion of the droplet was observed. It was not clear at that stage whether there was no motion at all or if the motion was too slow to observe during the contact angle measurements. During the contact angle measurements, the camera was only focused on the droplet for around 10 – 15 seconds. In order to determine whether any spontaneous movement would happen within time-scales smaller than the time taken for the water droplet to evaporate, a droplet was placed on the gradient surface under the optical microscope. The microscope was setup to take images once every thirty seconds for approximately ninety minutes.

A selection of images taken during this experiment are shown in Figure 7.1.

Figure 7.1 shows that the time-scale for the evaporation of the droplet is approximately 75 minutes. Within this time-scale, the droplet did not move by a detectable amount. The droplet fully evaporated before any movement could be seen. This meant that the gradient in wettability on these samples was not large enough to cause detectable spontaneous droplet motion within the time required for the droplet to evaporate.

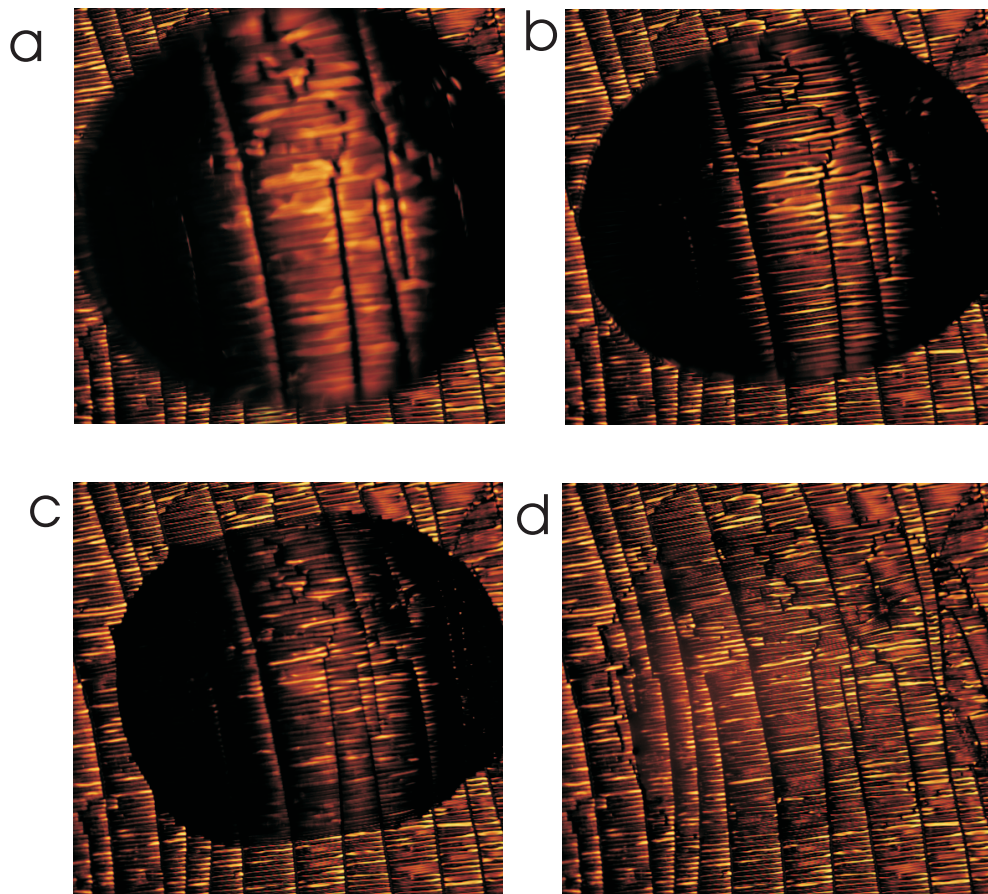


Figure 7.1: Images of a sessile water droplet on a gradient pre-strain surface viewed from above. These images were part of an experiment to determine whether the evaporation time-scale was longer or shorter than the time-scale for measurable movement. These three images were taken at times of a) 0 minutes, b) 30 minutes, c) 60 minutes and d) 75 minutes. The droplet can be seen to be shrinking due to evaporation and after 1 hour and 15 minutes the droplet has fully evaporated. However the droplet does not exhibit any detectable motion.

Other studies [1–4] have shown that in some cases it is necessary to excite the water droplet by vibrating the substrate in order to allow it to sample nearby conformations. For this reason it was decided that the sample should be mounted on a speaker such that a vibration could be applied to the bilayer that would cause the droplet to sample nearby locations on the surface and move to those with a lower total energy.

In order to estimate the activation energy of this motion, the variation in the energy of the droplet was considered as the leading edge of the droplet moved from one peak of the pattern on the surface to an adjacent peak. Throughout this movement, the trailing edge of the droplet also moves from one peak to an adjacent peak. Consequently the area of contact between the surface and the droplet will remain approximately constant during this movement.

The front and rear of the droplet will experience the greatest change in surface area while the side of the droplet will experience very little change. The maximum increase in the circumference of the droplet will be along the line from the front of the droplet to the rear and will be:

$$\Delta l = \Delta l_{front} + \Delta l_{rear} = 2A + 2A = 4A \quad (7.0.1)$$

where A is the amplitude of the wrinkles. The increase in the length of this line will vary approximately as the cosine of the angle between a given cross-section and the front-rear line already considered. This gives the change in area of the water-air interface as:

$$\Delta Area = 4A \int_{\frac{\pi}{2}}^{\frac{\pi}{2}} r \cos \theta d\theta = 8Ar \quad (7.0.2)$$

where r is the radius of the contact area between the water and the surface. This gives an increase in the energy of:

$$\Delta E = 8Ar\gamma \quad (7.0.3)$$

where γ is the surface tension of water. This gives an activation energy for droplet motion of approximately $2.3 \times 10^{10} J$ or $1.4 \times 10^9 eV$, much higher than the energy provided by thermal energy (approximately $28 meV$). This means that an oscillation will be needed to move the droplet. The maximum energy per cycle of an oscillation transferred to the droplet is:

$$E_{cycle} = \frac{1}{4}m\omega A^2 \quad (7.0.4)$$

where m is the mass of the droplet, A is the amplitude of the oscillation and ω is the angular frequency of the oscillation. However this value will only be converted to a motion of the droplet close to the resonance of the droplet when the leading edge of the droplet moves by more than half the wavelength of the surface wrinkles, such that it is energetically favourable for the droplet to move to a new position.

7.1 Moving a Droplet with White Noise

As the resonant frequency of the droplet was not known, the sample was initially subjected to a signal of broadband noise or ‘white noise’. This consisted of frequencies in the range of $0 - 512 Hz$ with the difference between two adjacent frequencies being $0.125 Hz$. Ideally each of the frequencies within the signal would have had the same amplitude such that, regardless of the resonant frequency of the droplet, the oscillation amplitude would always be the same.

The first attempt to achieve this was an 8 second long signal with a sample rate of $1024 Hz$. Each sample within this signal had a randomly generated value between $-1V$ and $+1V$. In order to confirm that this gave a signal with a range

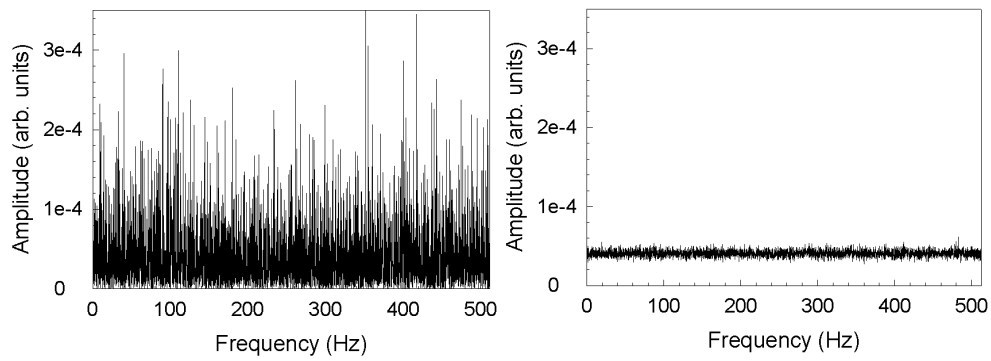


Figure 7.2: *Left*, example power spectrum from a single run of the experiment. There is clearly a large difference in amplitude between different frequencies. *Right*, average power spectrum from 100 experimental runs. This shows that on average each frequency will have the same amplitude over multiple runs.

of frequencies, and that each had the same amplitude, the Fourier transform of the signal was considered. An example of this is shown in the left frame of Figure 7.2.

Figure 7.2 shows that in a single run (left frame) the amplitude of a given frequency is not precisely known. This means that the amplitude of the applied oscillation at the resonant frequency of the droplet was not known. However as can be seen in the right hand frame of Figure 7.2, the average power spectrum over multiple runs is close to flat. Therefore the average amplitude of the resonant frequency of the droplet over multiple experiments was known.

This experiment was therefore able to give an indication of the suitability of the gradient samples for directing the motion of sessile water drops.

The location of the water droplet was tracked throughout the vibration, until too much of the droplet had left the visible area, when using the Olympus BX51 optical microscope, to accurately identify the centre of the droplet. Figure 7.3 shows an example run of a droplet on a sample being vibrated by a ‘white noise’ signal. After an initial fast motion with a speed of $3.0 \pm 0.2 \mu\text{ms}^{-1}$ lasting approximately 30 seconds, the droplet slows to approximately $0.32 \mu\text{ms}^{-1}$. This speed is

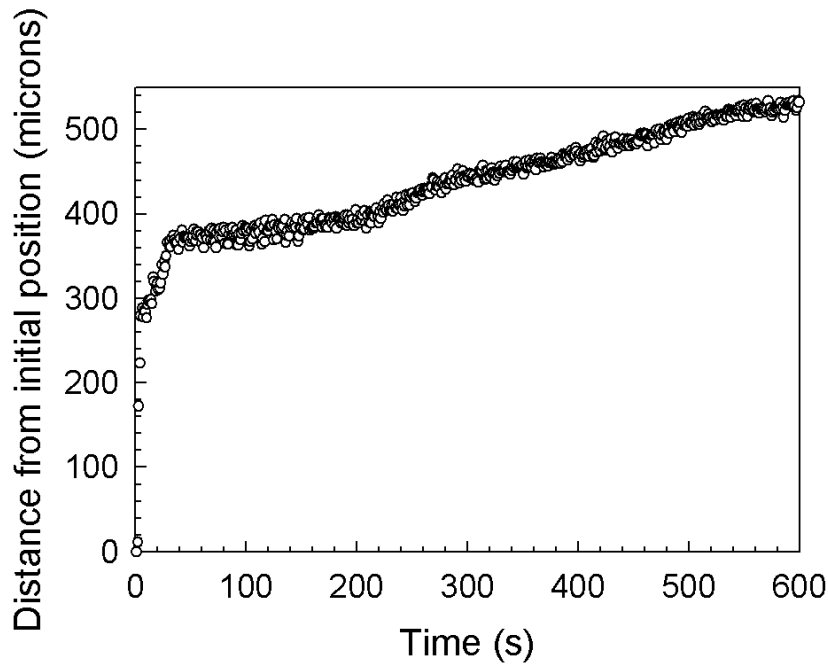


Figure 7.3: Plot showing the measured position of a sessile water droplet during application of a vibration consisting of white noise. The distance that the centre of the droplet had moved since the vibration was turned on is plotted against the duration of the vibration. An initial fast movement is seen for approximately 30 seconds before a slower speed becomes evident for the rest of the droplets motion.

consistent with that seen in additional repeats of the experiment, where speeds of $0.30 - 0.35 \mu\text{ms}^{-1}$ were observed.

Throughout these experiments, the water droplet consistently moved from the high pre-strain end of the sample and towards the low pre-strain end (see Figure 7.4). This indicated that the direction of the motion may be due to the gradient in wettability. In order to ensure this was the case, similar tests were carried out on a range of samples. These were:

- Flat elastomer samples
- Flat evaporated aluminium samples (evaporated onto single crystal silicon wafers (Compart Technology, UK))

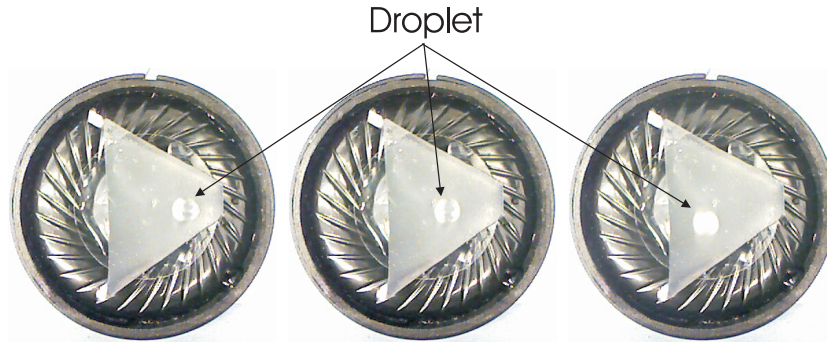


Figure 7.4: Images showing the motion of the droplet on the sample. The sample is mounted on the speaker with the high pre-strain end to the right of each image and the low pre-strain end to the left. The images are in order from left to right and were taken at intervals of 10 minutes. The droplet can be seen to move from the high pre-strain end of the sample towards the low pre-strain end.

- Uniform pre-strain bilayer samples

None of these three types of samples showed any evidence that the surface was directing the motion of the droplet. Any movement that was seen appeared to be in a random direction and was not reproducible. Often however, there was no movement present during the experiments. This can be seen in Figure 7.5.

Figure 7.5 demonstrates that neither the aluminium or the elastomer alone can direct droplet motion, and in the case of the aluminium there was no movement at all detected during the experiments. For the water droplet on the elastomer substrate, some motion was observed at short time-scales, however this was not in any particular direction and is assumed to be motion towards a defect on the surface of the elastomer. This rules out a systematic error, such as the sample stage not being level, causing motion in the preferred direction. Also since this motion was over a very short distance ($< 300\mu m$), this motion is assumed to be related to a defect upon the surface of the elastomer due to the short distance moved and the rapid change in speed after this motion.

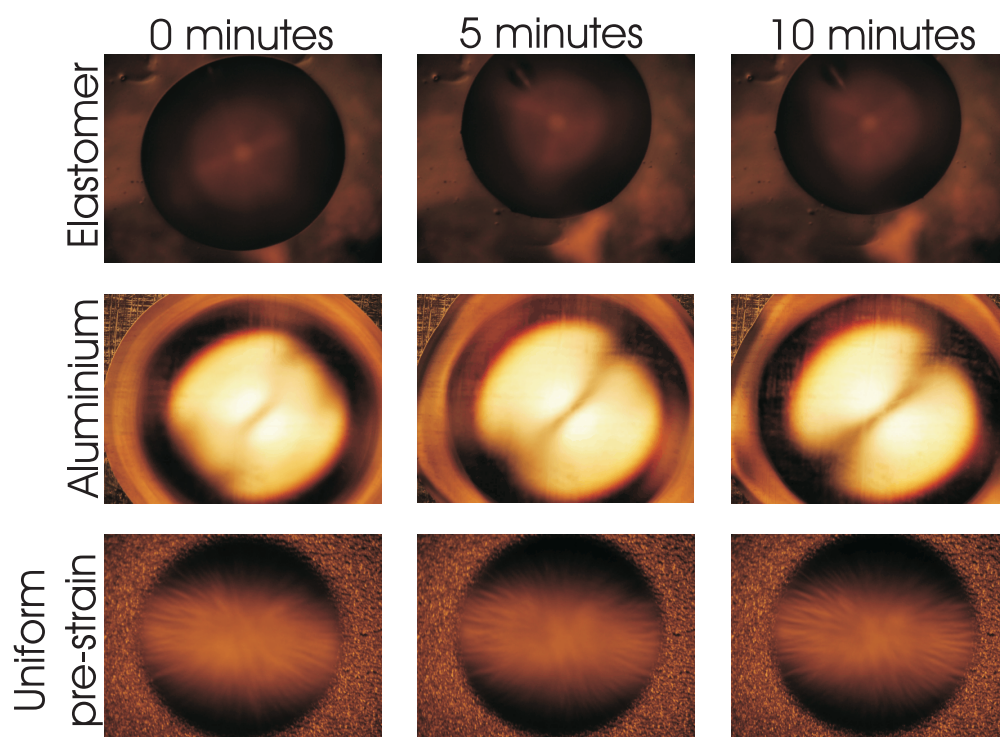


Figure 7.5: Images showing the lack of motion seen when vibrating droplets on (*top*) flat elastomer samples, (*middle*) flat aluminium evaporated onto a silicon substrate and (*bottom*) uniform pre-strain samples. In all three cases the images were taken from left to right at times of 0 minutes, 5minutes and 10 minutes after the start of the vibration respectively.

Additionally the bottom frames in Figure 7.5 show the motion of a sessile water droplet placed upon a sample with a uniform pre-strain. Again, in this case no motion was observed which leads to the conclusion that any motion present in the gradient pre-strain samples comes from the differences between the surfaces of the uniform and gradient pre-strain samples. The only difference between them being the gradient in the amplitude and wavelength of the wrinkles leading to the gradient in contact area.

This series of experiments has therefore indicated that the directed motion of sessile water droplets on these gradient pre-strain samples is a direct consequence of the gradient in contact area of the droplet and the wrinkled bilayer sample. Additionally it was also shown that the speed of the droplet was not adversely affected by the unknown amplitude of the oscillation at the resonant frequency of the droplet. This was most likely due to the nearby frequencies also having a strong effect on the speed of the droplet, reducing the effect of any anomalously low or high amplitudes at the resonant frequency.

7.2 Driving the Motion with a Sinusoidal Signal

In order to discover what effect these nearby frequencies had on the speed of the droplet, experiments were undertaken with the oscillation of the sample at a single frequency. While it was more difficult to ensure that the droplet was being oscillated at, or close to, its resonant frequency, the amplitude of the oscillation was much more controlled. All of the experiments presented here used a sinusoidal voltage signal to drive the speaker. This voltage signal had an amplitude of $1V$ and a frequency in the range of $0 - 300Hz$.

The position of the centre of the droplet within the image was measured as a function of time in the same way as for the white noise signal. An example of the plot this gave can be seen in Figure 7.6.

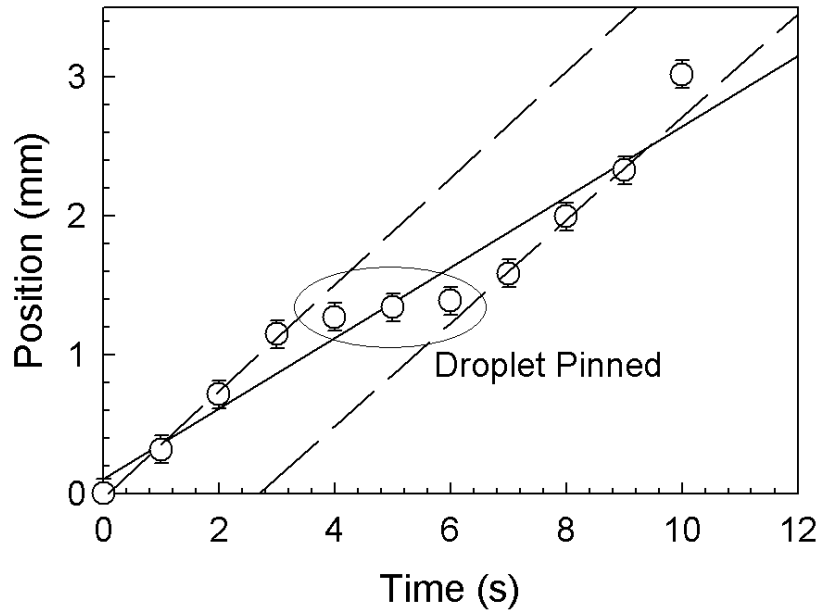


Figure 7.6: Position of the centre of an $8\mu\text{l}$ droplet of water as a function of time with a position of zero being the position before the vibration was turned on. Three distinct regions can be seen within this plot. The first and final region show the droplet moving at full speed while the central region (marked on the graph) shows the droplet has been pinned and slowed almost to a standstill. The average velocity over these three regions was found to be $255\mu\text{ms}^{-1}$ by using a linear fit over the full 10 seconds (solid line). The droplet speed in the other 2 regions was found to be $\approx 380\mu\text{ms}^{-1}$ by using a linear fit over just those regions of the data (dashed line). This sample was vibrated at 210Hz , the approximate resonant frequency of the droplet.

In Figure 7.6 there is a significant reduction in the speed of the droplet for approximately 3 seconds (this region is clearly marked). This is believed to be a pinning event, which reduces the overall speed of the droplet. Outside of this event, the speed of the droplet was estimated (through a linear fit to the graph) to be approximately $380\mu\text{ms}^{-1}$. A linear fit to the entire data set gives the mean velocity of the droplet to be approximately $255\mu\text{ms}^{-1}$. However this is only a brief snapshot of the velocity of the droplet, and as such the accuracy of a given measurement is unknown. At these speeds, the droplet moved too far off the edge of the image to accurately measure the location of the centre of the droplet after approximately 10 seconds. This means that it is difficult to get an accurate measure of the mean velocity on these gradient samples under these conditions as there is no information as to the frequency of the pinning events.

For this reason, both the mean speed and the maximum speed were measured for each droplet considered. In order to find the maximum speed that droplets would move upon these surfaces, a range of droplet sizes were considered. Figure 7.7 shows that the highest speed recorded was for a $8\mu\text{l}$ droplet. Above this volume, the droplets rested on more defects on the surface. This caused an increased resistance to movement and the droplets moved more slowly as a result. Below $8\mu\text{l}$ the droplets experienced a larger pinning effect at each of the cracks on the surface as a higher proportion of the droplet was pinned to a given crack than with larger droplets.

For these reasons, the remainder of the experiments were carried out with $8\mu\text{l}$ water droplets in order to find the highest possible movement speeds with these surfaces.

Following the decision to use $8\mu\text{l}$ droplets, the first experiment was to calculate an estimate of the mean velocity for an oscillation with a range of frequencies was calculated. This can be seen in Figure 7.8.

Figure 7.8 shows that, at frequencies of up to around 150Hz , no motion of

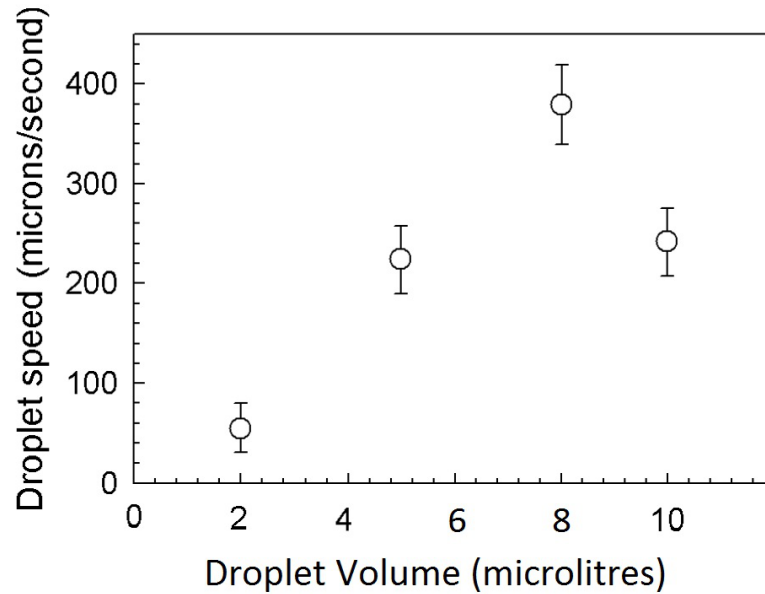


Figure 7.7: The maximum speed of a droplet vibrated close to its resonant frequency displayed as a function of droplet volume.

the droplet is observed. However as the frequency is increased, up to and beyond $210Hz$, a clear peak in the speed of the droplet becomes visible. This shows that the $8\mu l$ water droplet on this surface exhibits a resonance at $210 \pm 10Hz$. The speeds shown in Figure 7.8 represent the average speed of a water droplet travelling on these surfaces. However if a defect free gradient surface could be made of sufficient length, a much higher speed would be possible. Since small defect regions do exist upon these surfaces, the maximum speed of the droplet will give an approximation of the defect free speeds that would be achievable.

These maximum speeds are demonstrated in Figure 7.6 as dashed lines. In this example, the droplet is vibrated at its resonant frequency, $210Hz$, and the maximum speed is approximately $380\mu ms^{-1}$, almost 50% higher than the average speed of the droplet. A plot of the maximum speed as a function of frequency can be seen in the bottom frame of Figure 7.8.

This shows a similar profile to that seen in the top frame of Figure 7.8. They both show the same resonant frequency and display a similar resonance curve.

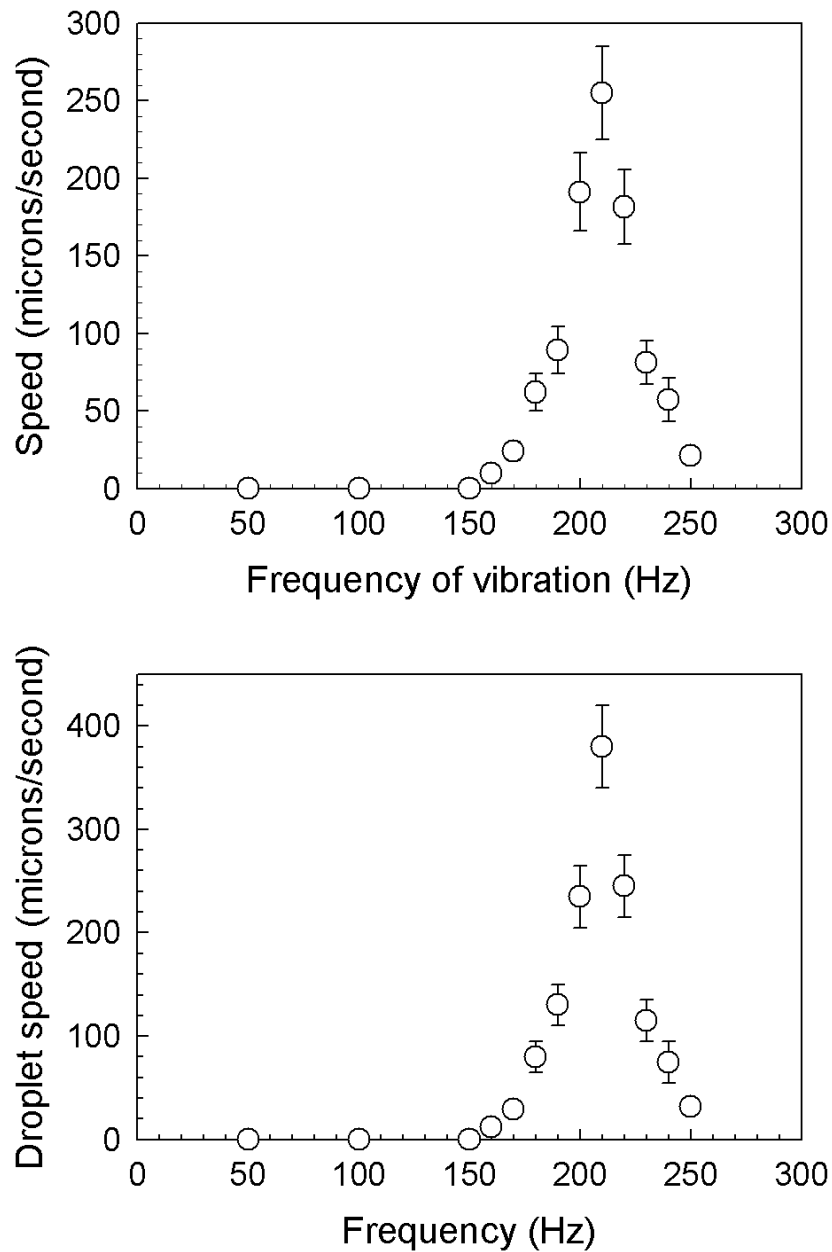


Figure 7.8: Graphs showing the speed at which the $8\mu\text{l}$ droplet moved when the bilayer was vibrated at a range of frequencies. The resonance of the droplet can be clearly seen at approximately 210Hz . No motion of the water droplet was observed for oscillation frequencies below 150Hz . *Top* Average speed of the droplet during the vibration. *Bottom* Maximum speed of the droplet during the vibration

When considering the maximum speed reached, the droplet can be seen to achieve speeds approximately 50% higher than the average speed.

In addition to these experiments, a similar test was run with a different gradient. The gradient chosen for this had pre-strains ranging from 10% to 30% over 16mm. This gradient was selected as there are very few cracks present at these pre-strains. Unfortunately no motion was seen on this gradient, regardless of whether or not an oscillation was applied to the sample. It is believed that the gradient was not large enough to cause motion with this level of oscillation.

Finally it was necessary to ensure that the resonance peak seen in the velocity profile of the droplet was due to the resonance of the water droplet and not due to the resonance of the speaker itself. In order to determine which resonance was being observed it was necessary to know the frequency response of the speakers amplitude for the frequencies used to move the droplet. This would give an indication of whether or not the resonance of the speaker was in the region that was being observed. In order to find the oscillation amplitude, the speaker was oscillated in an interferometry setup as described in section 3.6. The observed peak-peak amplitude that was seen using the interferometry is shown in Figure 7.9.

Figure 7.9 shows that although the amplitude was difficult to accurately measure with this technique, there was very little observable change in the peak-peak amplitude of the speakers oscillation throughout the frequency range considered for the droplet motion. This indicates that the resonance seen was the resonance of the water droplet, not the resonance of the speaker and was not an experimental anomaly resulting from the choice of speaker used to vibrate the droplet.

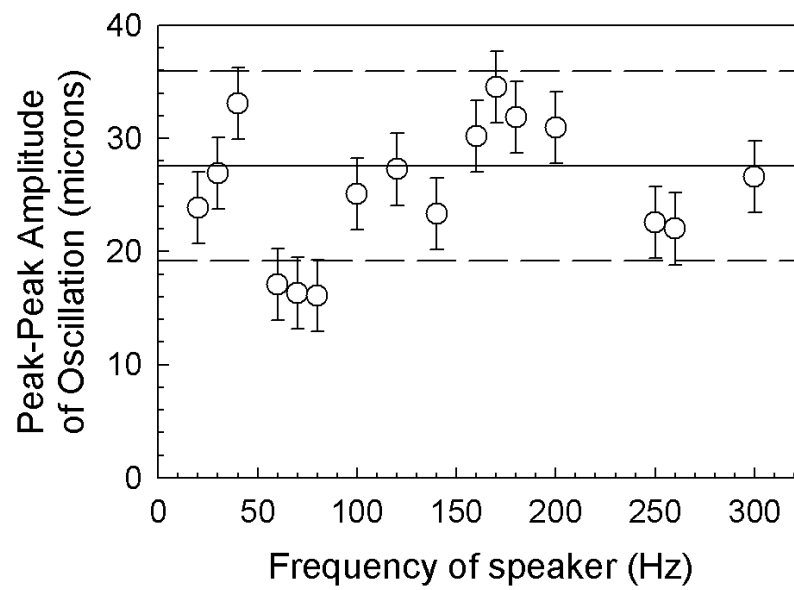


Figure 7.9: The calculated peak-peak amplitude of the speakers oscillation as a function of the frequency of oscillation for a sinusoidal input signal with an amplitude of $1V$. Also shown is the mean (solid line) and 95% confidence limits for the mean(dashed lines).

References

- [1] S. Daniel, S. Sircar, J. Gliem, and M. K. Chaudhury, “Ratcheting motion of liquid drops on gradient surfaces,” *Langmuir*, vol. 20, pp. 4085–4092, 2004.
- [2] S. Daniel, M. K. Chaudhury, and J. C. Chen, “Fast drop movements resulting from the phase change on a gradient surface,” *Science*, vol. 291, p. 633, 2001.
- [3] Y. Ito, M. Heydari, A. Hashimoto, T. Konno, A. Hirasawa, S. Hori, K. Kurita, and A. Nakajima, “The movement of a water droplet on a gradient surface prepared by photodegradation,” *Langmuir*, vol. 23, pp. 1845–1850, 2007.
- [4] L. Qiang, W. Hong, Z. Xun, and L. Mingwei, “Liquid droplet movement on horizontal surface with gradient surface energy,” *Science in China Series E: Technological Sciences*, vol. 49, pp. 733–741, 2006.

Conclusions

This thesis has discussed the production of highly ordered sinusoidal wrinkles with a precisely controlled wavelength and amplitude that are created by spontaneous pattern formation when thermally evaporated aluminium is deposited onto a pre-strained elastomeric substrate. These wrinkles have been shown to arise from the mismatch in the way in which the aluminium and the elastomer react to an external stimulus, in this case the release of pre-strain. Due to the difference in the Young's modulus of the elastomer and the aluminium, a stress is created at the interface between the two layers. It has been shown that the aluminium layer wrinkles in order to release this stress.

Two models were presented as possible candidates to explain this behaviour, the small deflection model [1], and the Song *et al.* model [2]. It was subsequently shown that the small deflection model could not accurately describe this system since the amplitude of the wrinkles that were produced were much larger than the thickness of the Al capping layer. Fortunately however, the Song *et al.* model [2] was found to be in excellent agreement with the wavelengths and amplitudes that were measured on these samples for all but the lowest pre-strain samples. A suggested reason for this discrepancy, was a change in the pre-strain during the deposition of the aluminium layer. The temperature of the elastomer was measured in situ throughout the aluminium evaporation and deposition, and was

found to rise by $\approx 30^\circ\text{C}$. This increase in temperature would change the apparent pre-strain on both the aluminium and the elastomer giving an additional source of pre-strain to consider.

The effect of this thermally induced strain was considered and shown to create a wrinkled surface prior to the release of the pre-strain. These wrinkles were shown to have wavelengths comparable in size to the low strain samples. It is therefore believed that this is the cause of the discrepancy between the Song *et al.* model [2] and the measured amplitudes at low strain values where the additional strain would play a large role, and that it is an insignificant effect at larger strain.

Following this, the viability of creating samples with a gradient in wetting properties was considered. The geometry of the samples was altered such that a gradient in the pre-strain was present prior to the deposition of the aluminium layer. This enabled a gradient to be created in the wavelength and amplitude of the wrinkles. Measurements of these were used to estimate the contact area of a droplet in different positions on the samples. This was shown to change with position on the sample making the gradient samples a viable candidate for the direction of droplet motion.

Following this, sessile water droplets were imaged upon the uniform pre-strain samples and the gradient pre-strain samples. On the uniform pre-strain samples, the observed contact angle was shown to change with the pre-strain for a selected thickness of the Al capping layer. Also, a gradient was discovered in the contact angle with respect to position with the gradient samples. This confirmed the presence of a gradient in wettability. Unfortunately no motion of the droplets was observed during time-scales shorter than that required for the droplet to completely evaporate. This is believed to be due to pinning effects that happen from the droplet finding a local energy minima on the wrinkles as well as pinning to defects within the wrinkled structure.

This pinning stopped the droplet from sampling any other nearby areas despite

the likelihood of a nearby location exhibiting a lower energy for the droplet than the current position. In order to allow the droplet to experience these nearby positions, the bi-layer sample was vibrated normal to the surface upon which the droplet was sat. This caused the contact area between the droplet and the surface of the bi-layer to expand and contract, thus allowing the droplet to sample nearby locations and move to those that were energetically favourable.

This vibration was initially applied in the form of a broadband or “white noise” signal. This caused the droplet to move, but the speed was rather low ($\approx 0.32\mu ms^{-1}$). Following this, a sinusoidal signal was used to drive the speaker, as this gave a higher degree of control over the frequency and amplitude of the oscillation. The speed of the droplet was shown to vary with the frequency of the applied oscillation, with the fastest motion evident at the droplets resonant frequency. This resulted in speeds in excess of $400\mu ms^{-1}$. These experiments were then repeated with a range of materials replacing the bilayer in order to ensure that the motion was a result of the structure on the surface of the sample, rather than due to a misalignment causing a slope in the sample or an oscillation that was not normal to the surface of the bilayer. No directed motion was seen on any flat materials or on the uniform pre-strain wrinkled samples. This led to the conclusion that the directed nature of the motion was a direct result of the gradient in surface texture.

This thesis has shown that the mechanical instability that arises from the mismatch in the mechanical properties of an elastomeric substrate and an aluminium capping layer can be used to create facile and inexpensive surfaces with a gradient in wettability. These surfaces could be used in applications where the presence of the speaker to apply vibrations to the sample is acceptable and can therefore replace existing, more expensive surfaces that are currently in use in these applications.

References

- [1] H. G. Allen, *Analysis and design of structural sandwich panels*. Oxford : Pergamon, 1969.

- [2] J. Song, H. Jiang, Z. J. Liu, D. Khang, Y. Huang, J. A. Rogers, C. Lu, and C. G. Koh, “Buckling of a stiff thin film on a compliant substrate in large deformation,” *International Journal of Solids and Structures*, vol. 45, pp. 3107–3121, 2008.

CHAPTER 9

Future Work

The main focus for further studies of these bilayer systems as a source of low cost rapidly manufactured surfaces for directed droplet motion would be working on improving the ease with which the droplet is moved. There are two main methods with which this could be achieved. Firstly the number of defects on the surface could be reduced, this would mean that there are fewer pinning events as discussed in section 7.2. With fewer pinning events the droplet would be able to move faster with the same vibration applied, and may be able to exhibit spontaneous droplet motion. In order to reduce the number of defects the cracking of the aluminium layer would need to be addressed. One possible method to reduce the cracking would be to replace the aluminium layer with a more pliable capping layer, for example polystyrene. Using a polymeric layer would hopefully mean that the capping layer would flow rather than yield when under a large strain. With this system it may even be possible to create smaller sized wrinkles that could push the water droplet from the Wenzel state (the water is completely wetting the substrate and filling the wrinkles) to the Cassie-Baxter state (the water droplet sits on top of the wrinkles and does not fill the wrinkles at all) further increasing the contact angle and getting closer to a superhydrophobic state such as those discussed by Fang *et al.* [1]. This will also allow the droplet to move around on the surface more freely as there will be much less contact between the droplet and

the wrinkled surface.

The second method would be to increase the amount of surface in contact with the droplet and consequently increase the reduction in energy that the droplet experiences during motion. This could be achieved by patterning the inside of a hollow tube of elastomer. When a droplet is placed within the tube, a much larger portion of the droplet will be in contact with the surface than when the droplet is on a flat bilayer. This would increase the force on the droplet and cause it to move more quickly as modelled by Fang *et al.* [1]. The complication with this technique comes in patterning the inside of a tube. Thermal evaporation could not be used as it would not cause a uniform layer of material to be deposited. For this reason, this technique would also require the capping layer to be replaced.

Both of these methods could be used in conjunction and have the potential to create cheap and easy transport methods for small water droplets.

References

- [1] G. Fang, W. Li, X. Wang, and G. Qiao, “Droplet motion on designed microtextured superhydrophobic surfaces with tunable wettability,” *Langmuir*, vol. 24, pp. 11651–11660, 2008.

List of Figures

1.1	Figure from Chung <i>et al.</i> [5] (a) Optical micrograph of a $\approx 2\mu\text{l}$ water droplet on a patterned surface, revealing an elongated, parallel-sided shape; (b) Dependence of the water contact angles in two directions (ϕ_{\perp} and ϕ_{\parallel}) on sinusoidally patterned surfaces as a function of degree of compression. The lines are meant to guide the eye and the error bars represent one standard deviation of the data, which is taken as the experimental uncertainty of the measurement.	2
2.1	Schematic of the wrinkled surface showing the 3 stresses that are considered. These are: 1. Compressive stress acting on the aluminium; 2. Stress from bending the aluminium layer; and, 3. Stress in the elastomer due to deformation.	16
2.2	Schematic of a bending Al capping layer along with the definitions of the terms from equation 2.3.3. Shown in light grey is the flat unstrained position of the Al capping layer (this is the case before the release of the pre-strain). In dark grey is the position of the Al capping layer once wrinkled (after the release of the pre-strain). . .	18
2.3	Interfacial energies acting on a droplet to determine the contact angle. The 3 interfacial energies are: γ_{12} , the liquid–solid interfacial energy, γ_{13} , the solid–air interfacial energy, and γ_{23} , the liquid–air interfacial energy (also known as the surface tension of the liquid). .	22

2.4	Diagrams of sessile water droplets on surfaces with different wavelengths. <i>Top Left</i> : an example of a droplet on a large wavelength sample - this droplet has a small contact angle and a small contact area. θ marks the macroscopic contact angle. <i>Top Right</i> : An example of a droplet on a small wavelength sample - this droplet has a large contact angle and a large contact area. θ marks the macroscopic contact angle. <i>Bottom</i> : An example of a droplet on a surface with a gradient in wavelength - the two visible contact angles are different and the contact area is now a function of the position.	24
3.1	a) A schematic of the PTFE mold used to make the elastomer substrates. b) The uncured elastomer was poured into the PTFE mold until it was full. This was left to cure for ≈ 15 hours before being removed. c) The cured disc of elastomer after removal from the mold. d) A strip was then cut from the elastomer disc to be attached to the stretching rig.	32
3.2	Schematic showing the production of wrinkled bilayer samples. A thick elastomer layer was stretched. A thin layer of Al was evaporated onto the strained elastomer layer. The pre-strain was released and the Al layer wrinkled.	32
3.3	<i>Left and middle</i> Schematic of the stretching rig used to create samples with a uniform pre-strain. <i>Left</i> unstrained sample. <i>Middle</i> strained sample. <i>Right</i> Photograph of the stretching rig	34

3.4 Schematic of two possible methods of applying a gradient in the pre-strain of the sample. In both cases the elastomer was of uniform thickness with the aluminium being evaporated onto the side shown. a) Applying a gradient in the cross-sectional area of the elastomer sample in the direction of applied pre-strain. b) applying a gradient in the initial length, L_0 , of the sample. In both images the direction of the force that was used to apply the pre-strain is shown. 35

3.5 Schematic showing how the shape of the sample gives a gradient in L_0 which, in turn leads to a strain gradient when the sample is stretched by a fixed amount, ΔL since $\varepsilon_{pre} = \frac{\Delta L}{L_0(x)}$ 36

3.6 a) An example image of a bilayer sample with a pre-strain of 1% and an Al capping layer of $196nm$ thickness, before the strain was released. The scale bar is $200\mu m$ long, also shown is the direction of the applied strain. b) An example image of a bilayer sample with a pre-strain of 1% and an Al capping layer of $196nm$ thickness, after the strain was released. The scale bar is $200\mu m$ long, also shown is the direction of the applied strain. 38

3.7 Diagram of the microscope used for these experiments. The Olympus BX51 was connected to a computer so that images taken by the digital camera could be saved for later analysis. 40

3.8 Ray diagram showing how 2 lenses can be used to make a simple microscope. The portion of the sample viewed can be seen to appear much larger in the image plane than its size at the sample. This is shown by the 2 arrows in these positions. 41

3.9 *Left* - Optical microscope images two different positions from opposite ends of a sample with a uniform pre-strain of 10% and an Al capping layer of thickness 73nm. *Right* - Optical microscope image of opposite ends of a gradient pre-strain sample with an Al capping layer of thickness 146nm, approximate pre-strain at image location is 30%. All scale bars are 200 μ m long 42

3.10 Schematic showing how the wavelength, λ , and amplitude, A , of the wrinkles are defined. 42

3.11 a) Optical microscope image of a sample with a uniform pre-strain of 10% and a Al capping layer of 219nm thickness with a 200 μ m scale bar. b) 2D fast Fourier transform of the microscope image, the peaks representing the wrinkled structure can be clearly seen. c) Radial average of the fast Fourier transform with the two important peaks labelled. 44

3.12 Schematic showing how the peaks or the troughs can be in focus.
a) The peaks of the wrinkled surface are in focus, the troughs are slightly out of focus. b) When the sample is raised slightly the peaks of the wrinkled surface go out of focus and the troughs come into focus. Beneath each frame is a schematic showing the region of the sample that is in focus. 46

- 3.13 Schematic of the stretching rig used to create samples with a gradient in pre-strain. *Top left* The unstrained elastomer is attached to the adjustable plates. The free region of the elastomer has an initial length dependent upon its position within the sample, $L_0(x)$ *Bottom left* The pre-strain is applied by separating the two halves of the stretching rig by an amount, ΔL . The pre-strain applied is dependent upon the position, $\varepsilon_{pre} = \frac{\Delta L}{L_0(x)}$, and the sample therefore has a pre-strain gradient *Right* A photograph of the stretching rig used, the micrometer that was used to measure the strain can be seen to the right of the shot. The amount the sample has been stretched, ΔL , is shown 47
- 3.14 Schematic of SFM in intermittent contact mode. 1) The cantilever is oscillating and the feedback loop in the SFM software moves the cantilever until the amplitude of oscillation matches a target value. 2) As the surface is scanned, the cantilever will be moved up or down in order to maintain a constant amplitude. 49
- 3.15 *Left* - Scanning force microscope scan of a portion of a wrinkled bilayer sample with a pre-strain of 10% and a 146nm Al capping layer. Shown on the image is the location of the line profile taken to determine the amplitude of the wrinkles. *Right* - Line profile taken from scanning force microscope image showing how the amplitude A is measured. 50

3.16 *Left* Schematic of the home built set-up used to capture images of sessile water droplets upon wrinkled surfaces. The white screen is illuminated with white light in order to create a disperse light source behind the droplet to aid with imaging the droplet. The sample upon which the droplet was placed was attached to a speaker cone such that a vibration could be applied at the droplets resonant frequency allowing it to fall into its relaxed state. The webcam was focused upon the droplet and was used to image the droplets profile. *Right* Photograph of the set-up used to take the images for the contact angle measurements 52

3.17 a) Example of a droplet upon a gradient surface. Image has been rotated to give a horizontal surface. b) Image has been binarised and the edges of the binary image have been highlighted. c) Lines fitted to contact points between droplet and surface. These are overlaid on the image along with the location of the surface. Also shown are the contact angles at each side of the droplet. 52

3.18 Images showing the movement of a $10\mu l$ sessile water droplet on a gradient surface where the droplet was vibrated close to a harmonic of its resonance frequency. In this case a vibration with a frequency of $210Hz$ was used. The images were taken in order from left to right with a $2s$ interval. The average speed of the droplet was over $200\mu ms^{-1}$. Scale bar $500\mu m$ 55

3.19 *Left* schematic of the interferometry used to measure the oscillation amplitude of the speaker. *Right* Photo of the same set-up. 56

3.20	<i>Left:</i> Power spectrum of the intensity of the light for the simulated oscillation with a peak-peak amplitude of $20\mu m$ and a range of frequencies from $50Hz$ to $200Hz$ <i>Right:</i> Power spectrum of the intensity of the light collected at the PMT for a sinusoidal signal with the same frequencies and an amplitude of $1V$	58
3.21	The calculated peak-peak amplitude of the speakers oscillation as a function of the frequency of oscillation for a sinusoidal input signal with an amplitude of $1V$. Also shown is the mean (solid line) and 95% confidence limits for the mean (dashed lines).	60
3.22	Schematic showing the set-up used for the axi-symmetric deformation test. The Lab jack is used to push the elastomer dome into the glass slide. Meanwhile the digital balance measures the force applied to the elastomer dome and the travelling microscope can be used to measure the diameter of the contact patch.	62
3.23	An example of data generated from the axi-symmetric deformation test used to determine the Young's modulus of the elastomer. A fit of these data to equation 3.7.1 gives $E = 2.11 \pm 0.08MPa$ and $G = 1.1 \pm 0.8Jm^{-2}$. The fit is shown on the graph as a solid line.	63
4.1	Schematic showing how the wavelength, λ , and amplitude, A , of the wrinkles are defined.	66
4.2	An example of the wrinkles that can be seen following removal of the bilayer sample from the thermal evaporation unit, but prior to release of the pre-strain. The scale bar is $200\mu m$ long. Also shown is the direction of the applied pre-strain.	67

4.3 The wavelength of thermally produced wrinkles as a function of Al capping layer thickness for three values of the pre-strain, 1%(\circ), 10%(\square) and 50%(\triangle). Also shown are the predictions for the wavelength using the Song *et al.* model [9] (solid line) and the small deflection model (dashed line). 69

4.4 Al capping layer thickness dependence of the wrinkle wavelength measured for pre-strains of 1%(\circ), 10%(\square), and 50%(\triangle) respectively. Also shown are the predictions of the Small deflection model for pre-strains of 1%(—), 10%(- -), and 50%(\cdots). 71

4.5 Al capping layer thickness dependence of the wrinkle amplitude, as measured using scanning force microscopy, for pre-strains of 1%(\circ), 10%(\square) and 50%(\triangle) respectively. 72

4.6 Al capping layer thickness dependence of the wrinkle wavelength (*Top*) and amplitude (*Bottom*) measured for pre-strains of 1%(\circ), 10%(\square) and 50%(\triangle) respectively. Also shown are the predictions of the Song *et al.* model [9] for the same pre-strains; 1%(—), 10%(- -), and 50%(\cdots). 73

4.7 A range of images showing how the cracks in the Al layer evolve with increasing pre-strain. All of these samples have had the pre-strain applied in the vertical direction with respect to these images and have had a 219nm Al layer evaporated onto them. A $200\mu m$ scale bar is present in all images. a)5% pre-strain, no cracks are observed at this pre-strain. b)10% pre-strain, some cracking is observed although the major contribution to surface patterning comes from the wrinkling of the bilayer structure. c)30% pre-strain, the density of cracking has increased, however the major contribution to surface texture still comes from the wrinkling. d)40% pre-strain, wrinkling is still observed however the major contribution to surface texture comes from cracking of the aluminium layer. 76

4.8 Plot showing how the density of the cracks varies with increasing pre-strain. The crack density is seen to increase linearly with increasing pre-strain. 77

4.9 Pre-strain dependence of the wavelengths (\circ) and amplitudes (\square) of wrinkles on elastomer samples that were capped with a 219nm thick layer of Al. Also shown are the predictions of the Song *et al.* model [9] for wavelength (solid line) and amplitude (dashed line). 78

5.1 Dimensions of the trapezoidal free region of the elastomeric substrate used to create the gradient samples. All positions, x , on the sample are measured from the 100% pre-strain position. The given pre-strain values assume $\Delta L = 2mm$ 81

5.2 Profile of predicted pre-strain for the chosen gradient sample. This assumes no effects due to the non-uniformity of the sample. $\varepsilon_{pre} = \frac{\Delta L}{L_0(x)}$ 82

5.3	A comparison of the radial average of the fast Fourier transform of uniform and gradient samples. <i>Top</i> - Sample with a uniform pre-strain of 50% with a 146nm thick Al capping layer. <i>Bottom</i> - Sample with a gradient in pre-strain and a 146nm thick Al capping layer, the location on the sample was chosen to have a pre-strain close to 50%. When the position was accurately measured, the local pre-strain was found to be $\approx 55\%$	84
5.4	Example images of a gradient sample taken from a range of positions. The scale bar on each image is 200 μm long. The diagram on the left shows the approximate location from which each image was taken. The wavelength of the wrinkles can clearly be seen to increase with decreasing pre-strain,	86
5.5	A plot showing the wavelength of the wrinkles as a function of the position on a sample with a gradient in pre-strain and a 146nm thick Al capping layer. Also shown as a solid line is the prediction from the model by Song <i>et al.</i> [4]. The pre-strain value for each position was taken from Figure 5.2 to calculate the the predicted wavelength.	87
5.6	A plot showing the amplitude of the wrinkles as a function of the position on a sample with a gradient in pre-strain and a 146nm thick Al capping layer. Also shown as a solid line is the prediction from the Song <i>et al.</i> model [4]. The pre-strain value for each position was taken from Figure 5.2 to calculate the the predicted wavelength.	89
5.7	Definition of the terms used in equation 5.3.1. $L_{surface}W$ is the surface area of the wrinkled surfaces. L_0W is the projected area of the surface. In both cases W is the width of the sample.	91

5.8	The area ratio, as calculated numerically using equation 5.3.2 along with the measured values for wavelength and amplitude as shown in Figures 5.5 and 5.6 respectively, as a function of the position on the sample. A gradient in the area ratio can be clearly seen across the sample.	92
6.1	The measured contact angle of sessile water droplets on wrinkled elastomer-Al bilayers with a range of pre-strains. <i>Top</i> The measurements were taken immediately after the water droplet had landed on the surface. <i>Bottom</i> These results followed a 1 second oscillation of the bilayer, at a harmonic of the resonant frequency of the sessile water droplet. The capping layer thickness used for these experiments was $146nm$	97
6.2	The estimated wetting profile of sessile water droplets on the gradient pre-strain samples. The contact angles are measured on uniform pre-strain samples with the same pre-strain as the equivalent position on the gradient sample.	99
6.3	Definition of the values P_{Image} and L_{Image} used to measure the position of the droplet on the surface. These are both measured in pixels, however the length of the bilayer is also separately measured in mm to provide an accurate measurement for the position of the droplet on the surface using equation 6.0.1.	100

6.4	An $8\mu\text{l}$ sessile water droplet on a gradient pre-strain sample with a 146nm capping layer with pre-strain going from 10% at the low strain end to 100% at the high strain end ($\approx 90\%$ pre-strain at the displayed position). Images from before (<i>left</i>) and after (<i>right</i>) the oscillation of the bilayer are shown. The contact angle on each side of the droplet is shown in both cases with an error of $\pm 1^\circ$. A change in contact angle can be seen in both cases, with a change of $\approx 3^\circ$ for the post vibration droplet.	101
6.5	Graph showing individual measurements of the contact angle seen as a function of the droplets position on the gradient sample. Both sides of the droplet were measured individually. The contact angle closest to the low pre-strain end of the sample (\circ) and the contact angle closest to the high pre-strain end of the sample (\square) are both shown. Although at large pre-strains (small position) the contact angle does not change much, a change in the contact angle can be clearly seen for low pre-strain.	102
7.1	Images of a sessile water droplet on a gradient pre-strain surface viewed from above. These images were part of an experiment to determine whether the evaporation time-scale was longer or shorter than the time-scale for measurable movement. These three images were taken at times of a) 0 minutes, b) 30 minutes, c) 60 minutes and d)75 minutes. The droplet can be seen to be shrinking due to evaporation and after 1 hour and 15 minutes the droplet has fully evaporated. However the droplet does not exhibit any detectable motion.	106

7.2	<i>Left</i> , example power spectrum from a single run of the experiment. There is clearly a large difference in amplitude between different frequencies. <i>Right</i> , average power spectrum from 100 experimental runs. This shows that on average each frequency will have the same amplitude over multiple runs.	109
7.3	Plot showing the measured position of a sessile water droplet during application of a vibration consisting of white noise. The distance that the centre of the droplet had moved since the vibration was turned on is plotted against the duration of the vibration. An initial fast movement is seen for approximately 30 seconds before a slower speed becomes evident for the rest of the droplets motion.	110
7.4	Images showing the motion of the droplet on the sample. The sample is mounted on the speaker with the high pre-strain end to the right of each image and the low pre-strain end to the left. The images are in order from left to right and were taken at intervals of 10 minutes. The droplet can be seen to move from the high pre-strain end of the sample towards the low pre-strain end.	111
7.5	Images showing the lack of motion seen when vibrating droplets on (<i>top</i>) flat elastomer samples, (<i>middle</i>) flat aluminium evaporated onto a silicon substrate and (<i>bottom</i>) uniform pre-strain samples. In all three cases the images were taken from left to right at times of 0 minutes, 5minutes and 10 minutes after the start of the vibration respectively.	112

- 7.6 Position of the centre of an $8\mu\text{l}$ droplet of water as a function of time with a position of zero being the position before the vibration was turned on. Three distinct regions can be seen within this plot. The first and final region show the droplet moving at full speed while the central region (marked on the graph) shows the droplet has been pinned and slowed almost to a standstill. The average velocity over these three regions was found to be $255\mu\text{ms}^{-1}$ by using a linear fit over the full 10 seconds (solid line). The droplet speed in the other 2 regions was found to be $\approx 380\mu\text{ms}^{-1}$ by using a linear fit over just those regions of the data (dashed line). This sample was vibrated at 210Hz , the approximate resonant frequency of the droplet. . . . 114
- 7.7 The maximum speed of a droplet vibrated close to it's resonant frequency displayed as a function of droplet volume. 116
- 7.8 Graphs showing the speed at which the $8\mu\text{l}$ droplet moved when the bilayer was vibrated at a range of frequencies. The resonance of the droplet can be clearly seen at approximately 210Hz . No motion of the water droplet was observed for oscillation frequencies below 150Hz . *Top* Average speed of the droplet during the vibration. *Bottom* Maximum speed of the droplet during the vibration 117
- 7.9 The calculated peak-peak amplitude of the speakers oscillation as a function of the frequency of oscillation for a sinusoidal input signal with an amplitude of 1V . Also shown is the mean (solid line) and 95% confidence limits for the mean(dashed lines). 119